Experimental and modelling studies of foam enhanced oil recovery

Boeije, Chris

Important note
To cite this publication, please use the final published version (if applicable).
Please check the document version above.

EXPERIMENTAL AND MODELLING STUDIES OF FOAM ENHANCED OIL RECOVERY

CHRISTIAN SIMON BOEIJE

EXPERIMENTAL AND MODELLING STUDIES OF FOAM ENHANCED OIL RECOVERY

PROEFSCHRIFT

ter verkrijging van de graad van doctor
aan de Technische Universiteit Delft,
op gezag van de Rector Magnificus prof. ir. K.C.A.M. Luyben,
voorzitter van het College voor Promoties,
in het openbaar te verdedigen op maandag 25 april 2016 om 15:00 uur

door

CHRISTIAN SIMON BOEIJE

Master of Science in Mechanical Engineering
Geboren te Zwolle, Nederland.

Dit proefschrift is goedgekeurd door de:

  promotor: Prof. dr. W. R. Rossen

Samenstelling promotiecommissie:

Rector Magnificus,	voorzitter
Prof. dr. W. R. Rossen,	Technische Universiteit Delft, promotor

Onafhankelijke leden:

Prof. dr. H. Bertin,	Université de Bordeaux
Dr. H. Hajibeygi,	Technische Universiteit Delft
Dr. S. Y. F. Vincent-Bonnieu,	Shell Nederland/Technische Universiteit Delft
Prof. dr. ir. R. A. W. M. Henkes	Technische Universiteit Delft
Prof. dr. P. L. J. Zitha	Technische Universiteit Delft
Dr. K. H. A. A. Wolf	Technische Universiteit Delft
Prof. ir. C. P. J. W. van Kruijsdijk	Shell Nederland/Technische Universiteit Delft, reservelid

CONTENTS

1

INTRODUCTION

1.1 THE USE OF FOAM IN ENHANCED OIL RECOVERY

With an ever-growing global population comes an increased demand for energy. Despite the current increased attention for renewables, oil remains one of the world's main energy sources (Key World Energy Statistics (2014), BP Statistical Review of World Energy June 2015). Especially the increase in energy consumption in emerging markets means the thirst for oil will likely increase in the years to come (Wolfram et al. (2012))

Discoveries of new oil fields has been in decline since the 1960s (Robelius (2007)). Therefore the current approach of increasing oil production is focused on producing more oil from fields that are already being operated. Conventional techniques employed in oil production from reservoirs cannot recover all of the oil from the subsurface. At present, the amount of oil that is recovered is generally between 20 and 40% of the oil that is initially in place in the reservoir (Muggeridge et al. (2013)). Recovering the remaining 60 to 80% requires Enhanced Oil Recovery (EOR) methods. One of the commonly applied EOR methods is gas injection. Gas (supercritical CO_2, hydrocarbon gases, N_2 or steam) is injected into the reservoir to displace the oil and to maintain pressure in the reservoir. Gas EOR processes are efficient at displacing oil where the gas sweeps (i.e. where the gas contacts the oil). However sweep efficiency is poor because of reservoir heterogeneity, viscous instability between injected the gas and the more-viscous fluids it displaces, and gravity override of gas.

All three causes of the poor sweep efficiency can be addressed by applying foam EOR. The use of foam as an enhanced oil recovery method was first proposed by Bond and Holbrook (1958). With foam, the gas is not a continuous phase, but is trapped in bubbles which are separated by thin liquid films called "lamellae". These lamellae are stabilized by adding surfactant (short for "surface active agent") which can adsorb onto the gas/liquid interface. The trapping of gas in separate bubbles impedes it from flowing freely within the reservoir thus reducing its mobility (Schramm (1994); Kovscek and Radke (1994); Rossen (1996)). The number of separate bubbles per unit volume is known as the foam

texture. Finely textured foams have very small bubbles which lead to a large reduction of the mobility, whereas coarser foams that contain fewer lamellae to restrict the flow do not influence the mobility quite as much. Therefore, finely textured foams are also often referred to as "strong" foams, and coarse foams tend to be called "weak" foam. Still, the gas bubbles in porous media tend to be larger than an individual pores. If multiple bubbles occupied a single pore, they would rapidly merge into bigger ones, because of gas diffusion (Rossen (1996)). Pore-scale schematics of a gas flood without foam compared to weak and strong foam floods are shown in **Figures 1.1a**, **b** and **c** respectively.

| (a) No foam | (b) Weak foam | (c) Strong foam |
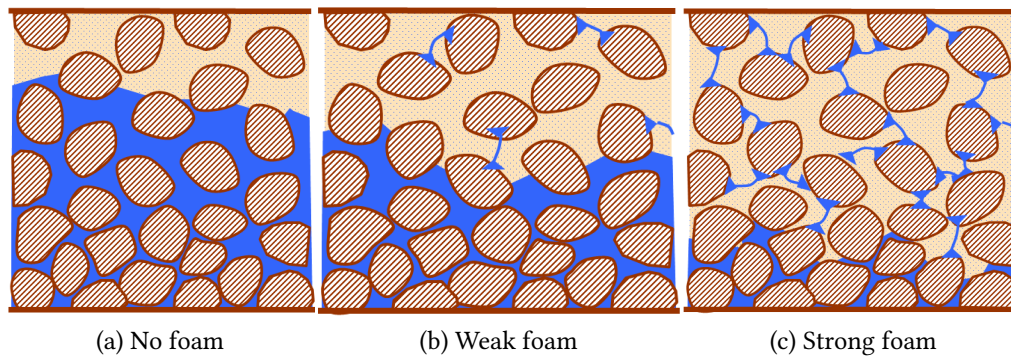
Figure 1.1: Schematic of foam in porous media (from Afsharpoor (2009)): (a) No lamellae are present, so gas is free to flow, (b) Some lamellae are present, somewhat reducing the gas mobility, (c) Large number of lamellae, severely restricting the gas's ability to flow.

It also reduces channeling of gas through high-permeability layers as foam generated in these layers tends to be stronger (i.e. mobility reduction is greater) (Moradi-Araghi et al. (1997)) than in low-permeability zones; thus gas is diverted to these lower-permeability zones. Also, the effect of viscous fingering and gravity override is lessened with foam, because the mobility of the displacing fluid is much reduced. **Figure 1.2** (from Farajzadeh et al. (2012)) shows a schematic of the effect of foam injection compared to a gas-injection process. Gas injection, shown on the left, results in channeling, viscous fingering and gravity override, whereas the foam produces a stable displacement front.

The effect of oil on the stability of the foam is also widely discussed in the literature. In most cases, oil is found to be detrimental to foam stability (e.g. Kristiansen and Holt (1992); Mannhardt et al. (1998)). An overview of recent studies on the effect of oil on foam is given in Farajzadeh et al. (2012). The focus of this project is the application of foam for mobility control, thereby enhancing oil recovery from carbonate formations. Several field trials using foam for EOR have already been performed, such as the project in the North Sea (Aarra et al. (2002); Blaker et al. (2002); Skauge et al. (2002)) which resulted
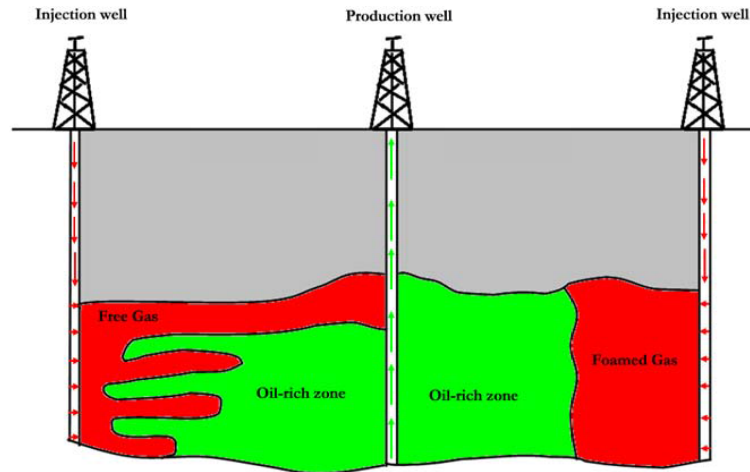
Figure 1.2: Schematic showing the influence of foam compared to a gas injection process (from Farajzadeh et al. (2012))

in additional oil recovery with a value of 25-40 million USD after an investment of 1 million USD. Results from other, smaller scale field trials are reviewed by Turta and Singhal (1998).

However, the use of foam in the petroleum industry is more widespread than this. Foam has already been used extensively as a drilling fluid in the field (e.g. Essary and Rogers (1976)) and also as a means of acid diversion (Rossen and Wang (1999)). The use of foam in porous media also extends beyond the petroleum industry. Several studies have been performed showing the potential of foam for aquifer remediation (e.g. Hirasaki et al. (1997a); Mamun et al. (2002)). Hirasaki et al. (1997b) then also used foam for aquifer remediation in the field and found that it can be successful at improving the sweep of remediation fluids that remove dense non-aqueous phase liquids (DNAPL) from aquifers.

1.1.1 *Foam Injection Methods*

There are four ways in which foam can be injected into the reservoir.

- With co-injection, where gas and aqueous surfactant solution are injected at the same time from the same injector. With this method, foam is already generated at the point where the fluids meet in the tubing, or at the moment both fluids enter the rock formation.

- Another method is to alternate between the injection of slugs of gas and surfactant solution. Hence, this is known as surfactant-alternating-gas or SAG injection. In this case, foam forms in the formation where gas

meets previously injected surfactant solution, or when surfactant solution meets previously injected gas. This is considered a preferred method over a co-injection process due to its increased injectivity (Shi and Rossen (1998); Rossen et al. (1999); Shan and Rossen (2004)).

- A novel approach is to dissolve surfactants directly into supercritical CO_2 (Le et al. (2008); Xing et al. (2012)). Naturally, this is not possible with all surfactants, but for some it is and in that case there is no need to inject an aqueous phase. The injected CO_2 with dissolved surfactant forms foam as it meets water in the formation.

- Another co-injection approach is to inject surfactant solution and gas simultaneously, but from different sections of a vertical well (Stone (2004); Rossen et al. (2010)). In this case the gas should be injected below the surfactant solution. Alternatively, the fluids can be injected using parallel horizontal wells, where gas should be injected from the lower well. Foam is generated where the fluids meet inside the reservoir.

1.2 FOAM RHEOLOGY IN POROUS MEDIA

As mentioned above, the degree to which a foam is able to reduce the mobility of gas depends on the bubble texture inside the porous medium. Khatib et al. (1988) found that for two-phase foam without oil, lamellae collapse at a fixed capillary pressure. Thus there is an abrupt transition between a state of strong foam and a state of nearly complete foam collapse at that capillary pressure. They referred to this as the "limiting capillary pressure" or P_c^*. Since capillary pressure is a function of the water saturation, there is also an accompanying limiting water saturation S_w^*.

Osterloh and Jante (1992) performed experiments in a sandpack using various gas fractional flows and total flow rates. They ran their experiments until the resulting pressure drop over the pack had attained a steady-state value and then they changed the flow conditions. They found that there are two foam flow regimes inside porous media: one where the resulting pressure drop is only a function of the gas superficial velocity and one where the pressure drop only depends on water superficial velocity. These regimes are commonly referred to as the low- and high-quality regimes, where quality means the gas fractional flow (f_g). Their results are summarized in **Figure 1.3**. This figure shows pressure-drop contours as a function of water and gas superficial velocity. The horizontal contours in the rightmost part of the figure comprise the low-quality regime and the near-vertical contours in the left part of the figure are in the high-quality regime. Foam rheology in the high-quality regime is con-

sidered mostly Newtonian although several studies (e.g. Alvarez et al. (2001)) report modest shear thinning or even shear thickening in this regime. In the case of Newtonian behaviour, the water saturation in the high-quality regime remains fixed at S_w^*. On the u_w-u_g plot of figure 1.3 the foam quality separating the high- and low-quality regimes is drawn as a straight line (in this case $f_g = 0.94$). Flow behaviour in the LQ regime can be strongly shear thinning as was found by Alvarez et al. (2001). This means that the transitional foam quality is not a constant, but varies for different total superficial velocities.
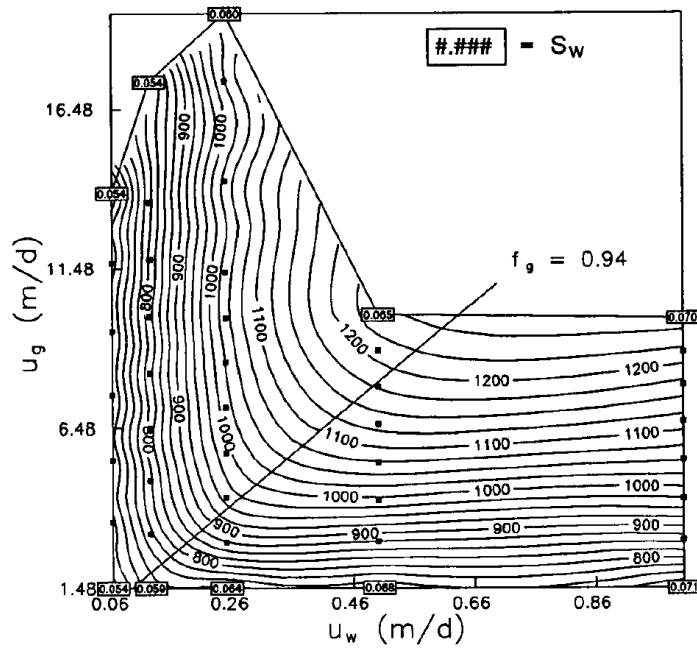
Figure 1.3: Pressure-drop contours [psi] as a function of superficial velocities of gas (u_g) and water (u_w) for a foam flood in a sandpack (from Osterloh and Jante (1992)). Each dot represents a steady-state pressure-drop measurement, and contours are plotted through these data. The "high-quality" regime is toward the upper left, and the "low-quality" regime to the lower right. There is a sharp transition between the two regimes (in this case at $f_g = 0.94$).

There are many studies that feature a more limited data set than that of Osterloh and Jante (1992). It is common to carry out experiments at one fixed superficial flow rate with varying foam quality rather than the full scatter of experiments performed by Osterloh et al. This would represent one diagonal line in the two-dimensional contour diagram as is shown in **Figure 1.4**. This figure shows data from Alvarez et al. (2001), who also performed the full scatter of experiments as did Osterloh et al. The dashed line represents experiments at one fixed superficial velocity (in this case 2.5 ft/day). Such a more limited set of experimental data is for instance found in Ma et al. (2013) and Chabert et al. (2012).
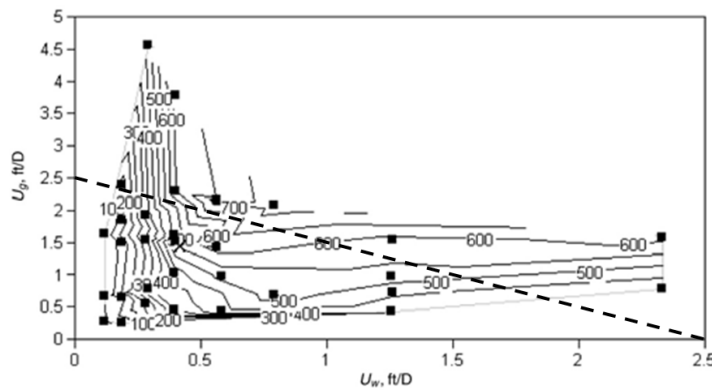
Figure 1.4: Pressure-gradient contours [psi/ft] as a function of superficial velocities of gas (u_g) and water (u_w) (from Alvarez et al. (2001)). Often datasets are limited to scans at a fixed total superficial velocity (but varying foam quality) which is indicated by the dashed line in the figure (superficial velocity of 2.5 ft/day).

There are also several petrophysical constraints that determine the maximum attainable mobility reduction factor with foam. First of all there is the issue of low-permeability rocks. As mentioned above, the foam's ability to reduce gas mobility is a function of permeability. Several studies find that the lower the permeability, the lower the mobility reduction factor (Bernard and Holm (1964); Moradi-Araghi et al. (1997)). Falls et al. (1988) showed that the mobility reduction factor (which they denote as apparent viscosity of the foam) is proportional to the third power of the capillary radius; thus larger pores mean more effective foam. Sanchez and Hazlett (1992) found that a wettability change towards more water-wet conditions was necessary for foam to form in their bead pack experiments. On the other hand, Suffridge et al. (1989) found that limited foaming was possible in their experiments in oil-wet porous media.

1.3 SURFACTANT SCREENING

For a foam EOR project to succeed, it is necessary that the surfactant can withstand the harsh operating conditions such as high-salinity brines, elevated temperatures and the presence of oil. In addition, the petrophysical parameters of the reservoir also play a role as mentioned in the previous section.

Various surfactant screening methods can be found in literature, ranging from bulk-foam stability tests (e.g. Lau and O'Brien (1988) and Vikingstad et al. (2005)) to measuring a surfactant's ability to alter parameters such as interfacial tension and rock wettability (Seethepalli et al. (2004); Kumar et al. (2008) and Chen and Mohanty (2014)) to measuring foaming performance in model porous

media that can be flushed and reused quickly (Duerksen (1986) and Kuehne et al. (1992)).

Foam-column apparatuses can be used to qualitatively assess other foaming performance parameters such as foam stability, by determining half-life of a generated foam column (see e.g. Andrianov et al. (2011) and Singh and Mohanty (2014)) or foam strength (or texture) through visual bubble-size analysis. Porous-media tests are commonly aimed at assessing the foam's ability to reduce total mobility. A surfactant's foaming performance in bulk does not necessarily correlate with its performance inside porous media. Conflicting results can be found in literature: for example Tsau and Grigg (1997) find a decent correlation between foaming in bulk and porous media, while Mannhardt et al. (1998) and Kam and Rossen (2003) did not find good agreement between the two types of tests.

Despite the variety of surfactant screening studies available in literature there are still various aspects which need to be addressed. These include the effect of wettability and the effect of oil on foam.

1.4 MODELING OF FOAM RHEOLOGY IN POROUS MEDIA

Two main types of foam simulation models can be distinguished that describe the behaviour of foam in porous media. Population-balance models (Falls et al. (1988); Friedmann et al. (1991); Kovscek and Radke (1994); Kam et al. (2007)) are aimed at completely capturing all of the physics that describe the foam rheology. These models represent the dynamics of bubble creation and destruction explicitly along with the effect of bubble size on gas mobility.

Rather than looking at the bubble size directly, the second group represents the effects of foam implicitly through a gas-mobility-reduction factor that is a function of water saturation, surfactant concentration, and other factors. A wide variety of models in the second group exist, with different levels of complexity (Law et al. (1989); Patzek and Myhill (1989); Kular et al. (1989); Fisher et al. (1990); Islam and Farouq-Ali (1990); Mohammadi and Coombe (1992); Cheng et al. (2000)). Models in the second group all implicitly assume local equilibrium (LE) between dynamic processes creating and destroying bubbles, which is why we refer to these as "LE" models here. In recent years, most of these allow for the abrupt collapse of foam at a limiting capillary pressure or limiting water saturation (Khatib et al. (1988)). Popular LE models found in commercial simulators such as CMG STARS, Schlumberger ECLIPSE and UTCHEM are all capable of accounting for a limiting water saturation and all simulators do this in a similar fashion.

Population-balance models are mathematically more complex to implement than LE foam models. These models face numerical challenges, because of their complexity and the differing time scales of bubble population dynamics and the overall displacement. LE foam models that account for an abrupt increase in gas mobility at a limiting capillary pressure or water saturation represent the two steady-state strong-foam regimes at high and low foam quality (flowing gas fraction) as well as do the population-balance models (Cheng et al. (2000); Ma et al. (2013)).

One of the issues arising in foam modeling is that with foam multiple steady states can exist (Gauglitz et al. (2002); Rossen and Bruining (2007)). Currently, only population-balance models can represent this phenomenon. Other physics that are exclusive to population-balance models include the dynamics of foam creation and propagation at a shock front, and the creation of foam at the entrance of the porous medium. If these phenomena are not the subject of study, current LE foam models are as capable of representing foam behavior as current population-balance models. This is why in this study we focus primarily on LE foam models.

1.5   THE SAG INJECTION PROCESS

As mentioned above, the surfactant-alternating-gas (SAG) injection process has distinct advantages over a co-injection process and is thus often the preferred injection method. With SAG, foam does not form directly in the well, and is quickly displaced from the vicinity of the well in the formation, which leads to increased injectivity compared to a co-injection process. This advantage is a result of the good injectivity of a gas slug during a SAG foam process, even though the foam that is formed further in the reservoir maintains mobility control with the fluids ahead of the foam bank. Several studies find that a SAG process, especially with large slugs of gas and liquid, has significant advantages in injectivity and overcoming gravity override (Shan and Rossen (2004); Kloet et al. (2009); Faisal et al. (2009); Leeftink et al. (2015)). Whatever the slug size, injectivity depends primarily on mobility very near the well, where even small slugs of surfactant and gas are large compared to the region of interest. Thus it is crucial to model the period of gas injection in SAG accurately.

In this study we focus our modeling efforts primarily on foam behaviour during a gas-injection cycle of a SAG process. Since the usage of large slugs of gas and liquid is the preferred method, it is likely that local equilibrium applies to most of the period of gas injection. Therefore our modeling approach is to fit an LE foam model to steady-state data rather than fit to results from dynamic

experiments. We also assume that LE applies in the field. This is an appropriate approach for a process with large slugs.

Laboratory coreflood experiments such as the one described above by Osterloh and Jante (1992) tend to be performed at a variety of different foam qualities. Fractional-flow theory and simulation show that most of the data gathered in such an experiment is irrelevant to the period of gas injection in a SAG process (Rossen et al. (1999)). Only the behaviour of foam at very high foam qualities determines whether mobility control can be maintained in the gas injection cycle of a SAG injection process. This is caused by the abrupt change between a state of strong foam and no foam which occurs at the limiting water saturation S_w^*. The resulting effect this has on the fractional-flow curve is shown in **Figure 1.5** (from Rossen et al. (1999)) which shows what the water fractional flow curve commonly looks like in the presence of foam, including the abrupt change at S_w^*. This means that for a gas-injection process ($f_w = 0$) there will be a shock from a very low water fractional flow back to the initial state. It is essential that one has an appropriate fit in this region to determine whether a SAG injection process will be successful or not.
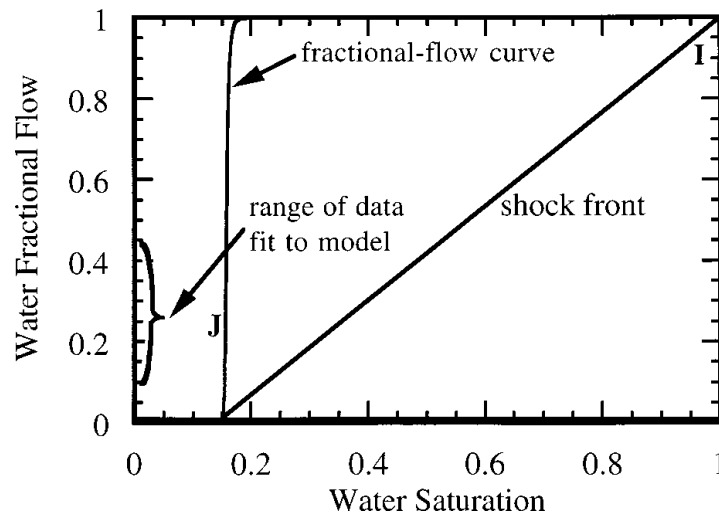
Figure 1.5: Fractional flow curve in the presence of foam (from Rossen et al. (1999)). There is an abrupt change between a state of strong foam and no foam at the limiting water saturation S_w^*. In this case the foam model was fit to data for f_w between 0.1 and 0.44, but the shock front jumps to a saturation with $f_w < 0.01$.

1.6 RESEARCH OBJECTIVES

This work is aimed at providing further insights into the following research topics:

- The first goal is to develop a surfactant screening methodology that is tailored to a specific application. Many screening studies are already available in literature, but those mostly provide a general method of performing a screening study and leave out certain aspects which can be essential for certain applications. One of these is the use of the surfactant in oil-wet porous media. Further knowledge is required as to what extent and why stable foams can be generated under oil-wet conditions. Here we target to develop such a screening methodology.

- The next step is to develop an easy-to-apply method of fitting foam-model parameters to experimental data sets. The method needs to be able to obtain parameter values based on a fairly limited data set. We describe different fitting approaches for co-injection and SAG injection processes.

- In addition we describe a simple analytical radial flow model based on fractional-flow theory to model foam flow in the gas-injection cycle of a SAG injection period. The aim for the model is to serve as a starting point to which numerical simulations can be compared.

- The final aim of this project is to check whether foam can be applied as a means of enhancing oil recovery from carbonate formations. Many of the aforementioned difficulties of generating stable foams in porous media (that is: salinity tolerance, adverse wettability, low permeability and heterogeneity) apply especially in carbonate formations. Here we aim to gather experimental data of foam in carbonate rocks and use that data to find a set of parameters for modeling the foam.

1.7 THESIS OUTLINE

This thesis contains work from several articles which are either already published or are currently in prepartion for publication in peer-reviewed journals. All of them focus on a different aspect of the subject: foam enhanced oil recovery. Each subject is described in a separate chapter. This introduction serves as **Chapter 1**.

- **Chapter 2** focuses on the screening of surfactants. A screening methodology is developed to find surfactants that are suitable for use in a given reservoir. Major constraints include the presence of high-salinity brines, crude oil and the wettability of the porous medium in which the surfactants are to be used.

- **Chapter 3** discusses the determination of accurate parameter values for use in foam-flood simulations. Parameter values for local-equilibrium models are chosen based on experimental data. We extend the method of Cheng et al. (2000) to work with more-limited data sets. In this chapter we show a simple method for fitting foam model parameters for a co-injection process.

- **Chapter 4** provides further insights into parameter-fitting methods for Surfactant-Alternating-Gas (SAG) applications. Different applications require different parameter-fitting approaches. We show how the parameter-fitting approach for SAG applications differs from the method described in the previous chapter.

- **Chapter 5** deals with the development of a simple radial flow model for the gas-injection cycle of a SAG process based on fractional-flow theory. We compare its results with 2D simulations of foam flooding in a quarter-five-spot pattern.

- **Chapter 6** shows results from foam-flooding experiments performed using consolidated, low-permeability carbonate cores. Two different sets of experiments were performed. Indiana limestone cores were used in a series of foam floods that examine the ability of foam to form in these rocks at our working conditions. We apply our parameter-fitting method to the experimental data we obtain here to see whether the generated foams are suitable for use in a SAG injection process. Another series of experiments uses heterogeneous Edwards White carbonates. CT visualization experiments are performed to determine the influence of the heterogeneities (which include vugs that are several mm in size) on the foaming performance.

- Finally, the main conclusions from this work are given in **Chapter 7** along with recommendations for future work.

2

A METHODOLOGY FOR SCREENING SURFACTANTS FOR FOAM ENHANCED OIL RECOVERY IN AN OIL-WET RESERVOIR

2.1 INTRODUCTION

Gas-injection projects aimed at enhancing oil recovery tend to suffer from poor volumetric sweep efficiency. Foam can be used to improve macroscopic sweep by reducing the mobility of the injection gas (see e.g. Schramm (1994) and Rossen (1996)) and divert gas flow to lower-permeability regions of the reservoir. This will for instance reduce the effect of channeling by generating stronger foam in high-permeability zones, thereby increasing flow resistance and diverting gas into zones with lower permeability, as foam is most stable in regions of higher permeability (Khatib et al. (1988)). Also, the effect of viscous fingering and gravity override is lessened with foam, as the mobility of the displacing fluid is much reduced.

A foam-injection project starts with the selection of a surfactant that is able to work in the operating conditions (e.g. high pressure and salinity, elevated temperatures and presence of oil). In addition, the petrophysical parameters of the reservoir, such as rock permeability and wettability, can have significant influence on the surfactants' foaming performance.

Various surfactant screening methods can be found in literature, ranging from bulk-foam stability tests (e.g. Lau and O'Brien (1988) and Vikingstad et al. (2005)) to measuring a surfactant's ability to alter parameters such as interfacial tension and rock wettability (Seethepalli et al. (2004), Kumar et al. (2008) and Chen and Mohanty (2014)), to measuring foaming performance in model porous media that can be flushed and reused quickly (Duerksen (1986) and Kuehne et al. (1992)). In this study we focus on two of these methods, namely simple bulk-foam stability tests and tests of foaming performance in porous media. Bulk-foam tests are used to determine a surfactant's ability to stabilize foam under operating conditions. These tests allow for quick screening of a large number of surfactants based on parameters such as salinity and oil-tolerance.

Foam-column apparatuses can be used to qualitatively assess other foaming performance parameters such as foam stability, by determining half-life of a generated foam column (see e.g. Andrianov et al. (2011) and Singh and Mohanty (2014)) or foam texture through visual bubble-size analysis. However, a surfactant's foaming performance in bulk is not necessarily representative of its performance inside porous media. Conflicting results can be found in the literature: for example Tsau and Grigg (1997) find a decent correlation between foaming in bulk and porous media, while Mannhardt et al. (1998) and Kam and Rossen (2003) did not find good agreement between the two types of tests.

Foaming strength in porous media is quantified by means of its ability to reduce total mobility. In the lab, the mobility reduction factor (MRF) can be determined by measuring the pressure drop during the flooding process over the porous medium with foam present and comparing it to the pressure drop of a single-phase waterflood. The ratio between the two is the factor by which the mobility is reduced.

One of the first studies comprising both bulk and porous-media foam-screening experiments was that by Duerksen (1986), who conducted tests on various surfactants, especially focusing on their thermal stability. In a recent study, Chabert et al. (2012) devised a method for fast measurement of interfacial tension and foam stability in bulk for a large number of surfactant mixtures. The best performing surfactant of their study was used in a subsequent set of coreflood experiments.

Despite the variety of surfactant screening studies available in the literature there are still various issues which need to be addressed. These include the effect of wettability and the effect of oil on foam. Several studies (e.g. Kristiansen and Holt (1992) and Mannhardt et al. (1998)) indicate that contact with oil has a detrimental effect on foam formation and stability. Farajzadeh et al. (2012) has reviewed the current state of research on oil-foam interactions and the challenges that need to be overcome to produce an oil-tolerant surfactant. Also, rock wettability can have a severe impact on the foam mobility measured in coreflood experiments. Kuehne et al. (1992) obtained very limited foaming performance of the surfactants from their study in oil-wet dolomite cores. Suffridge et al. (1989) found that foam can be generated in oil-wet porous media, but that the foam mobility reduction is significantly less than that in strongly water-wet cores. Sanchez and Hazlett (1992) found that foaming was possible in oil-wet media only after wettability was altered towards more mixed-wet/water-wet conditions as a result of surfactant adsorption. In their experiment, the presence of oil prevented the wettability change and foam did not form in the oil-wet medium. On the other hand, Lescure and Claridge (1986) concluded that oil recovery was enhanced more in an oil-wet medium as com-

pared to a water-wet one due to increased surfactant adsorption in the latter case which led to reduced foam stability. Several studies on wettability alteration through surfactant flooding (e.g. Gupta et al. (2009) and Wang and Mohanty (2013)) show an increase in oil recovery when oil-wet rocks are changed to more water-wet conditions.

In this study we provide an efficient methodology for screening surfactants for suitability for mobility reduction in porous media. To this end we conducted bulk-foam tests to quickly determine the surfactants' ability to foam under relevant operating conditions. We followed these up with a series of foam floods in beadpacks to determine which of the surfactants is able to form and produce the strongest foam. We performed the latter tests in both strongly water- and oil-wet bead packs to check the influence of the wettability on foaming performance. We also injected crude oil in both the bulk and the porous media experiments to check the surfactants' tolerance to presence of oil.

2.2 EXPERIMENTAL APPROACH

This study is aimed at designing and illustrating an efficient methodology for assessing a surfactant's potential for use in a foam field test. We specifically aim to devise a method for finding surfactants suitable for use in oil-wet porous media. To this end we perform both bulk-foam stability tests and high-pressure foam floods in model porous media. The bulk-foam screening experiments are performed to find surfactants that can produce a significant amount of stable foam (1) in the presence of high-salinity brine, (2) at elevated temperature (less than 100°C) and (3) in the presence of crude oil. Since these are only qualitative experiments, we do not aim to select a single surfactant based on the results of these tests, but rather allow us to narrow the number of candidate surfactants. The best-performing surfactants are used in a subsequent set of screening experiments (described further below) which are aimed at providing more quantitative data on the foaming performance of the surfactants inside artificial porous media. In total we perform tests with 31 surfactants from six different vendors.

Table 2.1 lists all of the surfactants that have been tested in this initial screening step. Each surfactant is given a number. In the remainder of this text, the numbers are used to refer to the surfactants. The table also shows the type of the surfactants.

Table 2.1: List of surfactants used in surfactant screening experiments

SURFACTANT NUMBER	SURFACTANT TYPE
1	Alcohol ethoxy sulphate
2	Alcohol ethoxy sulphate
3	Alkylaryl sulphonate
4	Alkylpolyglycoside
5	Alkylpolyglycoside
6	Alkylpolyglycoside
7	Alpha olefin sulphonate
8	Alpha olefin sulphonate
9	Alpha olefin sulphonate
10	Betaine
11	Ethoxylated alcohol
12	Ethoxylated alcohol
13	Ethoxylated alcohol
14	Ethoxylated alcohol
15	Ethoxylated alcohol
16	Ethoxylated alcohol
17	Ethoxylated alcohol
18	Ethoxylated alcohol
19	Ethoxylated alcohol
20	Ethoxylated alcohol
21	Ethoxylated alcohol
22	Ethoxylated alcohol
23	Internal olefin sulphonate
24	Mixture
25	Mixture
26	Mixture
27	Mixture
28	Mixture
29	Nonylphenol, ethoxylated
30	Nonylphenol, ethoxylated
31	Nonylphenol, ethoxylated

Table 2.2: Brine composition for 200,000 ppm brine. For lower salinity these amounts are scaled proportionately

ION	CONCENTRATION [PPM]
Cl^-	122,500
Na^+	55,900
Ca^{2+}	19,500
K^+	2,100

2.2.1 *Bulk-Foam Screening Experiments*

The following steps are carried out to assess the surfactants' foaming performance in bulk. Surfactant solution is mixed with brine inside a test tube. The surfactant concentration is kept constant at 0.5 wt.% (wt./wt.) throughout all of these tests. Surfactant stock solutions are prepared at a concentration of 2.5 wt.% active content initially. Then, 1 g of this solution is mixed with 4 g of brine inside a 10 ml test tube. Thus, in total, the test tubes contain 5 g of 0.5 wt.% surfactant solution. Afterwards, the test tubes are closed with screw caps to ensure that no gas could escape from the tubes. These screw caps are capable of withstanding an overpressure of 1 bar, according to the manufacturer, which is sufficient to withstand the pressure rise inside the tubes as a result of the elevated temperature (55°C) that is used in these experiments. Tests are performed using three different salinities: 70,000, 120,000 and 200,000 ppm. The brine composition for the 200,000 ppm case is given in **Table 2.2**. Brines of other salinities follow the same proportions of ions.

The first set of experiments is carried out with test tubes containing only brine and surfactant in solution. Separate experiments are performed with crude oil present. In these experiments, the brine and surfactant solution are prepared in the same way as the first set of tubes, with the addition of 1 ml of crude oil to the mixture.

The capped test tubes are placed inside a rack which is mounted inside a thermostat water bath. The water temperature is maintained at 55 °C. The tubes are left inside the water bath for two weeks. Subsequently, the surfactants' foaming potential is assessed by conducting the following steps:

1. One test tube at a time is taken from the 55 °C water bath

2. The tube is checked visually for precipitation of surfactant in the brine

3. The tube is shaken manually for 10 seconds

4. Foam height and foam texture are recorded. Foam texture is inferred *qualitatively* from the bubble size in the foam, as described below.

5. The tube is placed back in the water bath

6. After 10 minutes the tube is once again taken from the water bath

7. Foam height and assessed foam texture are recorded again

The initial foam height and foam texture provide an indication of the surfactant's ability to stabilize foam in high-salinity brine and at a given temperature. Checking again after 10 minutes provides an indication of foam stability. If the foam height and texture have decayed significantly, the stability of the foam is low. One of the parameters that constrains the initial foam height is the height of the test tube. The length of the test tubes used is approximately 10 cm. As a result, some of the generated foams, combined with the surfactant-brine mixture, filled the entire test tube.

2.2.2 *Surfactant Screening in Model Porous Media*

The initial bulk-foam screening tests provide a method of fast screening of a large number of surfactants. The surfactants' solubility in brine can be assessed and a qualitative indication of the bulk-foaming potential with and without oil present can be obtained. However, as mentioned in the introduction, several studies indicate that a surfactant's foaming potential in bulk does not necessarily correlate well with that in porous media under reservoir conditions (see e.g. Mannhardt et al. (1998) and Kam and Rossen (2003)). Therefore, additional screening tests are required. In this section we discuss these further tests which comprise a series of foam-flooding experiments in homogeneous model porous media. The effect of wettability on foam strength is assessed by tests in both strongly hydrophilic and hydrophobic porous media.

EXPERIMENTAL METHODS AND CONDITIONS   A setup was constructed capable of performing foam-flooding tests at high pressure (100 bar back pressure) and elevated temperature (55 °C). A schematic overview of the setup is shown in **Figure 2.1**. The setup consists of a model porous medium which is placed inside a stainless steel core holder. In order to determine the influence of wettability, porous media with two different wettabilities are used. Uniform hydrophillic glass beads of 100 μm diameter are used to obtain a strongly water-wet pack, whereas lipophilic polyproylene beads with a diameter of approximately 90 μm are used to make a strongly oil-wet pack. These bead diameters correspond to a permeability of roughly 10 D (see Bird et al. (2002)) . The core

holder is mounted vertically inside a Tamson TV7000 thermo bath (water bath) which is used to maintain a constant temperature (55 °C) within the sample. Gas, surfactant solution and oil can be injected simultaneously into the bead-pack. Methane (CH_4) is used as the gas in these experiments and is injected into the system using a Bronkhorst EL-FLOW F231M mass flow controller. A Quizix QX-6000 low-flow-rate pump is used to inject surfactant solution into the system. Metal frits are placed up- and downstream of the sample; these serve as size-exclusion filters in order to avoid any solid particles from entering the bead pack. These frits may also play a role as foam generators as they may facilitate the mixing of gas and surfactant solution, but we did not check this specifically. In separate tests, the effect of oil is investigated as well by co-injecting it along with the other fluids into the system. A Gilson 305 Piston Pump is used along with a transfer vessel to inject crude oil with 32°API gravity.

Gas-loaded back pressure regulators (Dresser Mity-Mite Model 91) allow the experiment to be carried out at the relevant operating pressure (100 bar). A differential-pressure transducer (Endress+Hauser Deltabar S PMD75) with a range of 0-3 bar is installed to monitor the pressure drop over a 9 cm segment inside the bead pack. In addition, various absolute pressure transmitters (GE PTX 611) are present to monitor pressures in the various segments of the setup. All of the pressure transducers are connected to a computer using a 16 bit A/D converter, so the pressure can be monitored in real time and pressure readings can be stored for analysis.

The experimental procedure used in these tests is as follows:

1. Initially the model core (bead pack) is vacuum-saturated with surfactant solution (0.5% wt./wt. with up to 200,000 ppm salinity).

2. The system is pressurized by applying a 100 bar back pressure. Several pore volumes of surfactant solution are injected to ensure that adsorption is satisfied.

3. The permeability of the sample to surfactant solution is measured by monitoring the pressure drop over a sample segment at various different flow rates

4. Gas and surfactant solution are co-injected into the system with a foam quality (i.e. gas fractional-flow at operating conditions) f_g of 0.95 at a total superficial velocity ut of 3.5 m/day. As the gas reaches the pack, foam generation begins, resulting in a reduced mobility and an increase in the pressure drop. Injection is continued until a steady state is reached (i.e. the pressure drop reaches a constant value).
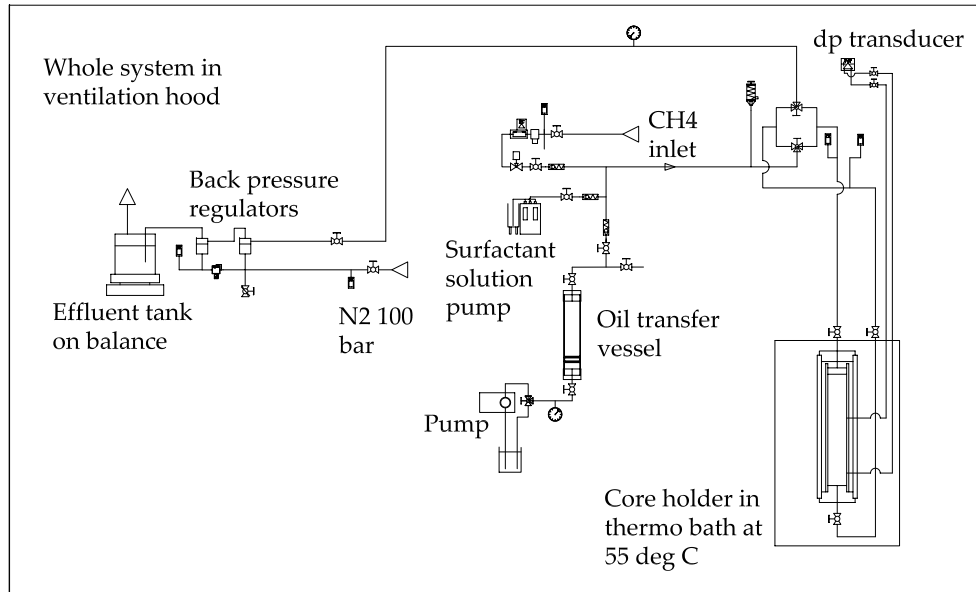
Figure 2.1: Schematic overview of the setup used in the high-pressure foam-flooding experiments. The apparatus can accommodate injection from the top or from the bottom of the pack. In our experiments we inject fluids from the bottom.

5. Initially tests are carried out in the hydrophilic bead pack without oil to quickly identify foaming performance for all surfactants.

6. The best-performing surfactants are assessed further on in a next set of experiments where crude oil is co-injected along with the other fluids at the same flow rate as the surfactant solution, to study its effect on the foam strength. Again the injection is continued until a steady state is reached.

7. Finally we repeat these tests using lipophilic bead packs which allow us to determine the influence on wettability on the surfactants' foaming performance.

This procedure is carried out for the surfactants selected based on results from the initial bulk-foam tests. Surfactants are tested at up to three different brine salinities. The bead pack is replaced after each experiment to ensure that each surfactant is tested under the same conditions and that no contamination (e.g. left-over oil or surfactant) is present in consecutive experiments. Also, surfactants may alter petrophysical properties of the beads such as wettability. Hence using a new bead pack in each experiment is desirable. The measured pressure drop inside the bead pack is used to calculate the mobility reduction factor *MRF* caused by the foam. The *MRF* is defined here as:

$$MRF \equiv \frac{\Delta p_f}{\Delta p_w} \tag{2.1}$$

where Δp_f is the measured pressure drop with foam and Δp_w is the pressure drop with a single-phase flow of surfactant solution at the same total superficial velocity with no gas present in the pack. This quantity is used to assess the obtained foam strength (i.e. larger MRF implies a stronger foam).

2.3 RESULTS AND DISCUSSION FOR BULK FOAM TESTS

The initial step to determine surfactant performance is checking for surfactant precipitation (e.g. caused by presence of divalent cations) and hence brine compatibility. Thereafter, shaking and observing the resulting foam can indicate (1) foam height, (2) stability and (3) texture. Initial foam height and foam height after 10 minutes (the stability indication) can be easily measured using a ruler. The foam's texture is a more qualitative assessment.

2.3.1 *Checking for Precipitations*

If the surfactant precipitates in the brine, it is not suitable for use in the foam flooding test, because the precipitated surfactant will aggregate inside the rock and there will therefore be a risk of pore-throat plugging and subsequent permeability reduction and injectivity loss.

Checking for precipitation is done by visual inspection. A flashlight is used to shine through the test tubes from the side in order to illuminate small precipitated particles that are difficult to see without the light. Four different kinds of precipitation could be distinguished. We refer to these types as: (a) *layer*, (b) *flakes*, (c) *slight* (which means a very limited amount of flakes was observed) and (d) *suspension*. These are illustrated and explained further in **Figures 2.2a** to **d**.

2.3.2 *Foam Texture*

The texture of the produced foam is assessed qualitatively based on bubble size. Finely textured foam has very small bubbles while coarse foam has much larger bubbles. Four levels of foam texture are distinguished ranging from very fine to fine, medium and coarse foam based on subjective judgement. Foam textures are denoted in the surfactant assessment figures and tables as VF, F, M and C respectively. Examples of each of these types are given in **Figures**
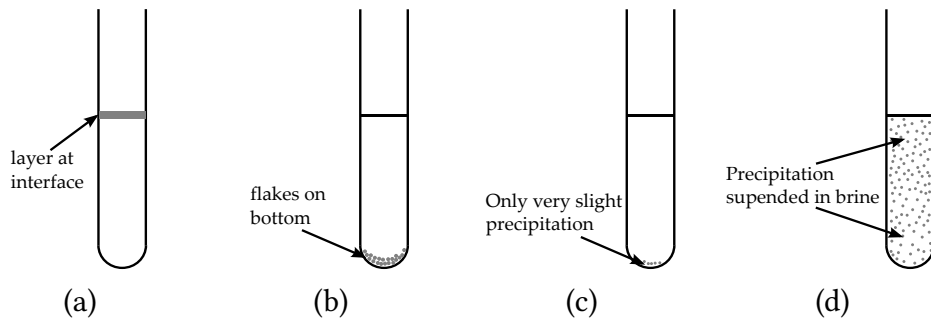
Figure 2.2: Schematic overviews of types of precipitation: (a) *layer*, a thin layer of surfactant aggregates at the water-air interface, (b) *flakes*, precipitated surfactant flakes can be observed on the bottom of the test tube, (c) *slight*, only very limited precipitation can be observed, mostly on the bottom of the test tube. This type is only visible when shining a flashlight through the tube, (d) *suspension*, large amounts of precipitation can be found throughout the solution

2.3a to **d**, which are photographs taken of test tubes. The width of the images corresponds to roughly 16 mm (i.e. the width of the tubes). The contrast of these images has been digitally enhanced to make the bubbles clearer to see. The categories are in part subjective and different observers might differ in the category they assign to a given test tube, but we believe the qualitative trends would be the same among observers. All judgements of foam texture given here were made by one observer.
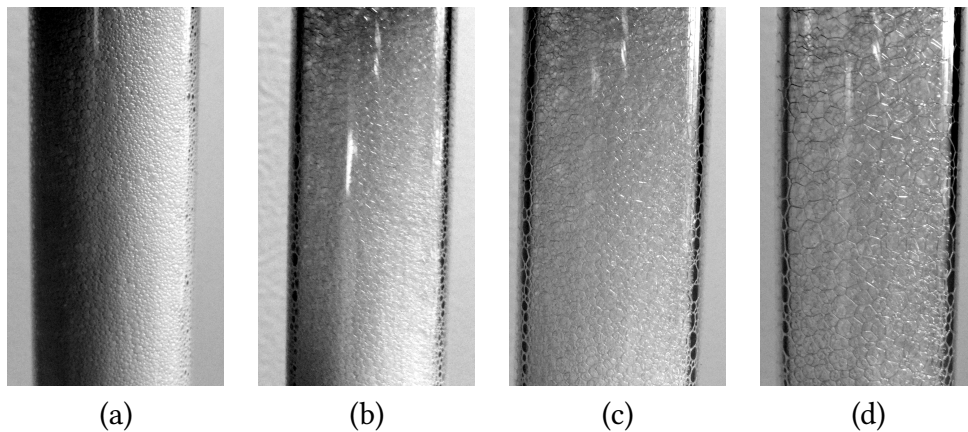
Figure 2.3: Classification of foam texture: (a) *very fine* (VF), finely textured foam with very small bubbles; (b) *fine* (F), bubbles are somewhat larger compared to the very fine type; (c) *medium* (M), even larger bubbles; (d) *coarse* (C), the largest observed bubbles. Image contrasts have been enhanced digitally. For comparison, the tube is 16 mm wide.

2.3.2.1   *Results for Experiments Without Oil*

The results for the experiments without oil present are shown in **Figures A.1, A.2** and **A.3** in **Appendix A** for salinities of 70,000, 120,000 and 200,000 ppm respectively. In these graphs two bars are shown for each surfactant. The left bar displays the initial foam height, whereas the right bar shows the foam height after 10 minutes. The surfactants are ordered by initial foam height. This means that surfactants with the largest initial foam height can be found towards the right end of the bar plots. Some of the surfactants with large initial foam height suffered from poor foam stability (i.e. the foam decayed fast). In addition, foam texture is shown in these graphs as well by means of the intensity of grey scale of the bars (darker bars indicate finer-textured foam). For completeness, all of the results are also tabulated in **Tables A.1, A.2** and **A.3** for each of the salinity values. These tables also include data on whether or not the surfactant precipitates in the brine.

These figures and tables show that salinity has a major influence on the performance of the surfactants. This is especially apparent when evaluating precipitation tendency. At the lowest tested salinity (70,000 ppm), the majority of the surfactants tested do not precipitate and instead form copious amounts of foam when mixed with gas. However, at higher salinity the number of surfactants that pass the precipitation test is reduced significantly. Only 5 out of 31 surfactants stay dissolved completely in 200,000 ppm salinity brine at the relevant surfactant concentration. We also find that the surfactants' performance relative to each other remains similar for each salinity; that is, the surfactants that perform well at low salinity also perform well at high salinity. Examples of surfactants that led to significant foam formation at all salinities are surfactants 2 and 6, which both led to a significant initial foam height and relatively stable foam.

2.3.2.2   *Results of Experiments With Oil Present*

The most promising surfactants from this initial test were used for coreflood experiments. Surfactants were selected based on their foaming ability and their salinity-tolerance. In these next experiments, crude oil was added to the test tubes to determine the foaming potential of the surfactants in the presence of oil. Results of these tests are shown in **Figures A.4, A.5** and **A.6** for salinities of 70,000, 120,000 and 200,000 ppm respectively. These figures show bar plots that are similar to the ones for the previous experiments. Once again, all of the results are also tabulated in **Tables A.4, A.5** and **A.6**.

The general trend that is found in these experiments is that oil has a detrimental effect on the stability of foam. Significant volumes of foam can still be generated for most surfactants, but the foam decays relatively fast. Especially

at high salinity, in most cases foam is not present in test tubes 10 minutes after shaking. Still, we found several surfactants that generated significant volumes of strong and fairly stable foam. These surfactants were selected for use in the next screening experiments (foaming performance in porous media). We also found that the majority of the surfactants that performed best in the previous tests without oil are also among the top performers in these tests. For example, surfactants 2 and 6 were among the best performers in both tests.

We also checked for precipitation of surfactant in the presence of oil in the same way as for the previous experiments. Most of the surfactants tested here passed the tests where no oil is present as performed earlier, so low or no precipitation was expected. However, some surfactants were used for these tests even though they did precipitate during the previous tests (especially at high salinity). As mentioned earlier, these surfactants were carried forward because they displayed high foaming potential. Most of the precipitation found in the previous experiment was of the 'layer' type, meaning that surfactant aggregates at the water-air interface. This type is difficult to observe in the presence of oil, because the surfactant is expected to form a layer in between the water and the oil. So even surfactants that failed the precipitation check in the no-oil tests passed here. This may be a result of our qualitative, "by eye", precipitation check and may not mean that no precipitation is present.

2.3.2.3 *Selecting Surfactants for Further Screening*

In the next experiments we test the foaming performance of the surfactants inside a porous medium. The surfactants we carry forward to these tests are mostly the ones that performed best in the bulk-foam experiments. We also add some surfactants that did not perform well, to test whether the bulk-foam tests can be used as a good predictor of foaming performance inside a porous medium. Some of the surfactants we selected precipitated at very high salinity. These are only tested at reduced salinity to avoid any precipitation inside the porous medium. In **Table 2.3** the surfactants used in the porous-medium experiments are listed. Surfactants are tested at the same salinities as in the bulk-foam experiments (70,000, 120,000 and 200,000 ppm). For each surfactant, the salinity at which they are tested is indicated. We selected a variety of surfactants (from alkylpolyglycosides to alpha olefin sulphonates and betaines). Also, the surfactants come from five different vendors.

These surfactants were selected for the following reasons:

- Surfactant 2 stays dissolved at high salinity. Furthermore it is among the best foamers we tested. Its foam is fairly stable in terms of retaining foam height, although the foam gets considerably coarser after ten minutes.

Table 2.3: Surfactants selected for the second batch of experiments, i.e. the assessment of foaming performance inside porous media

SURFACTANT NUMBER	SURFACTANT TYPE	SALINITY
2	Alcohol ethoxy sulphate	70, 120, 200
6	Alkylpolyglycoside	70, 120, 200
9	Alpha olefin sulphonate	70, 120
10	Betaine	70, 120, 200
12	Ethoxylated alcohol	70, 120, 200
19	Ethoxylated alcohol	70, 120, 200
26	Mixture	70
31	Nonylphenol, ethoxylated	70, 120

- Surfactant 6 was soluble at high salinity. In addition, it is one of the best performing foamers.

- Surfactant 9 is among the best foamers when oil is not present. However, it does precipitate at high salinity and its foaming potential is reduced in the presence of oil.

- Surfactant 10 does not precipitate even at high salinity. In test tubes, it produces moderate volumes of relatively stable foam.

- Surfactant 12 is chosen because it remained dissolved at the highest tested salinity. It is not a very good foaming agent under the tested operational conditions, so the main reason for selecting it is to check whether the foaming performance in these experiments gives any indication for the performance inside porous media.

- Surfactant 19 does not precipitate at high salinity. However, its foam completely collapses in the presence of oil. Therefore this will also be used to determine whether the foaming performance found here is similar to that in porous media.

- Surfactant 26 is a moderately performing foamer. Its foam retained most of its texture after 10 minutes. However, it can only be used at low salinity.

- Surfactant 31 is a moderately performing foamer. It can be used at low and medium salinity.

2.3.3 *Conclusions from Bulk Foam Tests*

The bulk-foam tests described here take little more time than the sort of solubility tests that must begin any study of surfactants for foam in with a given brine at a given temperature. As long as the temperature of interest is less than 100℃, the samples can be prepared and stored in racks of test tubes. Once stock solutions are prepared for the surfactants and brine(s), it is easy to create racks of test tubes containing every combination of surfactant formulation, brine, and presence or absence of oil. The foaming test here is qualitative, but it gives a rough indication of foaming and foam stability and eliminates obvious losers. Given the uncertain relation between any bulk-foam measurement and foaming in porous media, we believe this rapid approach offers advantages for screening large numbers of surfactants for a given field application.

We found that a large variety of surfactant chemical compositions (from alkylpolyglycosides to alpha olefin sulphonates and betaines) can all provide decent foaming results in bulk. Thus, we do not have to limit ourselves to a single surfactant type in the next batch of experiments.

2.4   RESULTS AND DISCUSSION FOR POROUS MEDIA TESTS

A typical example of a result obtained from the bead-pack floods is shown in **Figure 2.4**. At $t = 0$ co-injection of gas and surfactant solution is started upstream of the pack, with the upstream flow lines and the pack fully saturated with surfactant solution. Hence, the initial pressure drop is just the result of surfactant solution flowing through the sample. After some time gas reaches the bead pack (in this case at $t \approx 1700$ s) and foam starts to form inside the bead pack. This results in an increase in the measured pressure drop which continues to rise until gas breaks through at the end of the bead pack. After that, the pressure drop descreases somewhat and attains a steady-state value. In this case the pressure drop with foam is approximately 42 mbar compared to 2.1 mbar. Thus the mobility reduction factor using this particular surfactant is around 42/2.1 = 20. This indicates a comparatively weak foam. Other surfactants managed to attain mobility reduction factors of up to 2000, i.e. having pressure differences around 100 times greater than that shown in the figure. This is an example of an experiment without oil. For the experiments with oil, we start injecting oil after steady-state without oil is reached. It then takes a while for the oil to reach the bead pack and affect the foam, thereby altering the steady state.

Figure 2.5 shows the mobility reduction factor (*MRF*) for all of the investigated surfactant/salinity combinations without oil. Note that the *MRF* in the
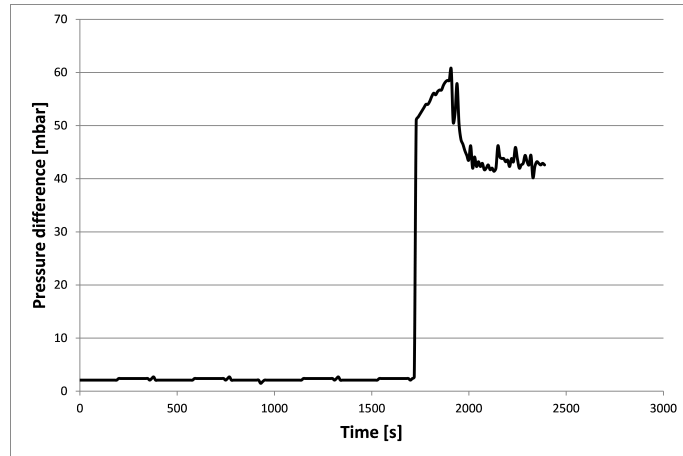
Figure 2.4: Example of experimentally obtained pressure difference over a 9 cm segment of the bead-pack. Pressure difference shows clear increase as gas reaches the bead pack

bar graph is shown on a logarithmic scale, because variation in foam strength can be several orders of magnitude when comparing different surfactants. The results shown in the figure indicate that foam strength with these surfactants tends to decrease with increasing salinity. However, as long as the surfactant is soluble in the brine, a foam can be generated; hence, even at the highest investigated salinity, strong foams could be observed for several surfactants. For completeness, **Table A.7** in Appendix A lists the *MRF* values.
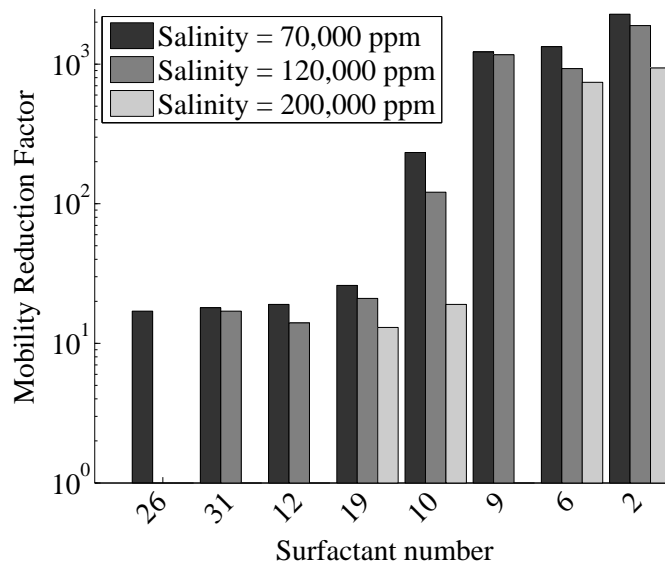
Figure 2.5: Measured mobility reduction factors shown here on logarithmic scale for all investigated surfactant/salinity mixtures without oil in the water-wet bead pack.

The best performing surfactants in this set of experiments are the same as those that did well in the bulk foam tests where foam texture was assessed. Thus we find a good correlation between bulk tests and porous media foam tests without oil. These results agree with Tsau and Grigg (1997), who also found decent agreement between foaming performance in bulk and porous media. However, they conflict with the results of Mannhardt et al. (1998) and Kam and Rossen (2003) whose results in bulk and porous media showed poor correlation.

The four best performing surfactants (surfactants 2, 6, 9 and 10) from these tests were carried forward for testing in the presence of crude oil. We narrowed the number of surfactants down to four, because these generated foams that are orders of magnitude stronger than the foams generated by the other surfactants. **Figure 6** shows a direct comparison of the measured *MRF* with and without oil present. Numerical values of the same experiments are listed in **Table A.7** in Appendix A.

Figure 2.6: Measured mobility reduction factors (*MRF*) in the water-wet bead pack without (white bars) and with oil (black bars). *MRF* values are shown here on a linear scale to emphasize the difference between measurements with and without oil. On the horizontal axis, the first label is the surfactant number and the second the brine salinity [x 1000 ppm].

For all of the experiments in the water-wet pack we find that foam strength is reduced as a result of the contact with the oil. However, for most experiments we still find a significant *MRF*, indicating that the foam does not collapse completely. This implies that these surfactants can be used effectively in a porous medium even when the foam would come into contact with oil.

Finally, we tested the same best-performing four surfactants in a strongly lipophilic bead pack. In separate tests, we also co-injected the same crude oil as in the hydrophilic packs. Foam quality and superficial velocity were the same as in the water-wet tests. *MRF* results from these experiments are given in **Figure 2.7** and tabulated in **Table A.9** in Appendix A. The absolute foam strength is roughly one order of magnitude smaller compared to the floods performed using the water-wet pack. Surfactant 10 gave hardly any reduction in mobility, indicating very poor performance. This result agrees with findings by Suffridge et al. (1989), who also observed reduced *MRF* in oil-wet media. Sanchez and Hazlett (1992) found that the presence of oil prevented the formation of foam in oil-wet beadpacks, because the oil prevented surfactant from reversing the pack's wettability. In our experiments oil was not introduced into the pack until foam was already established, so the case is not strictly analogous. The correlation with the bulk-foam tests is much less apparent for these tests than for the tests using the water-wet pack. In other words, the initial bulk-foam screening test was only predictive for the water-wet porous medium. First, the effect of oil is not nearly as pronounced in these tests; in several tests, mobility was reduced more when oil was added to the system. Yang and Reed (1989) report formation of emulsions of oil with surfactant solutions (in a study of supercritical CO_2 foam) that reduced mobility more than foam. Also, the effect of salinity appears to be more significant. Surfactant 2 produces only very weak foam at the highest salinity and surfactant 6 shows only moderate foam strength at the medium salinity. We repeated these experiments and found that the results are reproducible and not the result of experimental errors.

2.5 WETTABILITY ALTERATION IN OIL-WET POROUS MEDIA DUE TO SURFACTANT INTERACTION

Several studies report that a strong foam can either not be generated at all, or is very limited, inside an oil-wet porous medium (Kuehne et al. (1992); Sanchez and Hazlett (1992); Suffridge et al. (1989)). In this study we found that foaming in a homogeneous, unconsolidated porous medium is possible although the measured foam strength does tend to be lower than that in a fully water-wet medium. Still, a significant mobility reduction factor could be attained in the tests performed with the oil-wet medium (polypropylene beads), which leads to the question whether the wettability of the porous medium is changed as a result of interaction with the surfactant (Sanchez and Hazlett (1992)). To examine this, tests were carried out to determine the wettability of polypropylene, before, during and after interaction with surfactant.
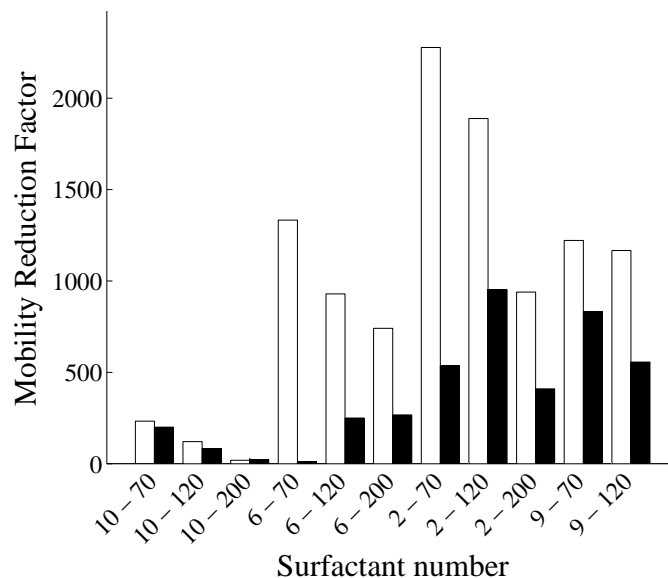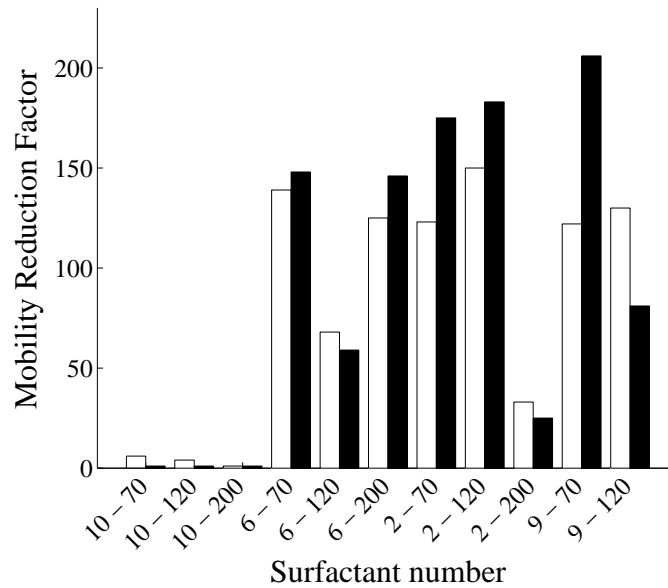
Figure 2.7: Measured mobility reduction factors (*MRF*) in the lipophillic bead pack without (white bars) and with oil (black bars). *MRF* values are shown here on a linear scale to emphasize the difference between measurements with and without oil. On the horizontal axis, the first label is the surfactant number and the second the brine salinity [x 1000 ppm].

2.5.1   *Experimental Methods and Materials*

Three different experiments were performed to determine if, and to what extent, the surfactants are able to alter the wettability of polypropylene. The first set of experiments is a qualitative method of wettability assessment of polypropylene. In these, test tubes are filled with polypropylene beads, surfactant solution and oil. We do not use the same beads that we used in the foam flooding tests: instead we use larger beads (≈3 mm in size) which allow for easier visual observation and recording of the results.

To determine the influence of the surfactants on the wettability of the beads we compare the behaviour of the original beads to that of beads that are exposed to the surfactants before being placed in the test tubes. To this end we soak beads in surfactant solution for 24 hours while placed in an oven that is maintained at 55°C. The initial assessment of the wettability takes place three hours after the test tubes are prepared. Afterwards all samples are left in the oven for 10 days to determine their long-term wettability behaviour.

We tested the three best-performing surfactants that were also used in the foam-flooding experiments in the polypropylene bead packs (surfactants 2, 6 and 9). Also, the same brine formulation was used in all wettability experiments as in the previous foam floods with salinities again up to 200,000 ppm.

The experiments are carried out at a temperature of 55°C using an oven to maintain consistency with the previous experiments that were carried out at the same temperature. The same crude oil (32°API) is used as the oleic phase as in the previous experiments. Additional repeat experiments are carried out using hexadecane for comparison with the crude oil tests. The hexadecane was dyed red in some tests using Oil-O Red ($C_{26}H_{24}N_4O$) in order to emphasize the location of the interface between the liquid phases.

Results from all experiments are analysed visually using a camera (Canon EOS 350D) paired with a macro lens (Canon MP-E 65mm f/2.8 1-5x Macro Photo). This combination allowed for detailed pictures of the relatively small setup without loss of quality. The camera was mounted on a tripod to maintain its position during long-exposure shots. The camera was kept in manual mode for all of the pictures. In general the aperture was kept relatively small (f/11) to maximise the depth of field in each image. ISO speed was kept at 100 and white balance on auto. In this way, the image exposure was the same for all images.

A second test involves contact-angle measurements. A polypropylene surface is placed in a beaker that is subsequently filled with hexadecane and maintained at 55°C. A drop of aqueous surfactant solution is then injected on top of the solid surface. The contact angle is measured through the aqueous phase. An angle larger than 90° indicates oil-wet nature of the PP surface whereas angles below 90° mean more water-wet conditions. As in the test tube test, we investigate the influence of the surfactant on the wettability by comparing the original PP to PP that has been soaked in the surfactant solution for 24 hours at 55°C. We cannot use crude oil in this experiment, because we would not be able to see the surfactant droplet through the crude oil. We determine the contact angle by drawing tangent lines at the interface between the phases and measure the angle between those lines using a digital goniometer. This causes a certain error as drawing the tangent lines is done "by eye". For our application this approximate method is sufficient. For more precise contact-angle measurement, a method such as that outline by Shojai Kaveh et al. (2011), with detailed image analysis methods, is more suitable.

Finally we performed a test to determine to which extent the surfactant is able to prevent crude oil from wetting the PP beads' surface. In this experiment, beads soaked in surfactant solutions for 24 hours were subsequently soaked in crude oil for 24 hours. Afterwards the beads were removed from the oil and placed back in surfactant solution maintained at 55°C to observe whether the oil coated the beads. The extent to which the oil coats the beads is measured here through the intensity of the images. Dark images mean more oil coats the beads.

WETTABILITY ASSESSMENT CRITERIA   In the test-tube experiments, the wettability is assessed by determining which liquid phase coats the beads. We distinguish four different levels of wettability ranging from strongly oil-wet to strongly water-wet. Representative results, with the four levels of water-wetness are shown in **Figures 2.8a** to **d**. When beads are not soaked in the surfactant solution before placing them in the tubes they are in the oleic phase. Interaction with the surfactant can change this preference and render them more water-wet.

(a)

(b)

(c)

(d)
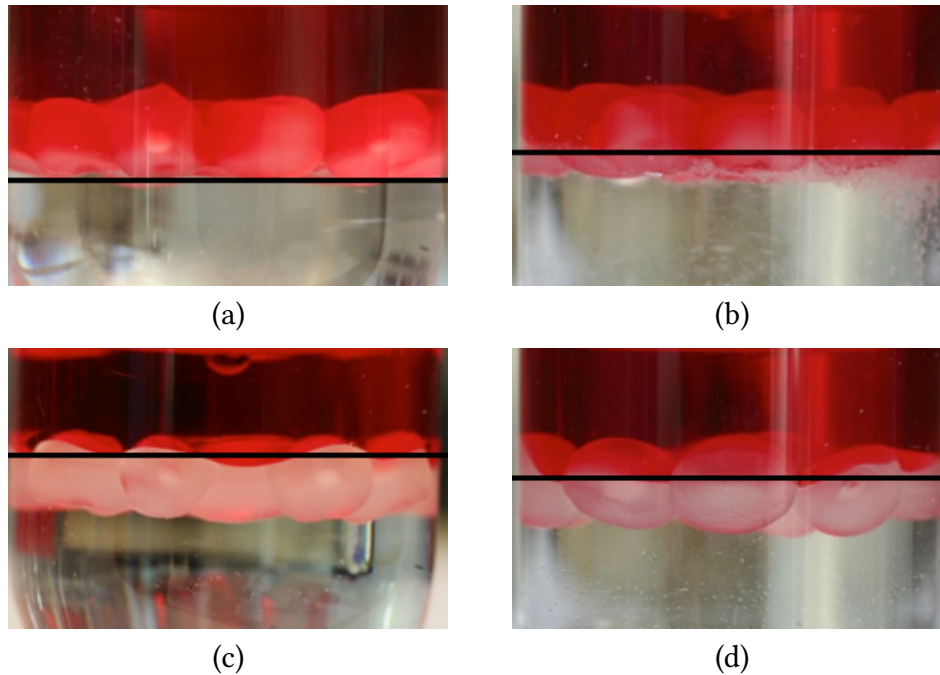
Figure 2.8: Polypropylene beads in test tubes with surfactant solution and hexadecane (dyed red). Four levels of wettability are distinguished depending on which liquid phase coats the beads' surface: (a) *strongly oil-wet*, (b) *moderately oil-wet*, (c) *moderately water-wet* and (d) *strongly water-wet*

Figures 2.9a to **c** shows some representative results from the contact-angle tests. These figures show drops of surfactant solution on a polypropylene surface surrounded by hexadecane. Figure 2.9a shows the clearly oil-wetting behaviour of the polypropylene surface before being exposed to surfactant. This results in a contact angle larger than 90° (in this case 145°). The polypropylene surface in Figure 2.9b has been allowed to soak in surfactant solution and as a result is clearly more water-wet with a contact angle of 60°. Some surfactants alter the wettability of the surface to such an extent that the surfactant does not bead on the surface, but rather spreads on it completely as in Figure 2.9c. The corresponding contact angle is close to 0° in this case.

(a)

(b)

(c)
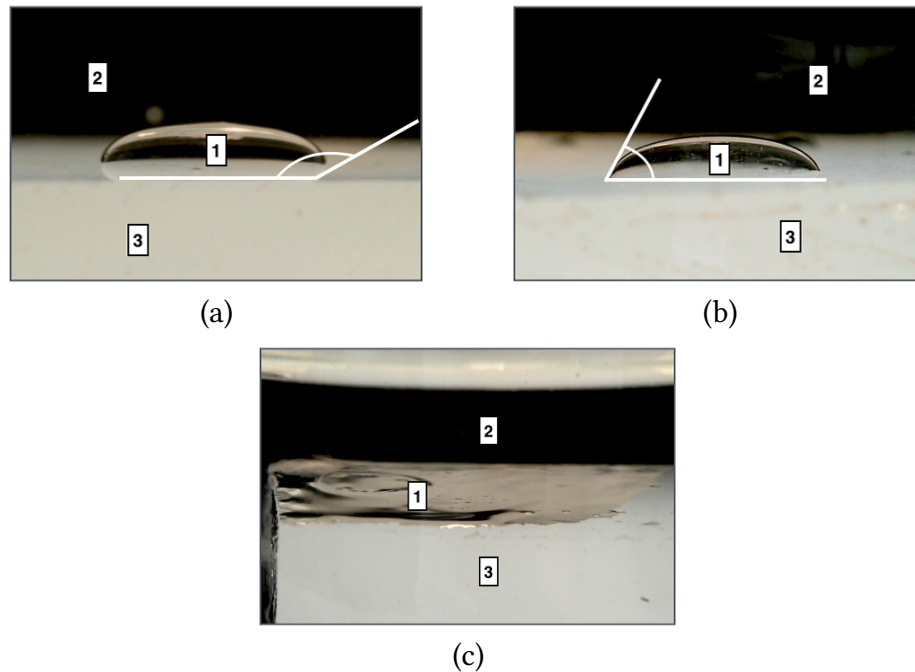
Figure 2.9: Several contact angles observed in the experiment indicating different wettabilities; numbers indicate various phases: 1. surfactant solution, 2. hexadecane, 3. polypropylene surface. (a) oil-wet nature before soaking (contact-angle: $\approx$145°), (b) water-wet nature after soaking (contact-angle: $\approx$60°), (c) surfactant solution spreading over surface, indicating fully water-wet nature (contact-angle near zero)

In our final experiment we analyse the intensity of images of beads to determine to which extent the oil is sticking to the beads. This is outlined in **Figure 2.10**. This is the result for beads that are not exposed to surfactant solution. Figure 2.10a is the original image taken with the camera and Figure 2.10b shows the cropped, grayscale image where only the beads were selected, removing the background of the image, which is not taken into account in the analysis. Figure 2.10c shows the intensity profile of the cropped image. In this case we see a clear intensity peak towards the left of the intensity spectrum indicating many dark pixels, which means a thick layer of oil coating the beads' surface. A measure of the amount of oil coating the beads is the ratio of dark to light pixels. Since we use 8-bit grayscale image in our analysis, the intensity can range from 0 (black) to 255 (white). We use a value of 75 as the cut-off intensity. The ratio we present is the number of pixels with intensity below 75 divided by the number of pixels with intensity above 75. **Figure 2.11** is an example of an image with a higher intensity, and therefore less oil is coating the beads. "By eye" comparisons between Figure 2.10a and 2.11a also show the differences of oil coating the beads. Analysing the histogram is a method of quantifying

this difference. Compared to the histogram shown in Figure 2.10c, the change in wettability is apparent from the shift of the histogram to the right for the histogram of Figure 2.11b. For reference: the ratio of the unsoaked beads is 4.45. We recognize the limitations of this method of analysis and only use it to distinguish between starkly different cases.

(a)

(b)

(c)
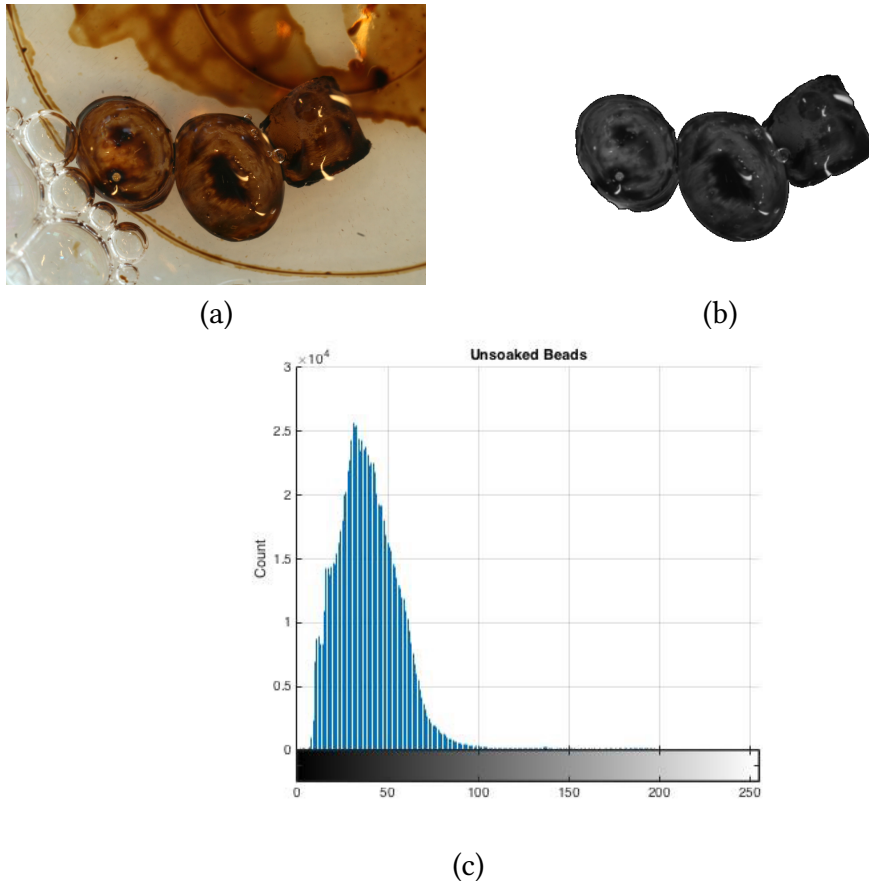
Figure 2.10: Image of beads coated with oil (a) before and (b) after cropping the beads and converting the image to grayscale. (c) Corresponding image histogram with 0 intensity representing black and 255 being white.

2.5.2   Results and Discussion

Tables 2.4 and 2.5 show all of the results for the experiments using crude oil and hexadecane respectively. Note that the test-tube experiments were carried out using both oils so these results appear in both tables. The crude-oil table further contains results from the image-intensity experiments and the hexadecane table contains contact-angle results.

(a)   (b)
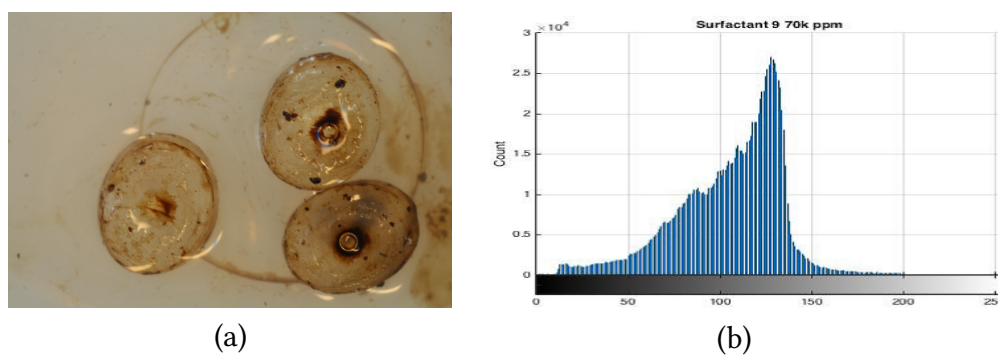
Figure 2.11: Bead image and corresponding histogram for beads soaked in surfactant 9. Intensity peak shifts right compared to that in the histogram for the unsoaked beads

Table 2.4: Results from crude- oil experiments: nomenclature for abbreviations used in the table - SWW: strongly water-wet, MWW: moderately water-wet, MOW: moderately oil-wet, SOW: strongly oil-wet. A higher ratio of dark to light pixels implies more oil is left coating the beads.

SURFACTANT NUMBER	SALINITY [×1000 PPM]	WETTING AFTER SOAKING	WETTING AFTER 10 DAYS	RATIO DARK TO LIGHT PIXELS
2	70	SOW	SOW	1.22
	200	SOW	SOW	1.34
6	70	*	SOW	0.40
	200	SOW	SOW	1.77
9	70	SWW	SWW	0.21

*Results from this test were inconclusive, but appeared to be intermediate-wet

Table 2.5: Results from hexadecane experiments: nomenclature for abbreviations used in the table - SWW: strongly water-wet, MWW: moderately water-wet, MOW: moderately oil-wet, SOW: strongly oil-wet.

SURFACTANT NUMBER	SALINITY [×1000 PPM]	WETTING AFTER SOAKING	WETTING AFTER SOAKING	CONTACT ANGLE BEFORE SOAKING [°]	CONTACT ANGLE AFTER SOAKING [°]
2	70	SWW	SOW	130	100
	200	SWW	SOW	145	60
6	70	SWW	SWW	140	0*
	200	MWW	SOW	140	50
9	70	SWW	SWW	140	0*

*The liquid spread on the surface so the contact angle is shown as 0°.

Results from the test-tube tests show a more pronounced effect for the experiments carried out using hexadecane than those using crude oil. This is may reflect the smaller density contrast between the crude oil and the PP beads. A larger density difference would tend to push the beads into the oleic phase whatever their wettability. The hexadecane tests may be a more valid comparison in this case, because the density of the polypropylene beads (0.9 g/cm^3) is right in between that of hexadecane (0.77 g/cm^3) and the surfactant solution (1.13 g/cm^3 for the solution using the 200,000 ppm brine). So the buoyancy force plays a smaller role compared to the tests with the crude oil which has a density of 0.87 g/cm^3 which is very close to that of the PP beads. **Figure 2.12a** shows a representative result for the crude oil test with the beads clearly remaining in the oil phase. The one test that did show complete alteration of wettability even when using crude oil is the test using surfactant 9. This result is shown in **Figure 2.12b**.

(a)   (b)
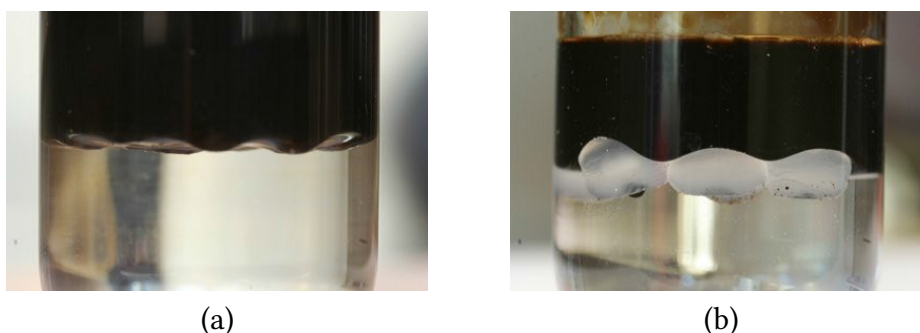
Figure 2.12: Results from test tube tests using crude oil: (a) representative result for most surfactants with beads clearly remaining in the oil-phase, (b) test using surfactant 9 shows complete wettability reversal with beads in the water-phase.

For the hexadecane tests, application of all surfactants resulted in drastic changes in wettability to more water-wet conditions. However, for most surfactants this is only a temporary change. After staying in the tubes for 10 days, most of the polypropylene beads reverted back to their original oil-wet state. This was not the case for the beads exposed to surfactant 9, which remained fully water-wet even after the 10-day period.

The image-intensity tests show that all surfactants cause the beads to turn more water-wet, allowing less oil to stick to the bead surface. All ratios observed here are considerably less than the 4.45 ratio found in the experiment with unsoaked beads. Surfactant 6 was very salinity-dependent, with the ratio changing from 0.40 to 1.77 from the low- to the high-salinity experiment. This was not the case for surfactant 2, which recorded similar ratios at both salini-

ties. Surfactant 9 performed best of all, with a ratio of 0.21, but this surfactant can only be used at the lower salinity, as it precipitates otherwise.

All contact-angle experiments (with hexadecane) indicated that the surfactants created more water-wet conditions. Very significant contact-angle reductions were found for all surfactants. Some even managed to alter the wettability to such an extent that the aqueous phase completely spreads on the PP surface.

2.5.3 *Conclusions from Wettability-Alteration Experiments*

The experiments show that an initially oil-wet polypropylene surface can be changed to more water-wet conditions after exposure to foaming surfactants. For the qualitative tests using crude oil, not all of the surfactants demonstrated the ability to change the wettability to a large extent. The comparison between the two oils is complicated by the different density contrasts between the oils and the beads. The density contrast is smaller for the crude oil which would tend to cause the beads to remain in the oil-phase. However, the experiments using hexadecane, with the beads show that wettability can be changed quite dramatically. In our tests we observed the wettability change from fully oil-wet to fully water-wet for several of the studied surfactants. Contact-angle tests confirmed these findings. For some surfactants the aqueous phase completely spread on the PP surface, indicating fully water-wet conditions. The image-analysis tests of the oil-coated beads revealed that the oil does not adhere to the polypropylene surface nearly as much when the surface is first exposed to surfactant solution, indicating a change in the wettability and thus an effective surfactant.

In general, the tests show that the surfactants do indeed change the wettability of the polypropylene surface, thereby resulting in more favourable conditions for foam generation and stability. Comparing with our bead-pack experiments using PP beads, we find a partial correlation. At low salinity, the best-performing surfactant in those tests was surfactant 9, which also performs best in the wettability alteration tests both in the crude-oil and the hexadecane experiments. The other two surfactants (2 and 6) performed similarly in the bead-pack tests at low salinity. However, at high salinity, surfactant 2 performed noticeably worse in the bead-pack experiments while the performance of surfactant 6 did not suffer the same impact on foaming performance. However, in our final wettability-alteration test, where we look at the amount of oil coating the beads, we observed the opposite. Surfactant 2 performed similarly at both tested salinities while surfactant 6's performance dropped significantly. Overall, surfactants 2 and 6 performed similarly in the crude-oil tests. In the hexadecane tests, surfactant 6 was a better performer which was especially ap-

parent from the contact-angle tests where it was considerably more effective than surfactant 6. These tests cannot be compared directly with the bead-pack experiments though, as crude oil was used in those experiments.

We should note that the bead-pack experiments took place in several hours so the packs were only exposed to oil for a limited period of time. In these wettability tests we also analysed the behaviour after 10 days. Because of the different time scale, these results may not correlate with our results from the bead-pack tests. But in a reservoir, rock is exposed to oil for prolonged periods of time so the tests with long exposure to oil may give a better indication of what happens in the field.

2.6   CONCLUSIONS AND RECOMMENDATIONS

1. We introduce a screening methodology for foaming surfactants that can be used both to quickly screen large numbers of surfactants through bulk-foam tests and also provide quantitative foaming performance data through foam flooding tests. The methodology takes into account the effect of oil, salinity and wettability of the porous medium.

2. Salinity is a major concern when evaluating surfactants. In this study, 26 of 31 surfactants analysed precipitated at the highest salinity levels tested (200,000 ppm).

3. As expected, presence of crude oil was detrimental to foaming performance in bulk for most surfactants. In water-wet porous media, the mobility reduction factor also decreased significantly with oil injected. However, some surfactants still produced fairly strong foams with oil present. For the oil-wet medium we did not find a general trend of reduced foam strength in the presence of crude oil. In fact, in some experiments foam strength increased when oil was injected along with the other fluids.

4. Foaming performance in water-wet porous media correlated well with bulk-foam testing: we found that surfactants that showed decent foaming potential in bulk also led to significant mobility reduction factors in the water-wet bead pack. This correlation is not as strong for the oil-wet pack.

5. Wettability (or hydrophilicity of the bead surface) plays a major role in foaming performance. In general, foam strength tends to be significantly lower in oil-wet porous media compared to water-wet packs. Also, surfactant performance in oil-wet porous media does not correlate with that in water-wet media. The best performing surfactant in the water-wet

pack was not the same as the best performer in the oil-wet pack. This can also explain the discrepancy in results found in literature, about correlating bulk-foaming performance with that in porous media, where porous media tests were carried out using oil-wet media. The influence of crude oil is much more limited for the oil-wet pack compared to the water-wet one (that is, *MRF* is not reduced as drastically by the presence of oil in the oil-wet pack as in the water-wet pack).

6. Overall, surfactants 2 and 6 proved to be the best-performing surfactants from these tests with high salinity tolerance and good foam strength in water-wet and oil-wet porous media. Therefore these surfactants were recommended for use in further testing in consolidated cores.

FITTING FOAM SIMULATION MODEL PARAMETERS TO DATA I: CO-INJECTION OF GAS AND LIQUID

3.1 INTRODUCTION

Gas-injection enhanced-oil-recovery (EOR) processes are efficient at displacing oil where the gas sweeps. However sweep efficiency is poor because of reservoir heterogeneity, viscous instability between injected gas and displaced oil and water, and gravity override of gas. Foam can address all three causes of poor sweep efficiency (Schramm (1994); Kovscek and Radke (1994); Rossen (1996)). Foam is injected in one of four ways: co-injection of gas and surfactant solution, injection of alternating slugs of gas and surfactant solution (SAG), injection of gas alone with surfactant dissolved in the gas, or injecting gas and surfactant solution simultaneously, but from different sections of a vertical well or parallel horizontal wells.

Design of effective foam projects requires accurate simulation of foam behavior in the formation. Cheng et al. (2000) show how the parameters for the STARS and UTCHEM foam simulators describing foam behavior without oil can be fitted to laboratory coreflood data, specifically a plot of pressure gradient as a function of superficial velocities of gas and water on which contours of pressure gradient are plotted. An example is **Figure 3.1**. In such a plot, the "high-quality" foam regime is that at relatively large superficial velocity of gas and small superficial velocity of water, in which the ∇p contours are nearly vertical. (Foam quality means gas fractional flow.) The low-quality regime is that at lower superficial velocity of gas and larger velocity of water, in which ∇p contours are nearly horizontal. Behavior in the high-quality regime can be modestly shear-thinning or shear-thickening, but in the low-quality regime it is markedly shear-thinning, reflecting the reduction in gas trapping with in-

---

The content described in this chapter is also published in: Boeije, C. S. and Rossen, W. R. Fitting Foam-Simulation-Model Parameters to Data: I. Coinjection of Gas and Liquid. *SPE Reservoir Evaluation & Engineering*, Vol. 18 (02) pp. 264 - 272, SPE 174544, May 2015.

creasing ∇p (Rossen and Wang (1999)) as well as the shear-thinning rheology of trains of bubbles (Hirasaki and Lawson (1985); Xu and Rossen (2003)). The transition between the high-quality and low-quality regimes occurs at a gas fractional flow or foam quality f_g^*; if the transition is abrupt, ∇p is a maximum at f_g^*. Because the low-quality regime is non-Newtonian, the transition foam quality f_g^* is not a constant, however, but varies with total superficial velocity.

Cheng et al. suggest that one pick one representative ∇p contour, draw the best horizontal line through the low-quality-regime data and best vertical line through the high-quality-regime data for the same value of ∇p, and fit the foam parameters to the intersection point of these lines. One can then use several horizontal contours in the low-quality regime to fit the shear-thinning behavior in that regime. The fit of Cheng et al. to the data in Figure 3.1 is shown in **Figure 3.2**. This approach assumes that the transition between regimes is abrupt; Cheng et al. argue that the nearly vertical slope seen in data in the high-quality regime suggest an abrupt transition. However, even if the transition is abrupt, in current models the ∇p contours are only approximately horizontal in the low-quality regime. To make them horizontal one would need to de-couple gas relative permeability and water saturation (Rossen and Wang (1999)).
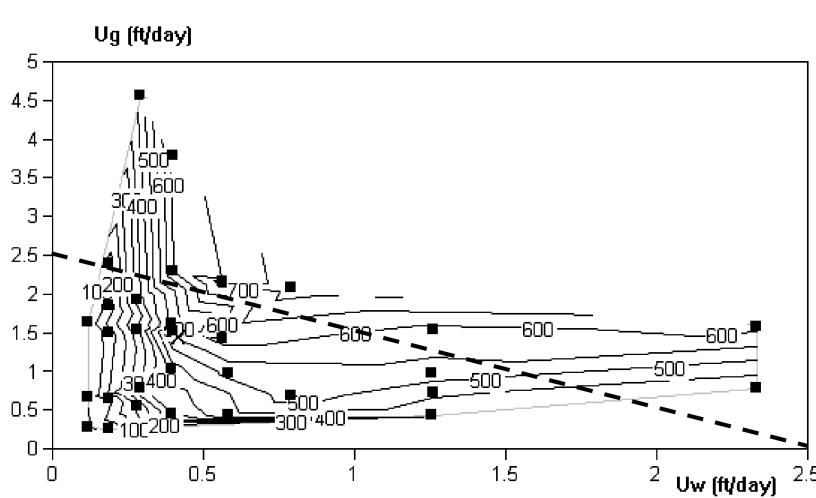
Figure 3.1: Pressure gradient (psi/ft) as a function of superficial velocities of gas (Ug) and water (Uw) for one foam formulation in a Berea sandstone core, from Alvarez et al. (2001). Each dot represents a steady-state measurement of pressure gradient, and contours are plotted through these data. The "high-quality" regime is toward the upper left, and the "low-quality" regime to the lower right. The dotted line represents a scan of foam quality at fixed total superficial velocity (in this case, 2.5 ft/day).
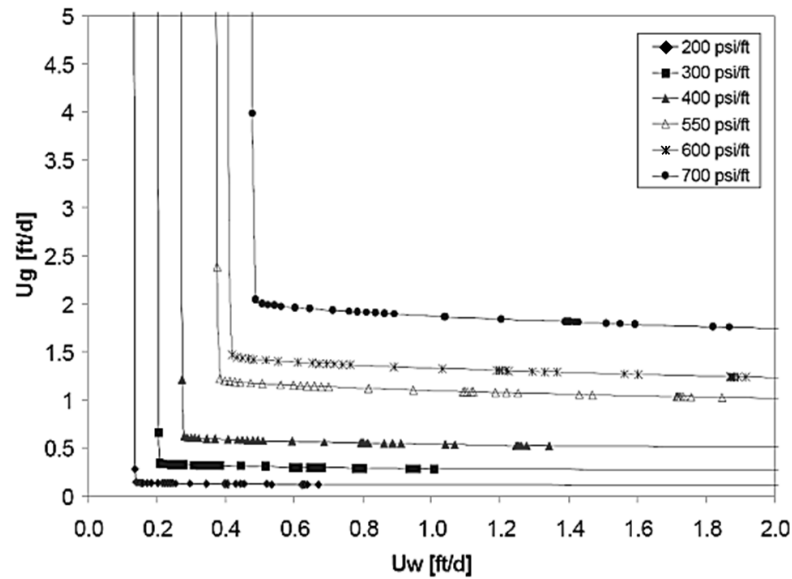
Figure 3.2: Fit of Cheng et al. (2000) to the data of Figure 3.1 using the STARS foam model. Symbols are calculated points, not data.

Ma et al. (Ma et al. (2013), Ma et al. (2014)) present a method for fitting foam parameters to a more-limited set of data, specifically a plot of foam apparent viscosity as a function of foam quality at fixed total superficial velocity. On Figure 3.1, this data set amounts to a scan along a line joining the same values of superficial velocity on the two axes. This approach (Ma et al. (2013)) focuses on fitting a single datum with the largest ∇p, and it requires creating two new contour plots from model parameters. It ignores shear-thinning foam behaviour in the low-quality regime in the model fit. It can give two solutions (Ma et al. (2014)), so one is discarded to give a unique parameter fit. This set of parameters can then be optimized using a least-squares minimization routine that still excludes shear-thinning in the low-quality regime (Ma et al. (2014)). More recently, the least-squares optimization routine has been extended to include shear-thinning behaviour in the low-quality regime (cf. Kapetas et al. (2015)). One still needs a first guess of parameter values for this global optimization of parameter values, which could be provided by the approach of Ma et al. (2013) or that presented here.

In this Chapter we present a method for fitting parameters to the same sort of data, based on the approach of Cheng et al. (2000). This model fit likewise could be the initial guess for a least-squares search for optimal parameters. Our approach offers several advantages described in the Discussion Section below.

The effect of oil on foam is crucial to foam success in the field, but fitting foam parameters in the absence of oil is a necessary first step toward adjusting

the model for the effect of oil. Farajzadeh et al. (2012) discuss the challenges of fitting foam models for the effect of oil.

3.2   MODELS

Foam models come in two groups. "Population balance models" (Falls et al. (1988); Friedmann et al. (1991); Kovscek and Radke (1994); Kam et al. (2007)) represent the dynamics of bubble creation and destruction along with the effect of bubble size on gas mobility. The second group, implicit-texture (IT) models, represent the effects of bubble size implicitly through a gas-mobility-reduction factor that depends on water saturation, surfactant concentration, and other factors (Law et al. (1989); Patzek and Myhill (1989); Kular et al. (1989); Fisher et al. (1990); Islam and Farouq-Ali (1990); Mohammadi et al. (1993); Cheng et al. (2000)).

Models in the second group all implicitly assume local equilibrium (LE) between dynamic processes creating and destroying bubbles. For simplicity, we refer to these as "LE" models here, although population-balance models can also be restricted to assume local equilibrium (Myers and Radke (2000); Kam and Rossen (2003); Kovscek et al. (2010)). LE models are simpler to use, require fewer parameters and avoid some numerical difficulties encountered with population-balance models (though they are not free of numerical challenges themselves (Rossen (2013); Ma et al. (2014))). Fitting the parameters of LE models to data is the focus of this study.

One of the most widely used LE foam models is that in STARS, a foam simulator of the Computer Modeling Group (Cheng et al. (2000); Computer Modeling Group (2006)). In this study, the names of parameters will be those in this foam model. Similar models can be found in other simulators such as that in ECLIPSE or UTCHEM, but terminology and some details may vary, as described in Appendix B.

The foam model in STARS introduces a function FM, which controls the reduction in gas mobility, into Darcy's law for the gas phase:

$$u_t f_g = -\frac{k k_{rg}^f}{\mu_g} \nabla p = -\frac{k k_{rg} FM}{\mu_g} \nabla p \qquad (3.1)$$

where k_{rg}^f is the gas relative permeability in the presence of foam and k_{rg} is the gas relative permeability without foam. The latter is assumed to be a known function of phase saturations. The function FM is in turn a product of various other functions $(F_1, F_2, ...F_6)$, each of which is aimed at capturing different

physical effects. The complete function FM is given by (Cheng et al. (2000); Computer Modeling Group (2006))

$$FM = \frac{1}{1 + fmmob \cdot F_1 \cdot F_2 \cdot F_3 \cdot F_4 \cdot F_5 \cdot F_6} \qquad (3.2)$$

The parameter $fmmob$ is the reference gas mobility-reduction factor for wet foams. This parameter corresponds to the maximum attainable mobility reduction. The functions F_1 to F_6 are constrained to values less than or equal to 1, so that each function can only reduce the gas mobility-reduction factor, i.e. increase gas mobility. In this study only the functions F_2 and F_5 are considered; they represent the effects of water saturation and capillary number, respectively, on the behavior of foam. The other functions model the effect of surfactant concentration (F_1), oil saturation (F_3), gas velocity (F_4) and the critical capillary number (F_6); they are not taken into account in this study. The functions F_2 and F_5 are given by:

$$F_2 = 0.5 + \frac{\arctan(epdry \cdot (S_w - fmdry))}{\pi} \qquad (3.3)$$

$$\text{If } N_{ca} > fmcap, \quad F_5 = \left(\frac{fmcap}{N_{ca}}\right)^{epcap}; \qquad (3.4)$$
$$\text{else}, \quad F_5 = 1$$

with

$$N_{ca} \equiv \frac{k\nabla p}{\sigma_{wg}} \qquad (3.5)$$

where σ_{wg} is gas-water surface tension. Factor F_5 makes the low-quality regime non-Newtonian (Cheng et al. (2000)). UTCHEM accomplishes this through a similar factor based on gas superficial velocity; see Section B.1 in Appendix B.

In total (accounting for these two factors) the foam model contains five parameters ($fmmob, epdry, fmdry, fmcap$ and $epcap$).

- If the transition between regimes is abrupt, the parameter $fmdry$ is equal to S_w^*, the water saturation at which foam collapses.

- $epdry$ controls the abruptness of the foam collapse. Small values give a gradual transition between the two regimes, while larger values yield a sharper, albeit still continuous, transition. Reservoir simulators do not work efficiently with discontinuities in fluid properties, and this parame-

ter is commonly tuned so that it does not slow the simulator excessively. This can mean that the modeling of the transition between regimes is not abrupt enough to capture foam behavior seen in the laboratory.

- *epcap* captures shear-thinning behavior in the low quality regime.

- *fmcap* is a parameter that is set to the smallest capillary number expected to be encountered by foam in the simulation. It is thus not a foam parameter per se, though it does affect the values of other parameters.

In the most recent version of STARS, the parameter *fmdry* is renamed *sfdry*, and *epdry* is renamed *sfbet* (Coombe (2012)). The water saturation around which foam collapses (*fmdry*) is no longer treated a constant, but is a function of surfactant concentration, oil saturation, salt concentration, and capillary number. If one disables these other functionalities *sfdry* plays the same roll as *fmdry* as described here.

3.3   FITTING PARAMETERS TO A SINGLE SCAN OF FOAM QUALITY

The method of Cheng et al. (2000) requires a substantial amount of data at various gas and water superficial velocities (as in Figure 3.1) in order to fit model parameters. In some cases, more-limited data are available: specifically, a single scan of pressure gradient as a function of foam quality at fixed total superficial velocity. In this section we extend the method of Cheng et al. to this more-limited type of data set, illustrating with various data sets found in literature. One such data set is shown in **Figure 3.3**, which is from Ma et al. (2013). Ma et al. plot their results in terms of apparent viscosity instead of pressure gradient; the two sets of data are equivalent, as shown in Eq. 3.12 below. Ma et al. describe a method of fitting model parameters to the datum with the maximum measured pressure gradient, assuming a relatively gradual transition between the two regimes. The data in Figure 3.3 are from a sandpack foam-flooding experiment which was conducted with the outlet open to the atmosphere. Thus gas compression may have affected superficial velocity and foam quality in the experiment; for the purpose of illustrating our method of fitting the data we ignore this possibility. The nominal total superficial velocity was kept constant throughout these experiments at 20 ft/day ($7.1 \cdot 10^{-5} \ m/s$), but the injected gas fraction varied. Figure 3.3 clearly shows the two flow regimes (low- and high-quality; compare Figure 3.3 to ∇p along the dotted line in Figure 3.1). For low injected gas fractions, the pressure gradient increases with increasing gas fraction. It attains a maximum at a certain gas fraction and, for large gas fractions, the pressure gradient decreases as the gas fraction increases further.
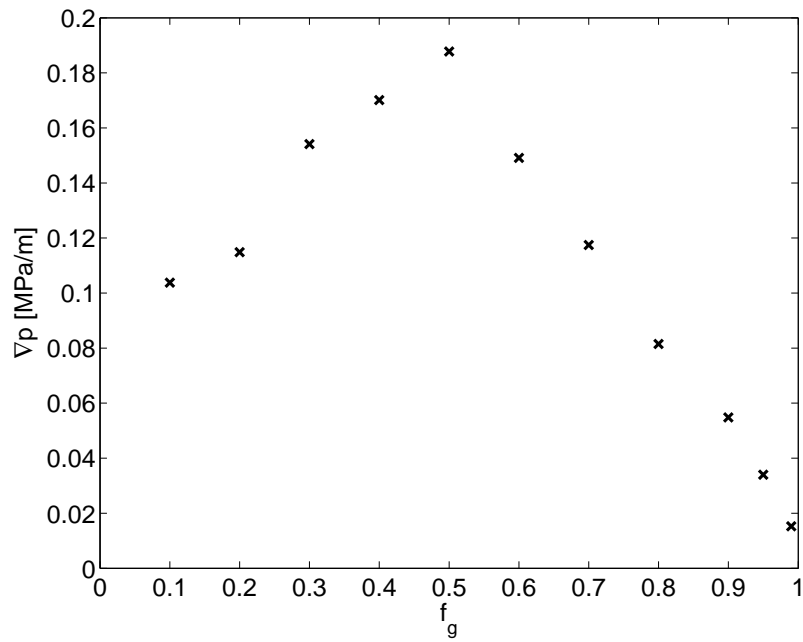
Figure 3.3: Scan of foam data at fixed total superficial velocity, after Ma et al. (2013)

Briefly, the method we propose is as follows. One must know the foam-free relative-permeability functions $k_{rw}(S_w)$ and $k_{rg}(S_w)$ in advance.

1. Plot the best fit through the data in a plot of ∇p v. f_g, as follows:

   - for large values of f_g (the high-quality regime), plot a straight line passing through $(f_g, \nabla p) = (1,0)$

   - for smaller value of f_g (the low-quality regime), plot a convex curve through the data and passing through $(f_g, \nabla p) = (0,0)$

   - The estimate of f_g^* is the intersection of the line and the curve.

2. Determine $fmdry$ from the slope of the straight line through the high-quality-regime data, using Darcy's law for the aqueous phase.

3. Determine $fmmob$ from Darcy's law for the gas phase using the value of ∇p at f_g^*.

4. Select a point on the curve through the low-quality-regime data some distance from f_g^*. Fit $epcap$ to this datum as described below. Select $fmcap$ and adjust $fmmob$ according to the range of capillary numbers expected in the simulation, as described below.

5. Pick the largest value of $epdry$ consistent with acceptable simulator performance.

6. Plot the resulting fits to the low-quality- and high-quality-regime data to verify the fit.

We illustrate the approach using the data of Ma et al. (2013). **Appendix B** and **Table 3.2** below provide fluid and transport properties used in this model fit in addition to the ∇p data. The first step in fitting the model parameters is determining the foam quality at the transition between the two regimes (f_g^*). Behavior is Newtonian in the high-quality regime (according to the model), and therefore data should fit a straight line through (f_g, ∇p) = (1,0). The first step then is to plot the best possible straight line through the data in the high-quality regime (f_g greater than that at the maximum in ∇p). If the data cannot be fit well with a straight line through (1,0), it is an indication of either non-Newtonian behavior in the high-quality regime or a less-abrupt collapse of foam at S_w^*; see discussion below.

In the low-quality regime strongly shear thinning behavior is expected: a straight line thought (0,0) would not be expected to fit the data in this regime. Instead we propose that one initially plot a free-hand convex curve to fit the data in this regime ($f_g < f_g^*$) which also passes through the origin ($\nabla p = 0$ for $f_g = 0$). The intersection between the straight line in the high quality regime and the convex curve in the low quality regime is the estimate for f_g^*. **Figure 3.4** illustrates this method using the data of Ma et al. (2013), where the estimated value of f_g^* is 0.54.

The second step is to determine S_w^* from the straight-line fit to the line through the high-quality-regime data; throughout this regime $S_w = S_w^*$. Darcy's law applied to the water phase at f_g^* gives

$$u_t \left(1 - f_g^* \right) = \frac{k k_{rw} \left(S_w^* \right)}{\mu_w} \nabla p \left(f_g^* \right) \tag{3.6}$$

from which (using the known function $k_{rw}(S_w)$) one can determine S_w^*. From the straight line through the data of Ma et al. (2013) we obtain $S_w^* = fmdry = 0.130$. The third step is to determine the value of $fmmob$ from the pressure gradient at f_g^* using Darcy's law for the gas phase. Because the transition between regimes is abrupt, at f_g^*, $S_w = S_w^*$ and

$$FM \left(f_g^* \right) = \frac{1}{1 + fmmob} \tag{3.7}$$
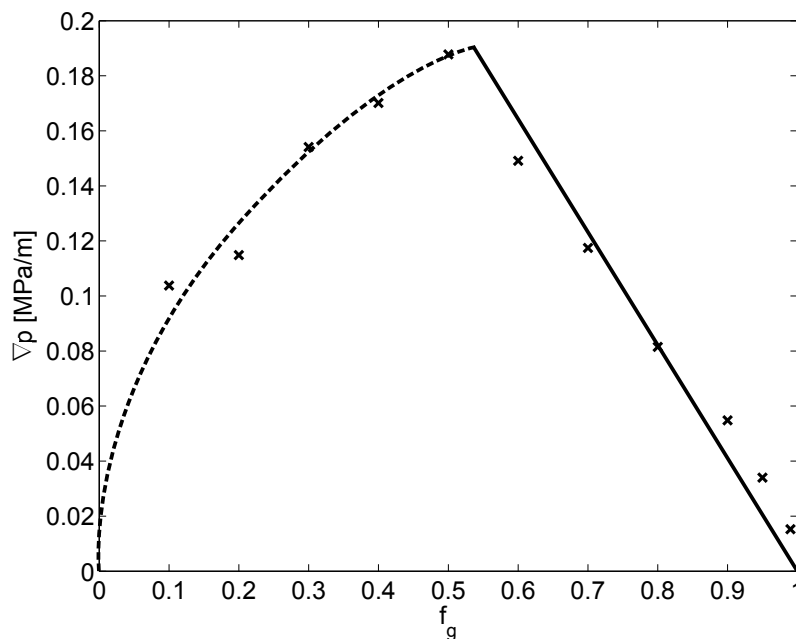
Figure 3.4: Data of Ma et al. (2013). Data points are shown as crosses. Initial, hand-drawn, fits to data in the low- and high-quality regimes are shown as a convex, dashed curve and a solid straight line respectively.

The value of $fmmob$ can be obtained from Darcy's law for the gas phase (Eq. (3.1)) at f_g^*:

$$FM\left(f_g^*\right) = \frac{1}{1 + fmmob} = \frac{u_t f_g^* \mu_g}{kk_{rg}\left(S_w^*\right) \nabla p\left(f_g^*\right)} \tag{3.8}$$

Inserting $S_w^* = 0.130$ into Eq. (3.8) gives $FM(f_g^*) = 3.14 \cdot 10^{-5}$ and thus $fmmob = 3.18 \cdot 10^4$. As mentioned, the value of $epdry$ is commonly chosen such that the simulator can execute efficiently. In this study we assume that the transition between regimes is abrupt, which corresponds to a large value of $epdry$. We chose $epdry = 100,000$ in most of the fits presented here. The resulting fit to the data of Ma et al. (2013), prior to consideration of shear-thinning in the low-quality regime, is given in **Figure 3.5**.

The fit accurately captures the maximum pressure gradient and shows good agreement with the data in the high-quality regime. In the low-quality regime, the fit is less accurate. The model approximates a straight line whereas the data show distinct deviation from a straight line through the origin. This suggests shear-thinning behavior in the low-quality regime, as reported previously (Alvarez et al. (2001)).

Therefore, the fourth step extends the model using the capillary-number-dependent function (F_5) (Eq. (3.4)). To simplify the determination of the pa-
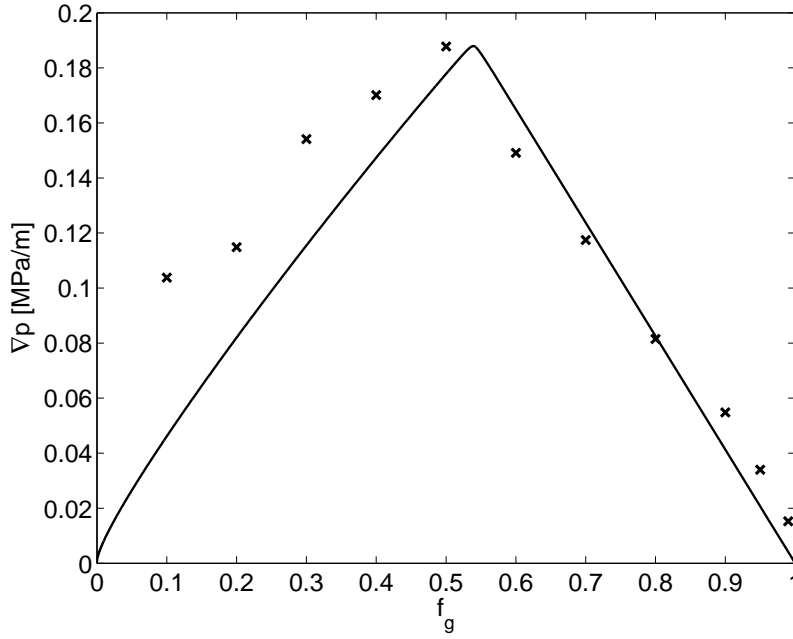
Figure 3.5: Model fit to data of Ma et al. (2013) using only the water-saturation-dependent function (F2). Data points are shown as crosses. The solid line shows the model fit.

rameter $epcap$ several assumptions are made. First, we continue to assume that the transition between regimes is abrupt, i.e. we assume a very large value of $epdry$. This means that the function F_2 equals 1 throughout the low-quality regime, and can be neglected when fitting the model parameters in this regime. Second, we further assume for simplicity that foam-free gas relative permeability is nearly constant throughout the low-quality regime and is equal to its value at S_w^*. In the final fit obtained below foam-free gas relative permeability changes by only around 10% for the saturations represented by the low-quality data, so initially fixing its value does not cause great errors in the model parameters. We pick one point in the curve through the low-quality data not too close to f_g^*, at a value of f_g we call f_g^+. Our choice is shown in **Figure 3.6**. With these assumptions, Darcy's law for the gas phase, applied to this datum, gives:

$$
u_t f_g^+ = \frac{kk_{rg}\left(S_w^*\right)\nabla p\left(f_g^+\right)}{\mu_g}\frac{1}{1 + fmmob\left(\frac{\nabla p\left(f_g^*\right)}{\nabla p\left(f_g^+\right)}\right)^{epcap}}
\tag{3.9}
$$

Note that for the data to be fit, k and σ_{wg} are fixed, so the ratio of capillary numbers in Eq. (3.4) equals the ratio of pressure gradients. This equation can be rearranged into an expression for $epcap$:

$$epcap = \frac{\log\left(\frac{kk_{rg}(S_w^*)\nabla p\left(f_g^+\right)-u_t f_g^+ \mu_g}{u_t f_g^+ \mu_g fmmob}\right)}{\log\left(\frac{\nabla p\left(f_g^*\right)}{\nabla p\left(f_g^+\right)}\right)} \tag{3.10}$$

This approach yields the value of $epcap$. Since F_5 is constrained to values less than 1, the value of $fmcap$ cannot be set by ∇p at f_g^*, the experimentally observed maximum value of ∇p; F_5 would then simply return a value of 1 (Eq. (3.4)) for smaller values of pressure gradient, including those in the low-quality regime used to fit the parameters. Instead, $fmcap$ should be based on either the lowest value of p expected in the simulation, or a lower limit below which non-Newtonian effects are not expected; call this value ∇p_{lim}. In addition, the value of $fmmob$ must be adjusted; let $fmmob^*$ be the value derived above at f_g^*; the new value of $fmmob$ is given by

$$fmmob = fmmob^* \cdot \left(\frac{\nabla p\left(f_g^*\right)}{\nabla p_{lim}}\right)^{epcap} \tag{3.11}$$

For illustration, here we choose $\nabla p_{lim} = \nabla p(f_g^*)/5$. Allowing for shear-thinning in the low-quality regime increases the value of $fmmob$, which can be problematic for simulators at low superficial velocity. The resulting fit for ∇p in the low-quality regime is given by the following expression, which is an approximation for the case $fmmob >> 1$, and illustrated in Figure 3.6.

For comparison, **Figure 3.7** shows the fit of Ma et al. (2014) to the same data, plotted here (as in their paper) in terms of apparent viscosity instead of ∇p. After the manual search for parameters using the approach of Ma et al. (2013), Ma et al. (2014) apply a least-squares optimization to find values of $fmmob$, $fmdry$ and $epdry$, but set $epcap$ to zero; in other words, it assumes Newtonian behavior in the low-quality regime. The smaller value of $epdry$ gives a more gradual transition between regimes, which partially makes up for the lack of shear-thinning assumed in the low-quality regime. Nonetheless, the fit to the trend of the data in the low-quality regime is poor because of the Newtonian behavior assumed there. As noted by Ma et al., the shift in parameter values brought about by matching the low-quality regime has shifted the foam quality at the maximum in apparent viscosity by over 10%.
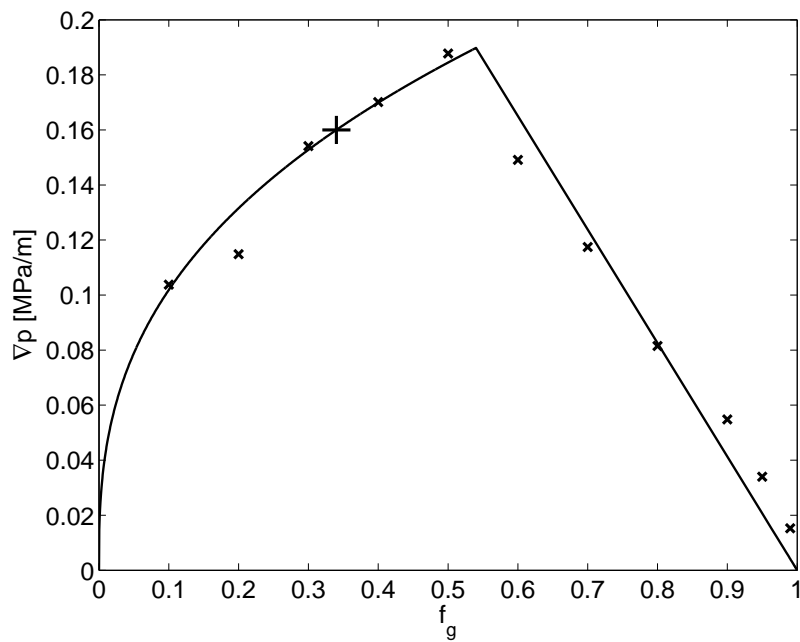
Figure 3.6: Model fit to data of Ma et al. (2013) including the capillary-number-dependent function (F_5) in the low-quality regime. Data points in the low- and high-quality regimes are shown by crosses. The solid line shows the model fit. The '+' sign is the chosen value of $(f_g^+, \nabla p(f_g^+))$.
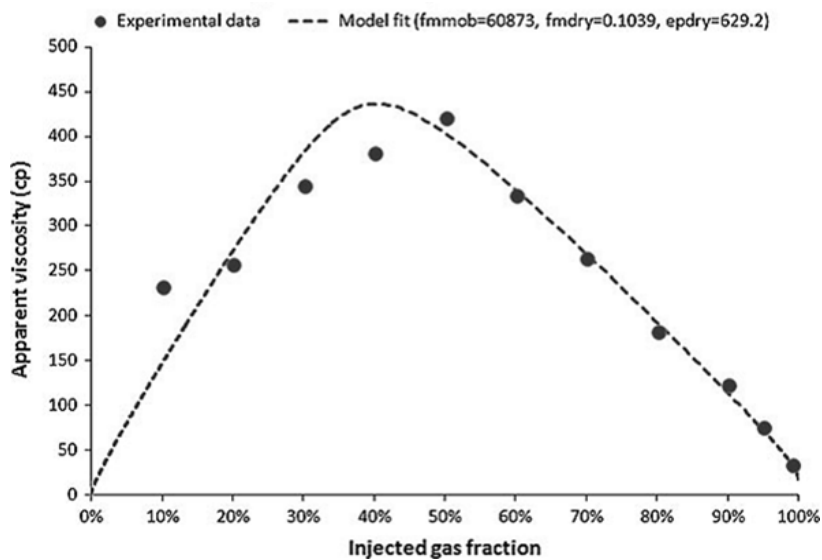
Figure 3.7: Model fit of Ma et al. (2014) to their data, using least-squares optimization of fit excluding non-Newtonian behaviour in the low-quality regime: $fmmob = 6.09 \cdot 10^4$, and $fmdry = 0.104, epdry = 629, epcap = 0$. The difference in $fmdry$ values between Table 3.3 and Figure 3.7 in part reflects a difference in relative-permeability functions assumed; see Appendix B.

Table 3.1: Comparison of results from this study with Cheng et al. (2000)

	CHENG ET AL. (2000)	THIS STUDY
$fmmob$	$6.84 \cdot 10^5$†	$6.63 \cdot 10^5$
$fmmob^*$		$4.27 \cdot 10^4$
$epdry$	$2.00 \cdot 10^4$	$2.00 \cdot 10^4$
$fmdry$	0.316	0.311
$fmcap$	$2.46 \cdot 10^{-5}$	$2.46 \cdot 10^{-5}$
$epcap$	1.12	1.13

† Note: the value of $fmmob$ is different from that in Cheng et al. (2000). It has been adjusted using the method outlined in the text.

3.4 OTHER EXAMPLES

We illustrate the fit of model parameters using data from various other published studies. The data of Alvarez et al. (2001) and fit of Cheng et al. (2000) are shown in Figures 3.1 and 3.2. Here we take a scan of ∇p at fixed a superficial velocity of 2.5 ft/day ($8.8 \cdot 10^{-6}$ m/s). The data in this case are values read off ∇p contours on the diagonal line on Figure 3.1. These experiments were carried out using Berea sandstone rather than the sandpacks that were used in the experiments of Ma et al. Therefore, different relative-permeability functions were used, as described in Appendix B. Figure 3.8 show the model fit with and without including the effects of shear-thinning in the low-quality regime. In this case we use a value of $epdry$ of 20,000 for direct comparison with fit by Cheng et al. (2000) and also use the same value of $fmcap$ as in that study.

Table 3.1 compares the results obtained here to those of Cheng et al. (2000). The value of the parameter $fmcap$ is calculated using a surface tension $\sigma_{wg} = 0.03$ N/m, a typical value for surfactant solutions against N_2 gas at room temperature and atmospheric pressure (Rossen (1996)). The fit of Cheng et al. to the data in Figure 3.1 give similar values of $epcap$ and $fmdry$ to those we obtain from a scan of foam quality at a single total superficial velocity. In the course of making our fit we discovered an error in the calculations of Cheng et al., probably arising from a units conversion from (1/ft) to (1/m); that is, the values of ∇p from their model in the low-quality regime are factor 3.28 lower than the ∇p data. The value of $fmmob$ is therefore too small by a factor $(3.28)^{(1+epcap)}$. When corrected for this error (Table 3.1) our value of $fmmob$ is close to theirs.

Figure 3.8: Model fit to the data of Alvarez et al. (2001) including the capillary-number-dependent function F_5. Parameter values are $fmmob = 6.63 \cdot 10^5$, $fmdry = 0.311$, $epcap = 1.13$, $fmcap = 2.46 \cdot 10^{-5}$. The '+' sign is the chosen value of $(f_g^+, \nabla p(f_g^+))$.

Moradi-Araghi et al. (1997) quantify foaming performance with plots of gas fraction (f_g) vs. mobility reduction factor RF, defined as the ratio of the pressure drop during foam injection to that during brine injection (i.e. $RF \equiv \Delta p_{foam}/\Delta p_{brine}$). To convert RF to a pressure gradient, the total superficial velocity u_t is required. However, this is not provided in the paper. Instead we plot these data as gas fraction vs. apparent viscosity of foam μ_{app}. The latter is defined by

$$\mu_{app} = \frac{k\nabla p}{u_t} \equiv RF \cdot \mu_w \tag{3.12}$$

Thus the mobility-reduction factor RF can easily be converted to apparent viscosity using brine viscosity, but not to ∇p without knowing u_t. Since the ratio $(\nabla p/u_t) = (RF \cdot \mu_w/k)$ occurs in Eqs. (3.6), (3.8), (3.9) and (3.10) it is possible to solve for model parameters (except $fmcap$) without knowing u_t. The experiments of Moradi-Araghi et al. were performed at a temperature of 98°F (36.7°C) at which brine viscosity is approximately 0.69 mPa·s. These experiments were performed in sandstone so we use the same relative-permeability functions as for the model fits to the data by Alvarez et al. (cf. **Table B.2**). The

resulting model fit is shown in **Figure 3.9**. Other data from Moradi-Araghi for foam in a 496-md core are fit in **Figure 3.10**.

Another recent data set can be found in Chabert et al. (2012), who conducted CO_2 foam flooding tests in low-permeability (20 mD) Indiana limestone cores. For carbonates we use yet another set of relative-permeability functions, as described in Appendix B. The fit to the data of Chabert et al. is given in **Figure 3.11**. In this case foam reduces gas mobility much less than in the other cases ($fmmob = 5.50$), and a satisfactory fit is obtained to low-quality-regime data without adjusting for non-Newtonian behavior there; thus we make no fit for $epcap$ or $fmcap$. In this case the pressure gradient in the absence of foam ($f_g \rightarrow 0$ or 1) is of the same order of magnitude as that with foam. The kink in the predicted curve for $\nabla p(f_g)$ for f_g close to 1 represents $S_w < fmdry$ - foam drier than the high-quality regime. (Such behaviour is suggested by Alvarez et al. at very large f_g in their case). The trend predicted for the high-quality regime remains a straight line through $(f_g, \nabla p) = (1, 0)$.

The fit in Figure 3.11 is not very good, at least in part because the data themselves are scattered. The datum at $f_g = 0.6$ in particular is off the trend of the others. One advantage of our approach is that the quality of the fit is apparent from the start of the process (cf. Figure 3.4), even before parameter values are estimated.

An overview of the input parameters used is given in Table 3.2 and all of the derived foam parameter values are given in Table 3.3. From the fitted parameter values it is clear that in the experiments of Chabert both the mobility reduction by full-strength foam ($fmmob$) is less and the onset of foam collapse occurs at higher water saturation ($fmdry$) than in the other experiments. When differences are more subtle, quantitative comparisons of $fmmob$ between cases is difficult because its value is affected by the choice of the reference pressure gradient ∇p_{lim} (Eq. (3.11)). As noted, this reference state should be the smallest value of ∇p expected to be encountered in the simulation. This could be orders of magnitude less than in the experiments. This difference, combined with shear-thinning behavior ($epcap > 0$) can greatly affect the fitted value of $fmmob$ between cases.

The value of $fmdry$ reflects the limiting capillary pressure P_c^* (Khatib et al. (1988); Cheng et al. (2000)). Making this link quantitative requires knowing the capillary-pressure function $P_c(S_w)$ for experiment. It is likely, for instance, that the smaller value of $fmdry$ in the fit to the data of Ma et al. than to the others in Table 3.3 reflects at least in part lower capillary pressure in a sandpack compared to the other formations. Therefore the difference in P_c^* between these cases is not clear from these data alone.
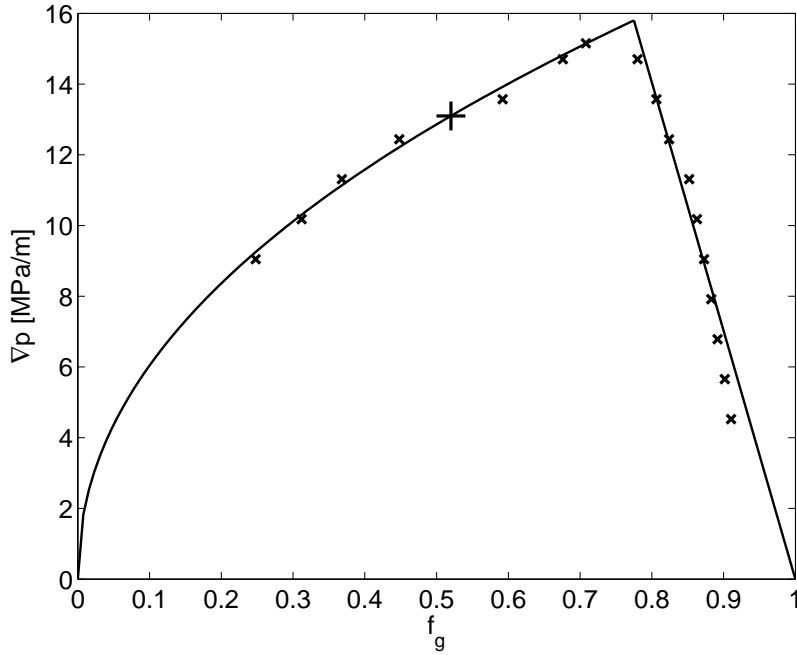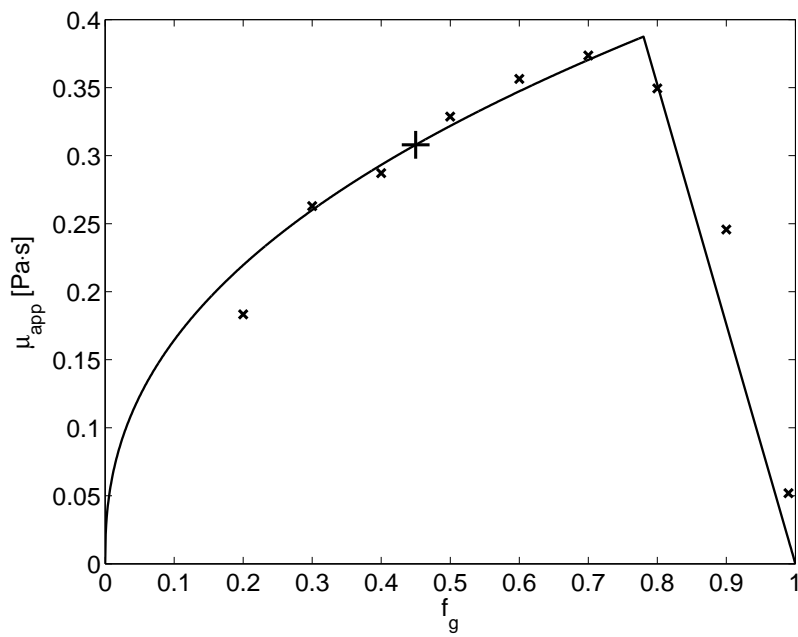
Figure 3.9: Model fit to the data of Moradi-Araghi et al. (1997) including the capillary-number-dependent function F_5. Parameter values are $fmmob = 5.26 \cdot 10^4, fmdry = 0.336, epcap = 1.40$. The '+' sign is the chosen value of $(f_g^+, \mu_{app}(f_g^+))$
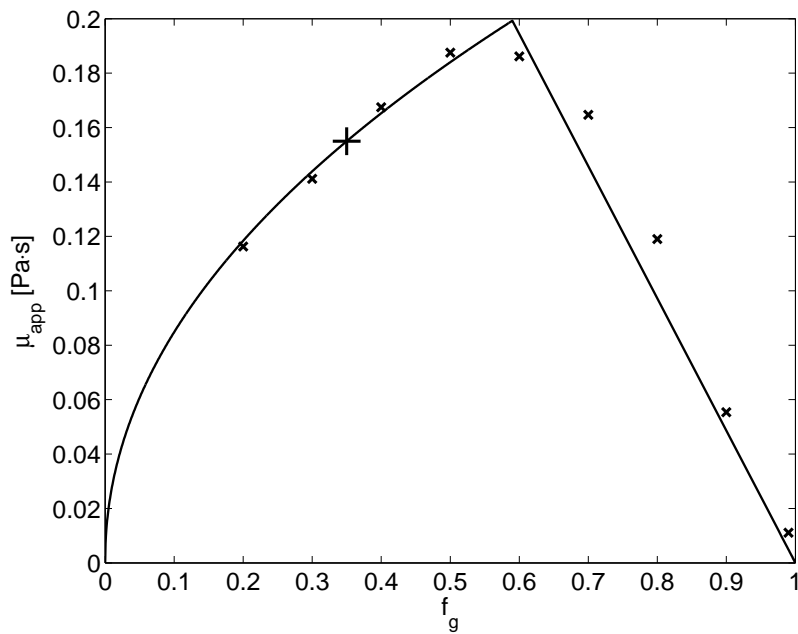
Figure 3.10: Model fit to the data of Moradi-Araghi et al. (1997) including the capillary-number-dependent function F_5. Parameter values are $fmmob = 1.86 \cdot 10^4, fmdry = 0.385, epcap = 1.08$. The '+' sign is the chosen value of $(f_g^+, \mu_{app}(f_g^+))$
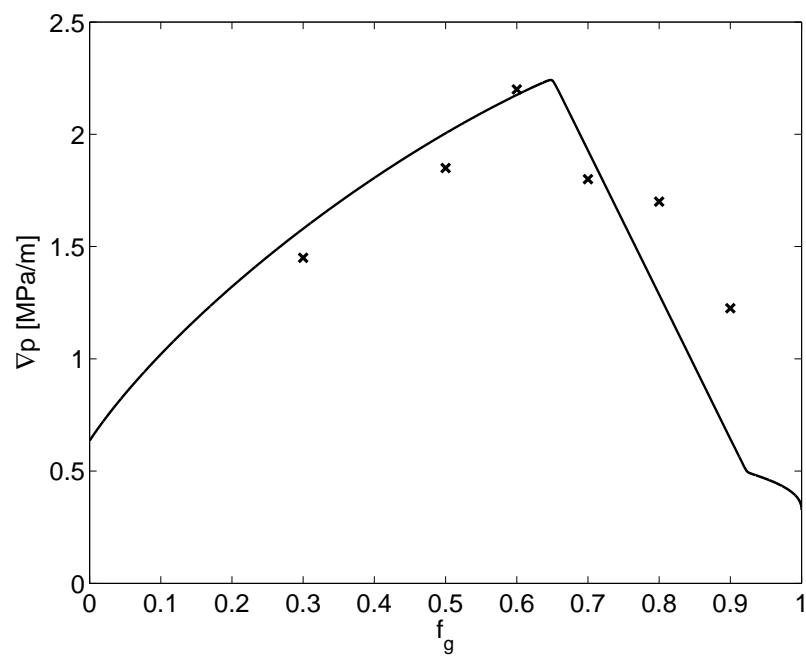
Figure 3.11: Model fit to the data of Chabert et al. (2012) using only the water-saturation-dependent function F2. Parameter values are fmmob = 5.5, fmdry = 0.550, $f_g^* = 0.65$.

Table 3.2: Overview of input parameters for all of the investigated studies

	MA ET AL. (2013)	ALVAREZ ET AL. (2001)	MORADI-ARAGHI (1) (1997)	MORADI-ARAGHI (2) (1997)	CHABERT ET AL. (2012)
porous medium	Unconsolidated sand	Sandstone	Sandstone	Sandstone	Sandstone
μ_w [Pa·s]	$1.0 \cdot 10^{-3}$	$0.70 \cdot 10^{-3}$	$0.69 \cdot 10^{-3}$	$0.69 \cdot 10^{-3}$	$0.65 \cdot 10^{-3}$
μ_g [Pa·s]	$2.0 \cdot 10^{-5}$	$2.0 \cdot 10^{-5}$	$6.0 \cdot 10^{-5}$	$6.0 \cdot 10^{-5}$	$6.0 \cdot 10^{-5}$
Type of gas	Air	N_2	CO_2	CO_2	CO_2
σ_{wg} [N/m]	0.030	0.030	0.005	0.005	0.005
u_t [m/s]	$7.1 \cdot 10^{-5}$	$8.8 \cdot 10^{-5}$	Unknown	Unknown	$5.4 \cdot 10^{-6}$
T [°C]	20	20	37	37	40
k [m^2]	$1.58 \cdot 10^{-10}$	$5.30 \cdot 10^{-13}$	$5.52 \cdot 10^{-13}$	$4.96 \cdot 10^{-13}$	$2.0 \cdot 10^{-14}$
Backpressure [Pa]	0	$4.14 \cdot 10^{6}$	$1.38 \cdot 10^{7}$	$1.38 \cdot 10^{7}$	$1.30 \cdot 10^{7}$

Table 3.3: Fitted values of STARS foam model parameters

	MA ET AL. (2013)	ALVAREZ ET AL. (2001)	MORADI-ARAGHI ET AL. (1) (1997)	MORADI-ARAGHI ET AL. (2) (1997)	CHABERT ET AL. (2012)
$fmmob$	$4.99 \cdot 10^5$	$6.63 \cdot 10^5$	$5.26 \cdot 10^4$	$1.86 \cdot 10^4$	5.50
$fmmob^*$	$3.18 \cdot 10^4$	$4.27 \cdot 10^4$	$5.57 \cdot 10^3$	$3.28 \cdot 10^3$	-
$epdry$	$1.00 \cdot 10^5$	$2.00 \cdot 10^4$	$1.00 \cdot 10^5$	$1.00 \cdot 10^5$	$1.00 \cdot 10^5$
$fmdry$	0.130	0.311	0.336	0.385	0.550
$fmcap$	$2.00 \cdot 10^{-4}$	$2.46 \cdot 10^{-5}$	Unknown†	Unknown†	-
$epcap$	1.71	1.13	1.40	1.08	-
f_g^*	0.54	0.775	0.78	0.59	0.65

† Note: - N_{ca} and $fmcap$ are unknown because ut is unspecified. We can still fit non-Newtonian behavior using ratios of RF, which at fixed superficial velocity equal the ratios of N_{ca}.

3.5   DISCUSSION

The model-fitting approach presented here has the following advantages:

1. The approach is simple. It can be carried out directly from a plot of the raw data using a pencil and a calculator.

2. It begins by making the best fit to both regimes based on *all* data in that regime. It allows that the transition in regimes, and the maximum in ∇p, may occur between measured values of f_g.

3. It accounts for the effect of shear-thinning behaviour on the low-quality regime.

4. The approach directly incorporates the assumptions of the STARS foam model into the process from the first step (cf. Figure 3.4). Excessive scatter or a mismatch between the data and model assumptions is immediately apparent.

5. The physical significance of each parameter value (*fmdry* in the high-quality regime, *fmmob* and *epcap* in the low-quality regime) is immediately apparent throughout the fitting process.

The approach does suffer from the following shortcomings:

1. The fit obtained is not necessarily the least-squares fit to the data. The user must judge for himself in the last step (6) whether the fit is adequate.

2. The approach assumes an abrupt transition between high- and low-quality regimes, i.e. a large value of *epdry* in the STARS model. The parameters quickly obtained by this method can provide the initial guess for a computer-based least-squares fit of all parameters, including a smaller value of *epdry*, and a check on the parameters so obtained. See Kapetas et al. (2015) for examples.

3. The method proposed here is appropriate for a process of foam injection with finite injected water fraction. In a SAG (surfactant-alternating-gas) process, behavior during gas injection depends on foam properties at very low water fraction (Zhou and Rossen (1995); Rossen et al. (1999); Shan and Rossen (2004)); properties at larger water fraction are relatively unimportant to the process, and data should be fit specifically to this low range of water fraction (cf. Kibodeaux and Rossen (1997); Xu and Rossen (2004); Rossen and Bruining (2007)). Chapter 4 addresses fitting data for application in SAG foam processes (cf. also Rossen and Boeije ((SPE 165282)).

4. A scan of foam quality at a single superficial velocity is a more limited data set than that used by Cheng et al. (2000). In using such a data set, one risks failing to notice deviations from the assumptions of the foam model. Not all foam data show horizontal ∇p contours in the low-quality regime, for instance (Kim et al. (2005)). A scan of foam quality at fixed superficial velocity could fail to detect this deviation.

3.6 CONCLUSIONS

We present a method for fitting parameters in the STARS foam model (excluding the effect of oil) to data for pressure gradient ∇p (or, equivalently, resistance factor RF or apparent viscosity μ_{app}) as a function of foam quality at a single superficial velocity. The approach estimates the non-Newtonian behavior in the low-quality regime from the same set of data. The same method would apply to the parameters of the foam model in ECLIPSE, and a similar method to those in UTCHEM. Its advantages are simplicity and directness. The model fit would be appropriate for an EOR process involving foam injection at finite water fraction, but not a SAG foam process involving large slugs of gas and liquid. For the latter process, model parameters should be fit to data relevant to that process, i.e. at extremely high foam quality.

This approach assumes an abrupt transition between high- and low-quality foam regimes, i.e. a large value of *epdry*. The parameter values quickly obtained by this method can provide the initial guess for a computer-based least-squares fit of all parameters, including a smaller value of *epdry*, and a check on the parameters so obtained.

4

FITTING FOAM SIMULATION MODEL PARAMETERS TO DATA II: SAG FOAM APPLICATIONS

4.1 INTRODUCTION

Gases (supercritical CO_2, hydrocarbon gases, N_2 or steam) injected for enhanced oil recovery (EOR) can be very effective at displacing oil where gas sweeps. However ultimate oil recovery is reduced by poor sweep efficiency (Lake et al. (2014)). Sweep efficiency is poor because of reservoir heterogeneity, gravity segregation of gas to an override zone, and viscous instability between gas and the more-viscous fluids it displaces. Foam can address all three problems and improve sweep efficiency of EOR processes where gas is injected (Schramm (1994); Kovscek and Radke (1994); Rossen (1996)). Foam can be placed in a reservoir in four ways:

1. In co-injection, gas and aqueous surfactant solution are injected simultaneously from a single well. Foam forms in the surface facilities where the fluids meet, in the tubing, or shortly after the fluids enter the formation.

2. In surfactant-alternating-gas or SAG injection, gas and surfactant solution are injected in separate slugs from a single well. Foam forms in the formation where gas meets previously injected surfactant solution, or when surfactant solution meets previously injected gas.

3. It is possible to dissolve some surfactants directly into supercritical CO_2 (Le et al. (2008); Xing et al. (2012)). Then there is no need to inject aqueous surfactant solution; injected CO_2 with dissolved surfactant forms foam as it meets water in the formation.

4. Surfactant solution and gas can be injected simultaneously, but from different sections of a vertical well (gas injected below the surfactant solution), or from parallel horizontal wells (gas injected from the lower well) (Stone (2004); Rossen et al. (2010)). Foam forms in the reservoir where gas and surfactant solution meet.

Modeling and upscaling a foam process from laboratory experiments is essential for designing a field application of foam. The effect of oil on foam is of course a key factor, but modeling foam without oil is a necessary first step to modeling foam with oil, and is still a challenge. In this work we focus on fitting simulation model parameters to foam behavior without oil. Farajzadeh et al. (2012) discuss the issues arising in fitting foam-model parameters describing the effect of oil on foam.

Foam simulation models are of two types: Population-balance models (Falls et al. (1988); Friedmann et al. (1991); Kovscek and Radke (1994); Kam et al. (2007)) represent the dynamics of bubble creation and destruction explicitly along with the effect of bubble size on gas mobility. The second group represents the effects of bubble size implicitly through a gas-mobility-reduction factor that depends on water saturation, surfactant concentration, and other factors. A wide variety of models in the second group exist, with different levels of complexity (Law et al. (1989); Patzek and Myhill (1989); Kular et al. (1989); Fisher et al. (1990); Islam and Farouq-Ali (1990); Mohammadi and Coombe (1992); Cheng et al. (2000)). In recent years, most of these allow for the abrupt collapse of foam at a limiting capillary pressure or limiting water saturation (Khatib et al. (1988)). Models in the second group all implicitly assume local equilibrium (LE) between dynamic processes creating and destroying bubbles. For simplicity, we refer to these as "LE" models here, although population-balance models can also be restricted to assume local equilibrium (Ettinger and Radke (1992); Myers and Radke (2000); Kam and Rossen (2003); Kovscek et al. (2010)).

Population-balance models are more complex than LE foam models. These models face numerical challenges, because of their complexity and the differing time scales of bubble population dynamics and the overall displacement. LE foam models that account for an abrupt increase in gas mobility at a limiting capillary pressure or water saturation represent the two steady-state strong-foam regimes at high and low foam quality (flowing gas fraction) as well as do the population-balance models (Cheng et al. (2000); Ma et al. (2013)).

In Appendix B we describe and relate the parameters in three popular foam models, those in STARS, ECLIPSE, and UTCHEM, that account for a limiting water saturation. Dong and Rossen (2007) show the importance of the functional form chosen for this effect for modeling SAG processes. At this time,

only population-balance models can represent multiple foam steady states, the dynamics of foam creation and propagation at a shock front, and the creation of foam at the entrance of the porous medium. However, unless this is the focus of study, current LE foam models are as capable of representing foam behavior as current population-balance models. Here we focus on the widely used STARS local-equilibrium foam model (Cheng et al. (2000); Computer Modeling Group (2006)), described in chapter 3.

The approach to fitting model parameters to foam data depends on the injection method envisioned in field application. In Chapter 3 (also published in Boeije and Rossen (2015)) we describe how to fit parameters describing the properties of foam without oil to data for pressure gradient as a function of foam quality at fixed total superficial velocity (see also Cheng et al. (2000); Ma et al. (2013)). This approach would be appropriate for a co-injection process.

In a SAG foam process, foam behavior during the period of gas injection is crucial. A SAG process with large slugs of gas and liquid has significant advantages in injectivity and overcoming gravity override (Shan and Rossen (2004); Kloet et al. (2009); Faisal et al. (2009); Leeftink et al. (2015)). Even in a SAG process with relatively small slugs of gas and liquid, if foam fails to form or collapses during the period of gas injection, gas would rapidly segregate vertically before injection of the next slug of surfactant solution. Whatever the slug size, injectivity depends primarily on mobility very near the well, where even small slugs of surfactant and gas are large compared to the region of interest. Thus it is crucial to model the period of gas injection in SAG accurately.

On the laboratory scale, especially during the first pore volume of gas injection in a SAG coreflood, local equilibrium may not apply (Kapetas et al. (2014)). At this time, however, we are aware of only two studies attempting to fit a population-balance model directly to SAG coreflood data (Kovscek et al. (1995a); Kapetas et al. (2014)). Most published population-balance models come quickly to local equilibrium (Rossen et al. (1999); Kovscek et al. (2010)). Moreover, the period of slug injection in a SAG process is much longer than a typical laboratory coreflood, so it is likely that LE applies to most of this period. Therefore here we fit an LE foam model to steady-state data, where LE is known to apply, and infer the behavior of a SAG flood assuming LE applies in the field.

In this study, we neglect the parameters in STARS representing non-Newtonian behavior in the low-quality regime, *epcap* and *fmcap* (as outlined in Chapter 3; also Cheng et al. (2000)). We neglect those parameters, we focus on the gas-injection cycle of a SAG flood, which implies that foam is predominantly in the high-quality regime (i.e. high gas fractional flow) (Zhou and Rossen (1995); Shan and Rossen (2004); Rossen and Boeije ((SPE 165282)). In this regime, the dryout function F_2 is the dominant mechanism in foam rheology (Cheng et al.

(2000), which is why we limit our modeling to the dryout function. Leeftink et al. (2015) show that, while other effects such as shear thinning are observed in this regime, they do not dominate foam rheology. Thus for SAG foam applications, the function FM reduces to.

$$FM = \frac{1}{1 + fmmob \cdot F_2} \qquad (4.1)$$

As illustrated in **Figure 4.1** (from Rossen et al. (1999)) below, during gas injection in a SAG process gas fractional flow is nearly 1 and foam resides in the high-quality regime, where these parameters ($fmcap$ and $epcap$ play little part. Thus we focus on remaining parameters $fmmob$, $fmdry$, and $epdry$.

Further from the well, in a process with many small slugs, individual gas and liquid slugs merge into a bank with uniform water fraction approximating that fixed by the WAG ratio (Walsh and Lake (1989); Faisal et al. (2009)). To represent this region, a foam model must represent intermediate values of water fraction, and not just behavior at the lowest water fractional flows.

Fractional-flow theory and simulation show that most of the data gathered in a scan of foam quality is irrelevant to the period of gas injection in a SAG process (Rossen et al. (1999). The application of fractional-flow theory, or the method of characteristics, to foam processes is described more fully elsewhere (Zhou and Rossen (1995); Shan and Rossen (2004)). Fractional-flow theory assumes a 1D displacement, incompressible phases, absence of dispersion (including capillary dispersion), and immediate attainment of local equilibrium (Lake et al., 2014). Despite its limitations, fractional-flow theory provides numerous key insights to application of foam and other EOR processes. Simulations in 1D linear or radial flow match the predictions of fractional-flow theory as long as the simulations are conducted with sufficient grid resolution and with the same assumptions made in fractional-flow theory (in particular, local equilibrium and incompressible gas) (Rossen et al. (1999); Shan and Rossen (2004)).

To predict a SAG foam displacement using fractional-flow theory one begins by plotting the steady-state fractional flow of water as a function of water saturation. In a SAG process, a slug of surfactant precedes the injection of gas, and surfactant is present at uniform concentration throughout the water phase in the region of interest. Therefore only one fractional-flow curve applies, that for foam. An example is shown in Figure 4.1. On this curve one plots the initial state of the reservoir as point I. Here we assume for simplicity that this is the first slug of gas injected; no gas is present in the reservoir and point I lies at water saturation $S_w = 1$. One then plots the state of the fluids injected into the reservoir J, determined by the water fraction of the injected fluids. During gas

injection in a SAG process, $f_w = 0$, and that state is therefore at irreducible water saturation S_{wr}. The solution for the displacement is represented as a path along the fractional-flow curve from J to I with monotonically increasing slope df_w/dS_w. In the displacement, fixed water saturations travel with dimensionless velocity equal to the slope of the fractional-flow function df_w/dS_w at that saturation. In radial flow, dimensionless position x_D is given by

$$x_D \equiv \frac{r^2 - r_w^2}{r_e^2 - r_w^2} \qquad (4.2)$$

where r is radial position and r_w and r_e the radii of the wellbore and the region of interest in the reservoir, respectively. Dimensionless time is expressed in pore volumes injected, that is, total fluid volume injected divided by the pore volume of the region of interest.

If the path from J to I along the fractional-flow curve does not have monotonically increasing slope df_w/dS_w, a portion of the $f_w(S_w)$ curve is replaced by a discontinuity, or shock, in S_w and f_w. For gas injection in a SAG process, this means that there is a shock from a point at small f_w on the fractional-flow curve to the initial condition I. The shock proceeds with dimensionless velocity equal to the slope $\Delta f_w/\Delta S_w$ of the shock. Ahead of the shock is the uniform initial condition. Behind it is a "spreading wave" of progressively drier conditions and decreasing df_w/dS_w back to the condition J (irreducible water saturation) at the well.

From the path and slopes on the $f_w(S_w)$ diagram, one can construct a plot of the advance of the displacement in time on a diagram with axes of dimensionless position and dimensionless time. In this diagram, "characteristics," lines of constant water saturation, advance with fixed dimensionless velocity. From the total mobility corresponding to the water saturation along each characteristic, one can tell whether the shock would suffer viscous instability (greater mobility upstream of the shock than downstream). From this one can also compute injectivity as a function of time during gas injection. Figure 4.2 shows the time-distance diagram for the flood represented in Figure 4.1. Each diagonal "characteristic" line represents a fixed value of S_w, and its slope dx_D/dt_D is also the value of df_w/dS_w at the given value of S_w. The total relative mobilities (defined by Eq. (4.3) below) shown in **Figure** (4.2) are those for the values of S_w along the given characteristics. To estimate injectivity, one converts from x_D to radial position r using Eq. (4.2) and then integrates pressure outward from the well using Darcy's law and the total relative mobility at each value of r. See Leeftink et al. (2015) for examples.

A similar construction using the fractional-flow curve governs the displacement upon injection of a slug of supercritical CO_2 with surfactant dissolved
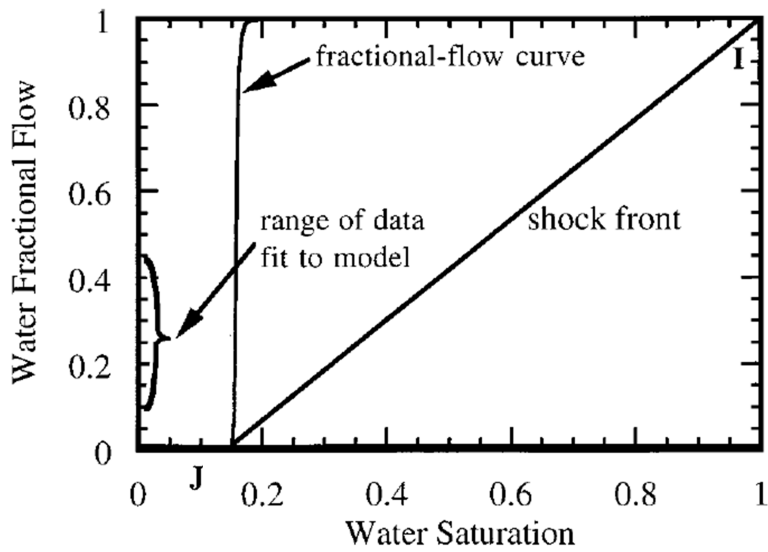
Figure 4.1: Fractional-flow function fit to model derived by Fisher et al. (1990) based on data of Lee and Heller (1990) for f_w between 0.1 and 0.44. Though not evident in this plot, the $f_w(S_w)$ function is curved at very low f_w, and there is a point of tangency at $f_w = 0.005$. From Rossen et al. (1999).
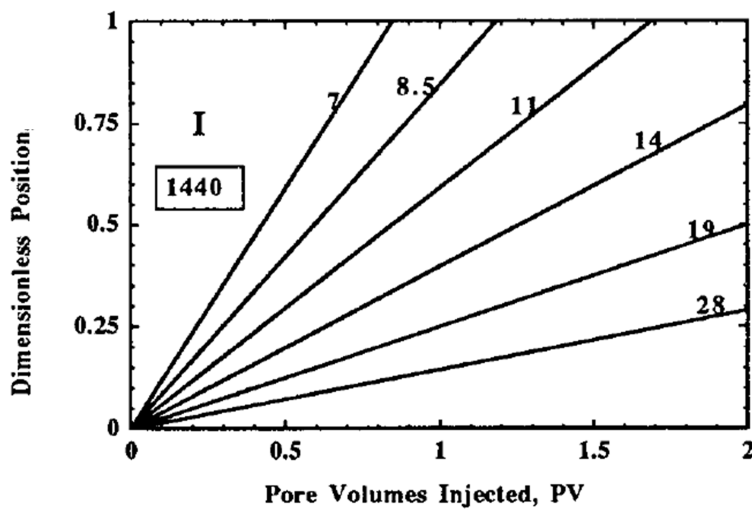
Figure 4.2: Dimensionless time-distance diagram for gas injection in SAG displacement based on Figure 4.1. Numbers are total relative mobility λ_{rt} in (Pa s)$^{-1}$; the boxed value is the uniform value of λ_{rt} for the initial state of the reservoir. From Rossen et al. (1999)

in the CO_2 (3rd method of injection listed above). Foam exists behind a shock constructed from a point of tangency at low water fractional flow; see Ashoori et al. (2010) for details.

In the example in Figure 4.1, data for foam with injected water fraction from 0.1 to 0.44 (Lee and Heller (1990) were used to fit a foam model (Fisher et al. (1990)), and then that model was used to simulate the period of gas injection in a SAG process. The shock is to a point with water fractional flow f_w = 0.005, about 20 times less than the lowest-f_w datum measured; the entire displacement takes place at f_w values less than this, well outside the range of the data on which the model was based (Rossen et al. (1999)). Reliable model-fitting for SAG processes requires steady-state data extending to f_w low enough to resolve the point of tangency illustrated in Figure 4.1.

It may seem simplest to derive parameters for modeling a SAG foam process by conducting a dynamic SAG coreflood and fitting the parameters to data of pressure gradient v. time from that experiment. Foam dynamics can distort behavior in the laboratory on a time scale of a few hours and a length scale of 10s cm, however (Persoff et al. (1991)). An LE model fit to laboratory results distorted by time-dependent dynamic processes would give an inaccurate fit. Moreover, laboratory-scale corefloods can be distorted by dispersion and by the capillary end effect. Therefore, in this work we focus on fitting steady-state laboratory foam data to an LE foam model and upscaling using fractional-flow theory to reveal implications of the model fit. Eventually, of course, the model parameters would be used in 3D simulations not subject to the limitations and assumption of fractional-flow theory. We illustrate with fits to two sets of steady-state foam data. In the process, we show the challenge of finding a single model fit to foam data over the two ranges of conditions important to a SAG flood, at low and intermediate values of water fractional flow.

4.2 METHOD

We assume that either the foam-free relative-permeability functions $k_{rw}(S_w)$ and $k_{rg}(S_w)$ are known for the core sample used in the experiments, or that water saturation S_w is measured during the experiment. We assume that a set of data for steady-state pressure gradient ∇p over a range of injected water fractional flow f_w has been collected, with sufficient data to interpolate the point of tangency to the fractional-flow curve like that in Figure 4.1. We assume that either the experiment was conducted under conditions to minimize the effects of gas compression along the core (i.e., with sufficient back-pressure) or that the data have been corrected for this effect. An example of such a correction is described in Section B.3 in Appendix B. If independent measurements of S_w are not available, then S_w must be estimated from Darcy's law and the measured pressure gradient for each value of f_w.

We assume that local equilibrium applies on the field scale: that is, that dynamic approach of foam texture to its local-equilibrium value is rapid on the scale of the displacement. Therefore the fractional-flow curve governs the displacement, and in particular the point of tangency of the $f_w(S_w)$ curve to a line drawn to the initial condition at (1,1). For any point on the $f_w(S_w)$ plot one can immediately determine total relative mobility rt at that point from the location of the point and the known function $k_{rw}(S_w)$ (Ashoori and Rossen (2012)):

$$\lambda_{rt} \equiv \left(\frac{k_{rw}(S_w)}{\mu_w} + \frac{k_{rg}^f(S_w)}{\mu_g} \right) = \frac{k_{rw}(S_w)}{\mu_w f_w} \tag{4.3}$$

This means that an accurate model fit to the data on the $f_w(S_w)$ plot gives both an accurate fit to the velocity of the foam bank and the mobility of that bank. Our goal then is to give as accurate a fit to the $f_w(S_w)$ plot near and below the point of tangency to a line to the initial condition at (1,1). Fortunately, of the three foam model parameters $fmdry$, $fmmob$ and $epdry$, $fmdry$ is set by the nearly vertical trend in $f_w(S_w)$ at larger f_w. The 'limiting capillary pressure" concept prescribes this behavior (Zhou and Rossen (1995)); two examples are shown below. The two remaining parameters can be fit visually to the $f_w(S_w)$ data using a simple spreadsheet and plotting program. As one varies the two parameters one can immediately see whether the fit is improved or not. An earlier example of data fitting is in Xu and Rossen (2004); here we illustrate with fits to the data of two other published studies.

It is sometimes convenient to represent total relative mobility λ_{rt} instead in terms of "apparent viscosity" of foam μ_{app}, where the foam is represented as a single-phase fluid. In this case,

$$\mu_{app}[\text{cp}] = \frac{1000}{\lambda_{rt} \left[(\text{Pa} \cdot \text{s})^{-1} \right]} \tag{4.4}$$

EXAMPLE 1: DATA OF PERSOFF ET AL. (1991)   The study of Persoff et al. (1991) was a key step in the understanding of the effect of the limiting capillary pressure on foam properties. In that study steady-state water saturation and foam mobility were measured over a range of injected water fractions from 0.004 to 0.29 at a variety of total superficial velocities. Remarkably, no measurable change in water saturation was observed among all the data (to within experimental uncertainty of about 0.01). If S_w is the same for all measured values of f_w then the fractional-flow function is vertical throughout the data and no point of tangency can be determined. Therefore the water-saturation data are insufficient to model a SAG foam process, as pointed out by Zhou

and Rossen (1995). In addition, one cannot determine the value of STARS parameter $fmmob$, the reduction in gas mobility at maximum-strength foam (see Eq. 3.2), from these data, because it is not clear if maximum foam strength is reached in the given scan of foam quality. Zhou and Rossen (1995) estimate that $fmmob$ (R in their terminology) is at least 18,500. The value of STARS parameter $fmdry$ (the water saturation near which foam collapses, i.e. S_w^* in their terminology) they estimate to be 0.37, based on measured ∇p and a $k_{rw}(S_w)$ function fit to all the data, with and without foam. Measured values of water saturation with foam were a little lower, scattered around 0.35, but the unchanging water saturation with foam and scatter in measurements of S_w makes it difficult to fit k_{rw} directly to the foam data. Therefore for illustration we use the $k_{rw}(S_w)$ function in Appendix B, fit to the $k_{rw}(S_w)$ data presented in the paper.

In that study either water injection rate or gas injection rate was held constant as the other varied, so total superficial velocity varied among the experiments. Here we take the data for a fixed water superficial velocity of 0.185 m/d ($2.14 \cdot 10^{-6}$ m/s) and assume it also describes mobilities at fixed total superficial velocity. There is a small, systematic decreasing trend in k_{rw} as f_w decreases in the data, shown in **Figure 4.3**. Using $k_{rw}(S_w)$ fit to the data in their study (Appendix B), one computes a slight decreasing trend in S_w as f_w decreases that is within the experimental uncertainty of the direct measurements of S_w. In other words, k_{rw} and ∇p give a more sensitive measure of changing water saturation than the direct saturation measurements, which had scatter $\pm 1\%$. This trend is shown in **Figure 4.4**. There is some scatter in the data, but the point of tangency (with slope $(\Delta f_w / \Delta S_w) \approx (1 - 0.01)/(1 - .36) \approx 1.5$) should come between $S_w = 0.36$ and 0.365. Figure 4.4 shows the slope the tangent line must approximate, though the line is not drawn tangent to the trend in the data.

Our goal in the model fit is to represent the data near the point of tangency in particular, and to the extent possible the rest of the data. Furthermore, we keep the value of $fmdry$, i.e. the water saturation near which foam abruptly weakens, at the value fit to the remainder of the data, i.e. 0.37. We seek a model fit with a point of tangency near the $f_w(S_w)$ data (for an accurate fit to foam mobility - Eq. (4.3)) and the slope forced by the tangency construction to the point representing the initial condition at (1,1). The result is shown in **Figure 4.5**. Parameter $fmdry = 0.37$ is set by the data as a whole, as noted. The other model parameters, obtained from a manual fit of parameters $fmmob$ and $epdry$, are $fmmob = 25{,}000$ and $epdry = 2500$. The point of tangency lies at $S_w = 0.363$, with total relative mobility $\lambda_{rt} = 73$ (Pa $\cdot$ s)$^{-1}$, i.e. an effective viscosity of foam (Eq. (4.4)) of about 13.7 cp.
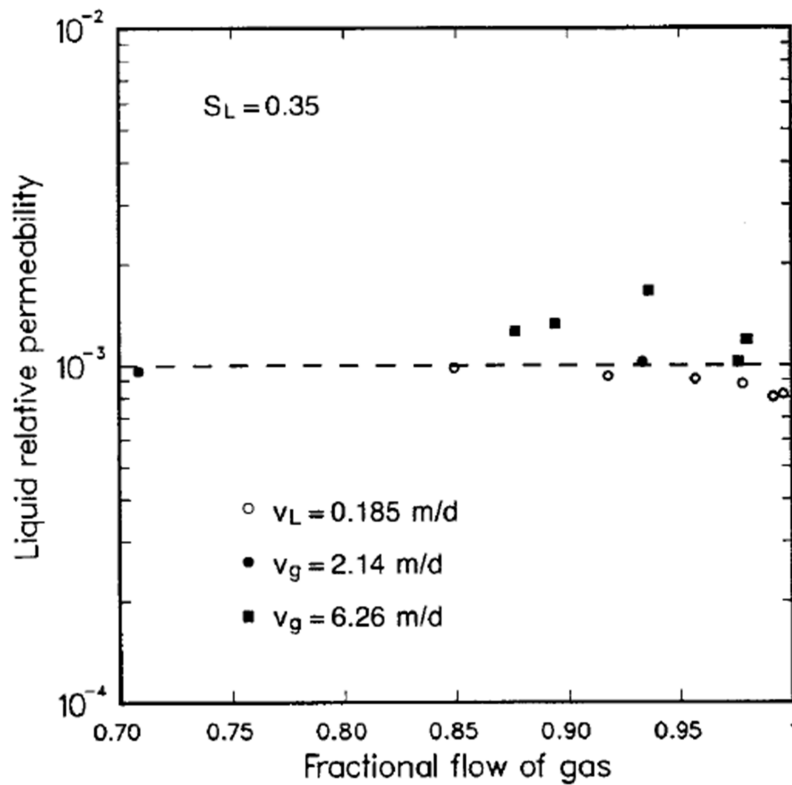
Figure 4.3: Data from Persoff et al. (1991) used in this study; we use the data represented by the open circles, for fixed water superficial velocity 0.185 m/d ($2.14 \cdot 10^{-6}$ m/s). Total superficial velocity is nearly constant for these data, varying by less than 18% from the lowest-f_w datum to the largest.

The foam front advances at a dimensionless velocity of 1.5 until this gas slug reaches the leading edge of the previously injected surfactant bank. In other words, 1 m^3 of injected gas adds about 1.5 m^3 to the foam bank.

If one increases $epdry$ so that the model fit passes lower between the two lowest-f_w data, the $f_w(S_w)$ curve shifts further away from (further below and to the right of) the data for S_w = 0.365 and 0.3665. If one then increase the value of $fmmob$, the fit to the two lowest-f_w values is poorer. **Figures 4.6a and b** illustrate the separate effects of altering $fmmob$ and $epdry$ on the fit to the data. If one adjusts $epdry$ to smaller values, for instance to make the collapse of foam near $fmdry$ less abrupt and reduce simulation time, one must also reduce $fmmob$ to maintain the fit (which also would accelerate simulation times); but the fit to the larger-f_w values is a little poorer. **Figure 4.6c** shows a fit with $fmmob = 10,000, epdry = 1000, fmdry = 0.37$.

The point of tangency is again near 0.363 and total mobility at the leading edge of the foam is again about 73 (Pa $\cdot$ s)$^{-1}$ (apparent viscosity about 13.7 cp). The fit is good to the low-f_w data, but deviates from the data at large S_w. Persoff et al. found that measured k_{rw} does not change significantly for f_w as
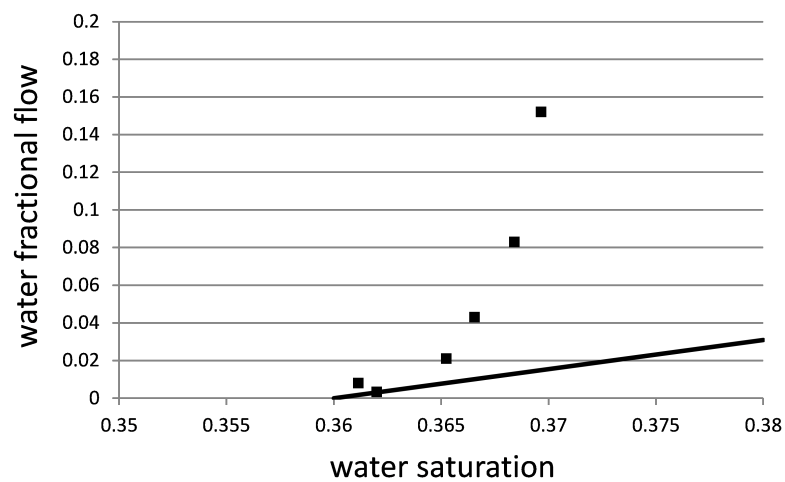
Figure 4.4: Fractional-flow data implied by the k_{rw} data of Persoff et al. (1991) (Figure 4.3) for 0.185 m/d water superficial velocity together with $k_{rw}(S_w)$ function derived from their data (Appendix B). Solid line illustrates the approximate slope ($\approx$1.5) at the point of tangency required for construction of the shock at the leading edge of the foam bank.
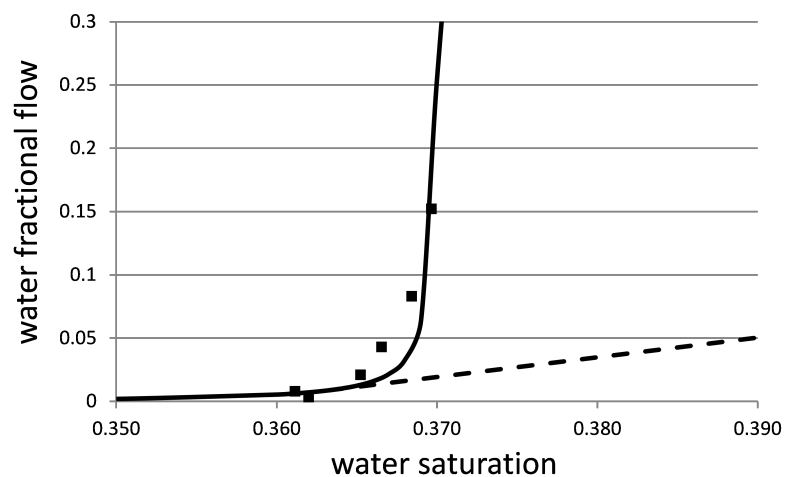
Figure 4.5: STARS model fit to data of Persoff et al. (1991): fmmob = 25,000, fmdry = 0.37, epdry = 2500.

large as 0.29; this model fit gives an increase in k_{rw} by over 40% for f_w = 0.29. That difference lies at about the limit of the scatter in the k_{rw} data in Figure 4.3.

We do not show the time-distance diagram for this model fit, because there are no data at lower f_w to compare to the model fit. Nor do we estimate injectivity with foam. However, it is important to note that in the STARS model foam does not collapse completely even at irreducible water saturation S_{wr}
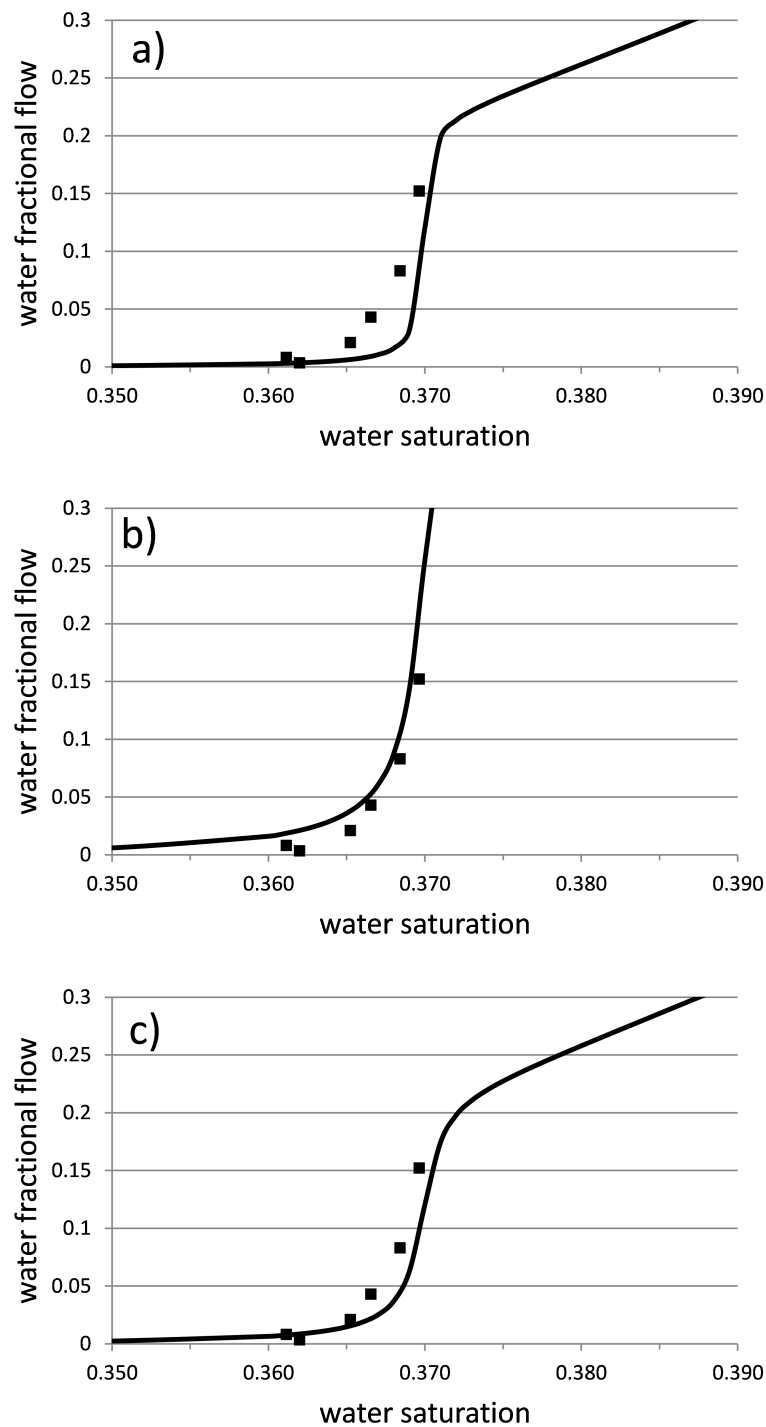
Figure 4.6: a) Same STARS model fit to data of Persoff et al. (1991) as Figure 4.5, but with $fmmob = 10,000$. b) Same STARS model fit to data of Persoff et al. (1991) as Figure 4.5, but with $epdry = 1000$. c) Same STARS model fit to data of Persoff et al. (1991) as Figure 4.5, but with $fmmob = 10,000, epdry = 1000$.

due to the functional form of the water-saturation-dependent function F_2 (Eq. (3.3)). For the model fits in both Figures 4.5 and 4.6 foam at the well has a total relative mobility of about 2400 (Pa· s)$^{-1}$, (apparent viscosity 0.42 cp), 21 times lower than the mobility of gas without foam. The failure of foam to collapse at the wellbore in the model would have a major impact on injectivity calculated with the model.

EXAMPLE 2: DATA OF MA ET AL. (2013)   Ma et al. (2013) measured foam mobility (reported in that study as apparent viscosity of foam, Eq. (4.4)) at fixed nominal superficial velocity for injected water fractions from 0.01 to 0.90. They simultaneously measured water saturation by weighing the core during the experiment. The foam-flow experiments were carried out in a 158-Darcy (1.58 $\cdot 10^{-10}$ m^2) sandpack. Ma et al. (2014) estimate $fmmob = 4.27 \cdot 10^4$, $fmdry = 0.101$, and $epdry = 500$ (using a different $k_{rw}(S_w)$ function than that in Table B.3 in Appendix B). In Chapter 3 we fit the middle range of these data using a relative-permeability function derived from another sandpack study but adjusted to fit the water saturations measured in this study. We estimate $fmmob = 3.18 \cdot 10^4$ and $fmdry = 0.130$, based on foam mobility in the middle range of f_w. The value of $fmmob$ is adjusted if one accounts for shear-thinning behavior in at high f_w, which, as noted, is not so important for a SAG process. In Chapter 3 we give no estimate of $epdry$, but suggest it should be large (in modeling a co-injection foam process). For a SAG process the value of $epdry$ is crucial, however. Ma et al. (2013) propose using a SAG coreflood to fit the value of $epdry$. Given the uncertainties in a laboratory-scale SAG coreflood noted above, we propose here instead a method based on steady-state at low water fractional flow.

One can reconstruct the fractional-flow curve directly from injected water fraction and measured water saturation in this study. The study was conducted at a single nominal total superficial velocity as injected water fractional flow varied. However, there was no back-pressure applied in these experiments, while pressure difference across the sandpack was as large as 0.5 atm. We have roughly adjusted water fractional flow for this effect by calculating the average gas superficial velocity inside the pack. This calculation is given in Appendix B. The effect is small in the low range of f_w that is the focus of this study, but alters f_w values initially near 0.5 by as much as 0.05.

Like Persoff et al., Ma et al. report nearly fixed S_w (to within measurement error) over a broad range of f_w (**Figure 4.7**). There is a clear trend to lower S_w for the two lowest values of f_w, however. A straight line between the two lowest-f_w values passes just above (1,1), which implies that the point of tan-

gency should come roughly between these two points but closer to the lower-f_w datum.

Figure 4.8 shows water relative permeability in the range of S_w relevant to foam, obtained directly from the ∇p and S_w data of Ma et al. (2013). Ma et al. do not use the experimentally measured water saturations to fit the $k_{rw}(S_w)$ function they use to fit their data. The effect of this choice is discussed in the Section "Effect of Water Relative Permeability" below. A straight line fits the four lowest- f_w data most important to a fit of gas injection in SAG. For the larger values of f_w, a very different function would be needed. In fact, these data do not appear to be consistent with the commonly used approximation that $k_{rw}(S_w)$ is a single-valued function of S_w (i.e., independent of foam properties) in foam flow. We use the linear function illustrated in Figure 4.8 (using the parameters given in Table B.3 in Appendix B) in fitting all the data.
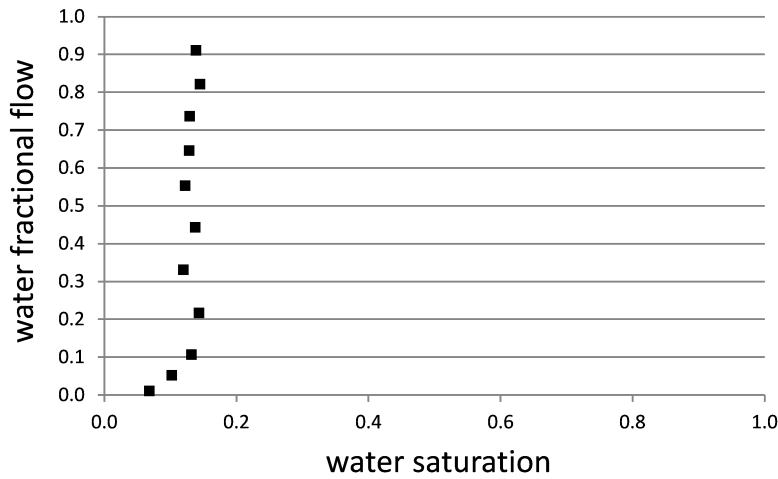
Figure 4.7: Fractional-flow data directly from data for injected f_w and measured S_w of Ma et al. (2013).

In this case the tangent line must have slope close to $[(1\text{-}0.03)/(1\text{-}0.1)] \approx 1.08$. We obtain a fit to these data with $fmmob = 12,000, fmdry = 0.13$ (in agreement with the nearly fixed S_w over the entire range of the data) and $epdry = 30$; the fit to the low-range f_w data is shown in **Figure 4.9**. The point of tangency lies near $S_w \approx 0.088$, with $\lambda_{rt} = 18$ (Pa·s)$^{-1}$, or an effective viscosity at the leading edge of the foam bank of about 56 cp. The fit is consistent with the f_w and S_w values in the low range of f_w, and therefore consistent with both the velocity and mobility of the foam shock implied by these data.

This fit is not at all consistent with the upper range of f_w data, however, as shown in **Figure 4.10**. Thus in a multi-slug process these parameters would give a poor fit to mobility in the mixing zone where slugs merge. An attempt to fit the entire range of $f_w(S_w)$ data better is illustrated in **Figures 4.11** and **4.12**,
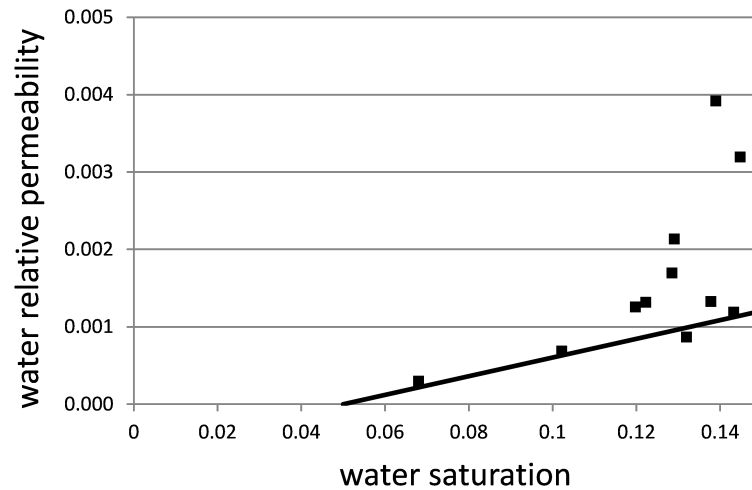
Figure 4.8: Data for $k_{rw}(S_w)$ computed from ∇p and S_w data of Ma et al. (2013). A linear function works reasonably well for the four lowest-f_w data most important to gas injection in SAG (see Table B.3 in Appendix B).

using $fmmob = 100,000$, $fmdry = 0.13$, and $epdry = 400$. The fit is better in the upper range of f_w, and the fit roughly similar to that in Figure 4.9 to the lower range: the point of tangency is at $S_w = 0.09$, with total relative mobility about 23 (Pa·s)$^{-1}$ (apparent viscosity 43 cp). However, though the $f_w(S_w)$ data are fit reasonably well in the middle range, the mobility (expressed as apparent viscosity) is poorly matched there: it peaks at 700 cp around $f_w = 0.67$ rather than about 400 cp at about $f_w = 0.5$ as in the data of Ma et al. In part this may be a result of using the linear $k_{rw}(S_w)$ function based on the low-f_w data for the data in the upper range of f_w. A better fit to the apparent viscosity data over the entire range of f_w, consistent with a fit to the low-range $f_w(S_w)$ data, is obtained with $fmmob = 40,000$, $fmdry = 0.13$, and $epdry = 150$ (Figure **4.13**). The fit to the $f_w(S_w)$ data in the upper range of f_w is worse (Figure 4.13), but the mobility behind the shock at the foam bank is again about 22 (Pa·s)$^{-1}$, i.e. with an apparent viscosity of 45 cp, similar to the fit in Figures. 4.9 and 4.11, and the fit to apparent viscosity as a function of injected gas fractional flow (**Figure 4.14**) compares well to the data of Ma et al.

As with the fit to the data of Persoff et al. here, the STARS foam model does not represent collapse even at irreducible water saturation S_{wr}. For the model fit in Figures 4.9 and 4.10, foam at the well has a total relative mobility of only 33 (Pa·s)$^{-1}$ (apparent viscosity 30 cp), 1500 times less than the mobility of gas without foam. For the fits in Figures 4.11 and 4.13 total relative mobility at the well is about 50 (Pa·s)$^{-1}$ (apparent viscosity 20 cp), 1000 times less than the mobility of gas without foam. The apparent viscosity of foam is not much less at the well than at the leading edge of the foam bank. Though the parameter
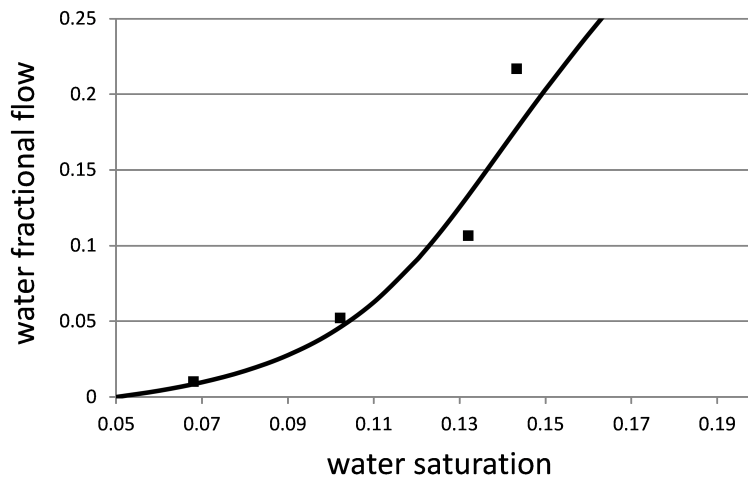
Figure 4.9: STARS model fit to data of Ma et al. (2013) in low range of f_w: fmmob = 12,000, fmdry = 0.13, epdry = 30.
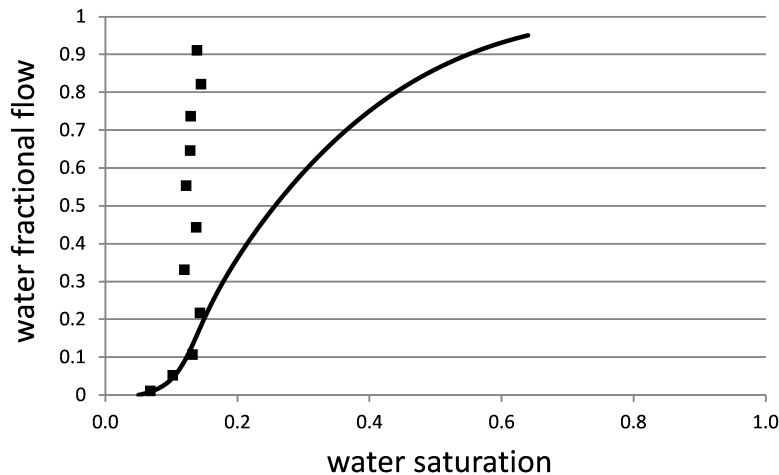
Figure 4.10: STARS model fit to low range of f_w data from Ma et al. (2013) in Figure 9 compared to entire data set.

values shown here fit the fractional-flow data reasonably well near the point of tangency, and thus represent the leading edge of the foam bank during gas injection, they grossly underestimate injectivity of gas. One can immediately put an upper bound on injectivity in the two cases: it is poorer than for a 20 or 30 cp Newtonian fluid in single-phase flow. Injectivity in a SAG process is expected to be much greater (Shan and Rossen (2004); Leeftink et al. (2015)).

EFFECT OF WATER RELATIVE-PERMEABILITY FUNCTION   In the absence of measured water saturations in this experiment, one would have to use relative-permeability functions for similar media, i.e. sandpacks. An example are the
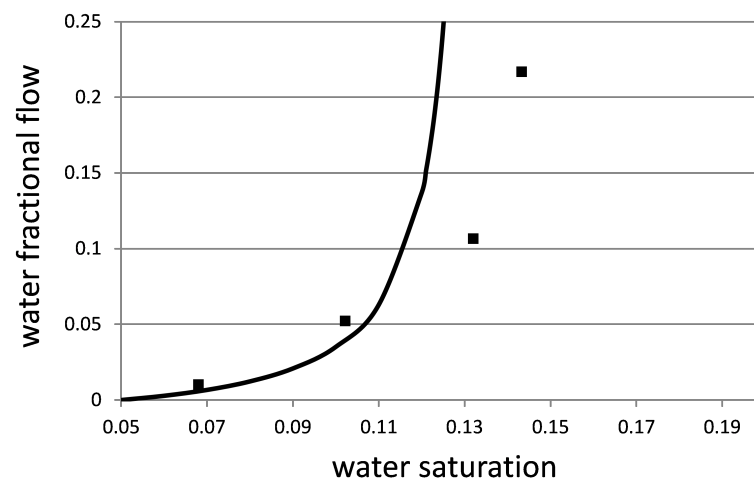
Figure 4.11: STARS model fit to data of Ma et al. (2013) in the low range of f_w: fmmob = 100,000, fmdry = 0.13, epdry = 400; focus on lower range of f_w.
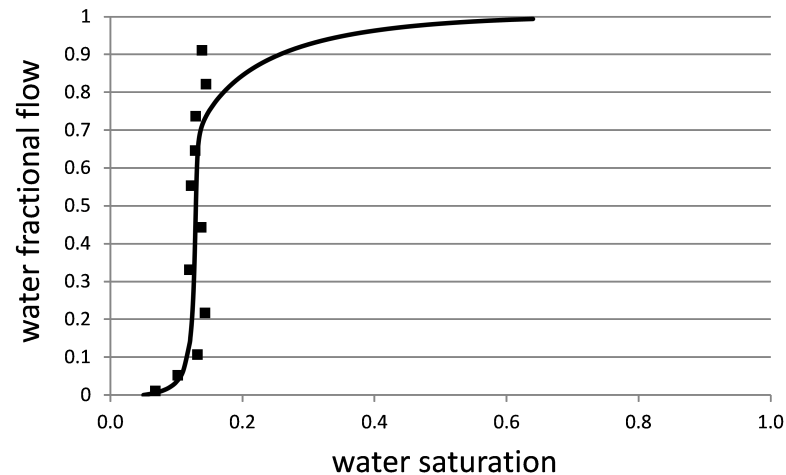
Figure 4.12: STARS model fit from Ma et al. (2013) in Figure 11 compared to entire data set.

functions of Kam and Rossen (2003), given in Appendix A. In this case, in the absence of measured values, water saturation would be inferred from measured mobility or apparent viscosity and the water relative-permeability function (Eqs. (4.3) and (4.4)). The result of this calculation is shown in **Figures 4.15 and 4.16**. The scatter in water saturation in the vertical portion of the $f_w(S_w)$ curve (which now occurs near $S_w = 0.08$) largely disappears and the decrease in S_w in the lowest-f_w data is smaller. As a result, in this case a straight line drawn through the two lowest-f_w data would pass far above (1,1), which suggests that the point of tangency at a value of S_w and f_w below the range of the data.
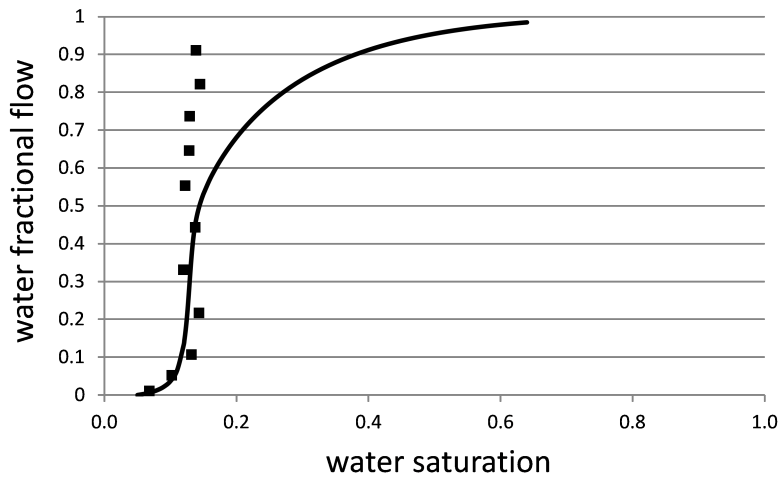
Figure 4.13: STARS model fit to data of Ma et al. (2013) over entire range of f_w adjusted to fit mobility data in middle range of data: fmmob = 40,000, fmdry = 0.13, epdry = 150.
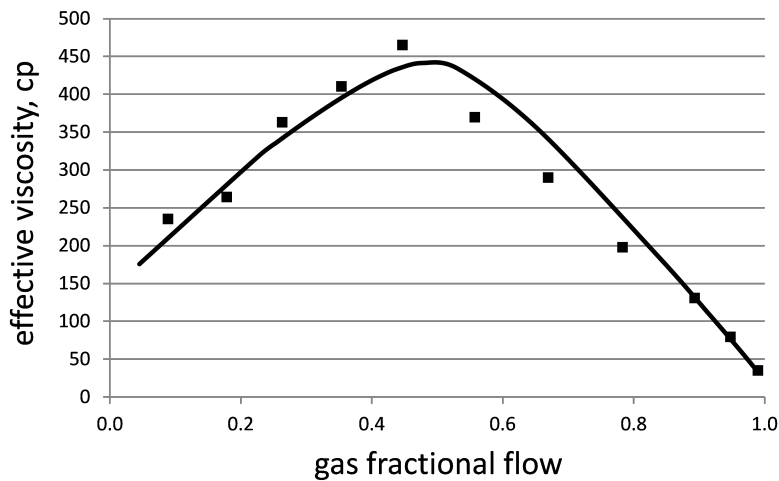
Figure 4.14: Fit of model parameters from Figure 4.13 to apparent viscosity data of Ma et al. (2013).

Figures 4.15 and 4.16 also show the fit using $fmmob$ equal to 55,000, $fmdry$ 0.08, and $epdry$ 800. The point of tangency is at S_w = 0.063 and f_w = 0.005, below range of the measured data. The leading edge of the foam bank has total relative mobility about 38 (Pa·s)$^{-1}$ (apparent viscosity about 26 cp). This is about half the apparent viscosity of the fits using the directly measured S_w values. The dimensionless velocity of the foam bank decreases slightly, from 1.08 in the previous fits to 1.05, reflecting the shift to smaller values of S_w. Using the set of S_w values inferred from mobilities rather than measured directly makes a substantial difference to the predicted mobility of foam in a SAG flood.
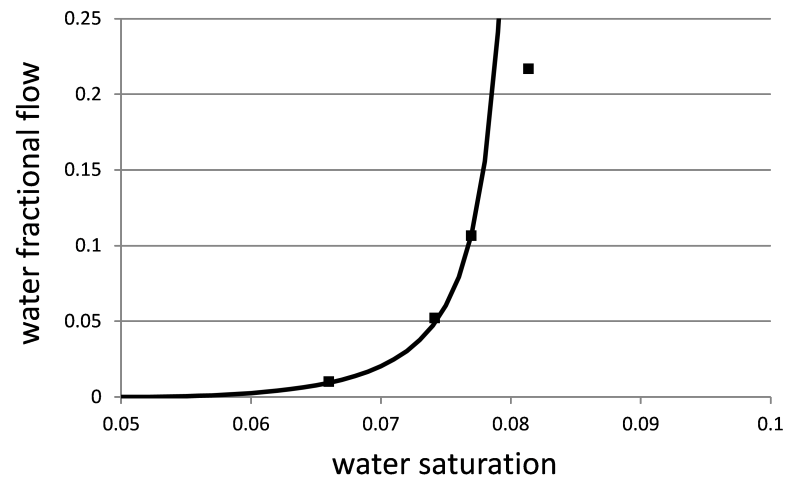
Figure 4.15: STARS model fit to data of Ma et al. (2013) using S_w values estimated from measured mobility relative-permeability functions from Kam and Rossen (2003); focus on low range of f_w: fmmob = 55,000, fmdry = 0.08, epdry = 800.
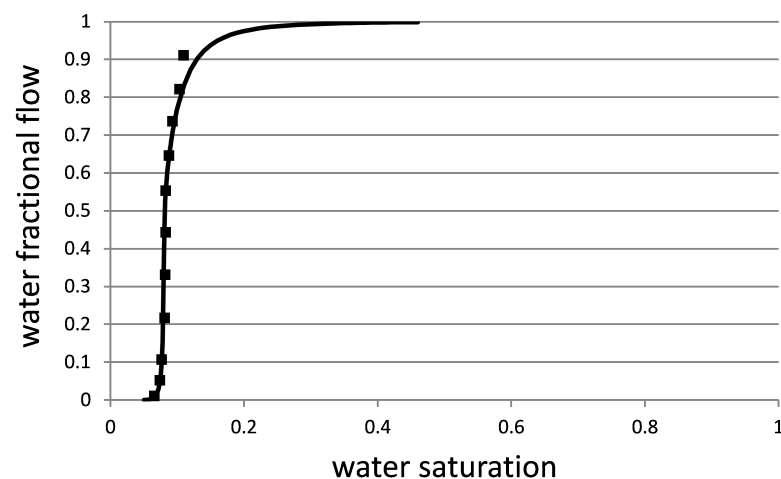
Figure 4.16: STARS model fit to low range of f_w data from Ma et al. (2013) in Figure 14 compared to entire data set.

For the model fit in Figures 4.15 and 4.16, foam at the well has a total relative mobility of 68 (Pa·s)$^{-1}$ (apparent viscosity 14.6 cp), 730 times less than the mobility of gas without foam.

Ma et al. (2013) propose a different method for fitting data: using data from a dynamic SAG coreflood to choose among parameter sets fit to the data in Figure 4.14. They use the $k_{rw}(S_w)$ function given in the last column of **Table B.3**. **Figure 4.17** compares the fractional-flow curve based on their parameter fit to the $f_w(S_w)$ data using the measured values of S_w and those inferred from

∇p and the $k_{rw}(S_w)$ function used in the model fit. The fractional-flow curve based on the parameter fit is reasonably consistent with the $f_w(S_w)$ data based on the calculated S_w data, but not with the measured S_w data. The mobility at the leading edge of the foam bank in their model fit is 31 $(Pa \cdot s)^{-1}$, compared to 18-22 $(Pa \cdot s)^{-1}$ in our model fit using their S_w data directly and 38 $(Pa \cdot s)^{-1}$ in our model fit using a relative-permeability function similar to theirs. The mobility at S_{wr} is 51 $(Pa \cdot s)^{-1}$.
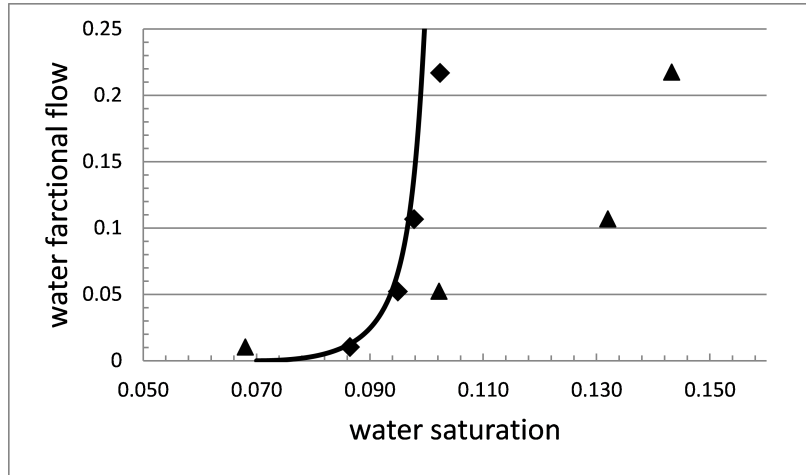
Figure 4.17: Comparison of the fractional-flow curve based on parameter fit by Ma et al. (2013) to their data (curve) and $f_w(S_w)$ data based on measured S_w values (triangles) and based on S_w values inferred from ∇p and assumed $k_{rw}(S_w)$ function (diamonds). ∇ parameter values $fmmob = 47,100, fmdry = 0.1006$, and $epdry = 500$.

4.3   SUMMARY AND DISCUSSION

Others have shown that the fractional-flow curve is the key to predicting the performance of a SAG foam process during gas injection (e.g., Shan and Rossen (2004)). Here we show how to use the fractional-flow plot to fit foam model parameters to steady-state foam coreflood data and thereby predict the SAG displacement that is implied by these data. For reasons discussed in the text we believe steady-state data to be more reliable for model fitting than a single dynamic SAG coreflood. For illustration we use the STARS local-equilibrium foam model here, but the same approach could be used with other foam models. During the period of gas injection, the success of a SAG foam process hinges on the properties of foam at the point of tangency that defines the leading edge of the gas bank. Correctly fitting the $f_w(S_w)$ data from the corefloods implies a correct fit both to the velocity and the mobility of the foam bank (Eq. (4.3)).

In the cases shown, there is a nearly vertical trend over much of the $f_w(S_w)$ data that sets the value of *fmdry*, the water saturation around which foam collapses. This leaves two parameters to fit, *epdry* and *fmmob*. Increasing *epdry* reduces predicted $f_w(S_w)$ for the lowest-f_w data, while increasing *fmmob* increases $f_w(S_w)$ in this range. At the upper range of f_w, increasing *epdry* and *fmmob* both increase the predicted value of $f_w(S_w)$.

A simple spreadsheet can instantly show the fit to $f_w(S_w)$ data for any parameter set. Thus, it is easy to judge the best value of *fmmob* for a given value of *epdry*, for instance, as illustrated in Figure 4.6, and then vary *epdry* in the search for the best fit to all the data. Our results in Figures 4.9 through 4.14 illustrate this process.

One could use least-squares optimization to search for optimal parameter values, but such an optimization must still begin with the user's judgment on the relative importance of fitting low-f_w data v. the entire data set, and of fitting mobilities v. measured water saturations. Here we illustrate how these judgments can lead to different parameter choices.

Accurate measurements of water saturation in the experiment, or, failing that, a reliable water relative-permeability function $k_{rw}(S_w)$, is key to upscaling the data to a SAG flood, as noted previously by Ashoori and Rossen (2012). For the data of Ma et al. (2013), using S_w values inferred from measured mobilities and a plausible $k_{rw}(S_w)$ function instead of the directly measured S_w values results in a factor of two difference in mobility at the leading edge of the foam bank.

A SAG process involving multiple slugs depends not only on foam behavior at low water fractional flow but, further from the well, on behavior at larger water fractional flow. The examples presented here indicate the challenge in obtaining a fit to both ranges of data. Compromises must be made between fitting all the saturation, mobility, and fractional-flow data. It may be that a new functional form is needed for the effect of capillary pressure and water saturation on foam that could better fit the whole range of data.

We do not compute gas injectivity in the cases shown because nearly the entire foam bank (the spreading wave from the shock back to the injection condition J in Figures 4.1 and 4.2) is predicted to lie beyond the range of the data - that is, starting with the shock near the lowest-f_w value and decreasing in f_w from there. The fact that in the STARS dry-out model (Eqs. (4.1)) foam does not collapse even at S_{wr} does have an important effect on predicted injectivity, however. For the fit to the Persoff et al. (1991) data, mobility at the well is about 20 times less than that expected if foam collapses at S_{wc}, and for the fits to the data of Ma et al. (2013) mobility at the well is between 1000 and 1500 times

less than expected. Injectivity calculated with the model would be exceedingly poor.

Liquid injectivity is also a major challenge to a multi-slug SAG process. Several published studies (Zerhboub et al. (1991); Persoff et al. (1990); Kibodeaux et al. (1994); Zeilinger et al. (1995); Robert and Mack (1997); Cheng et al. (2000); Nguyen et al. (2009)) examine liquid injectivity following co-injection of gas and liquid rather than following gas injection in a SAG process; mostly these studies were focused on foam-acid diversion in well-stimulation treatments. In such studies liquid injectivity is exceedingly poor (which is the goal of foam-acid diversion). In a separate study from the one examined here, Persoff et al. (1990) examined liquid injection following foam injection, and found no measurable increase in liquid relatively permeability during subsequent injection of surfactant solution: k_{rw} remained at 0.001 during liquid injection. Other studies report modest increases in k_{rw} during injection of surfactant solution following foam. In one field test of SAG, poor liquid injectivity led to fracturing of the injection well and loss of subsequent surfactant slugs (Martinsen and Vassenden (1999)).

One advantage of the method presented here, of fitting $f_w(S_w)$ data directly for SAG processes, is that it immediately shows if the form of the model itself is inappropriate for SAG. Some functional forms suggested in the literature for the effect of capillary pressure (or water saturation) on foam are incapable of representing a SAG process because they predict a point of tangency to the $f_w(S_w)$ function at complete foam collapse. Rossen et al. (1999) and Dong and Rossen (2007) show examples. This sort of problem would be immediately apparent in plotting the model-generated $f_w(S_w)$ function for comparison with the data.

MODELING FOAM FLOW IN RADIAL SAG INJECTION

5.1 INTRODUCTION

Gas injection for enhanced oil recovery can be efficient at mobilizing oil where gas sweeps, but suffers from poor sweep efficiency because of reservoir heterogeneity, viscous instability and gravity segregation of injected gas to the top of the formation (Lake (1989)). Foam can address all three sources of poor sweep of gas (Schramm (1994); Rossen (1996)). In cases of gravity override in relatively homogeneous formations, the best foam-injection strategy is injecting a large slug of surfactant solution followed by a large slug of gas (Shan and Rossen (2004)), maintaining the maximum allowed injection pressure (just below fracturing pressure) at all times. The injection rate of gas should be adjusted to maintain this injection pressure. This advantage obtains from the good injectivity of a gas slug during a SAG foam process, even while maintaining mobility control with the fluids ahead of foam. In the North Sea field example described by de Velde Harsenhorst et al. (2014) the effect of gravity on this process over a distance of even 6 km is small. Moreover, Grassia et al. (2014) show that in such a process in principle the foam bank can propagate indefinitely without suffering worsening gravity override. In multiple-slug processes the extremely poor injectivity of surfactant slugs reduces this advantage substantially. Faisal et al. (2009), and Kloet et al. (2009) find a single-slug process (i.e. a process that consists of injecting one large surfactant slug followed by one large gas slug rather than multiple, smaller cycles) superior to multiple-slug processes in spite of challenges to placement of the initial surfactant slug with no diversion yet in place.

Availability of gas is a major issue if the gas is produced from an industrial plant with limited capacity or a gas field with limited production rate; one may

---

not be able to adjust injection rate at will. As mentioned by Melzer (2012), limited supply of CO_2 is presently constricting the growth of CO_2-based EOR processes. Here we present a simple model for the injection rate required to maintain a constant injection pressure in a SAG foam process during the period of radial flow. It builds upon fractional-flow theory for foam SAG processes, and in particular on the finding that soon after gas injection begins the pressure difference across the foam bank a single-slug SAG process approaches a constant value. This suggests asymptotic formulas for required injection rate in two limiting cases, one of a foam just strong enough to maintain mobility control at its leading edge, and the other an extremely strong foam. The formula is based on the assumption of radial flow; we therefore compare the theoretical result to flow in a five-spot pattern to check the duration of the period during which the model predictions are valid.

5.2 THEORY

Fractional-flow theory, or the Method of Characteristics (MOC), for gas injection in a SAG foam process is described in detail elsewhere (Zhou and Rossen (1995); Shan and Rossen (2004)). There are a number of simplifying assumptions, including incompressible phases, Newtonian mobilities, immediate attainment of local steady-state, and, in this study, a homogeneous cylindrical reservoir and only two mobile phases (water and gas) in the foam bank; oil may be present at a uniform residual saturation within this bank. MOC analysis of three-phase foam flow with mobile oil is possible but much more complex (Mayberry et al. (2008); Namdar Zanganeh et al. (2011)).

In a single-slug SAG foam process, during injection of gas there is a shock from the initial condition of zero gas saturation to a point of very-low fractional flow of water f_w, representing the leading edge of the foam bank. Behind this front are "characteristics," each representing a fixed water saturation S_w, becoming progressively drier until, at the well, $f_w = 0$ and $S_w = S_{wr}$, i.e. irreducible water saturation. Ahead of the shock, we assume, the formation is at a uniform state at the initial condition I. The shock and all the characteristics behind the shock travel with constant dimensionless velocity dx_D/dt_D, where dimensionless position and time are defined by

$$x_D \equiv \frac{r^2 - r_w^2}{r_e^2 - r_w^2} \qquad t_D \equiv \frac{Qt}{\pi r_e^2 H \varphi} \tag{5.1}$$

and dimensionless velocity is

$$\frac{\mathrm{d}x_D}{\mathrm{d}t_D} = \frac{\mathrm{d}f_w}{\mathrm{d}S_w} \tag{5.2}$$

for each characteristic with a given value of S_w. Here r, r_w and r_e are radial position, wellbore radius and the outer radius of the cylindrical reservoir, Q is volumetric injection rate, H the thickness of the formation, φ formation porosity and f_w water fractional flow, a function of water saturation S_w. Crucial to what follows is that if characteristics with low mobility have passed far enough from the well that the r_w^2 term in Eq. (5.1) is insignificant, then the pressure difference across the foam bank is nearly constant in time as the foam bank propagates radially outward. Another requirement is that mobility near the wellbore be very large compared to mobility further from the well; a SAG process in which foam collapses completely at S_{wr} near the well satisfies this requirement, but a process of continuous foam injection would not. This result is demonstrated in Appendix C.

Let the constant pressure difference across the foam bank at fixed injection rate Q be ΔP_f, and let the foam injectivity $I_f \equiv Q/\Delta P_f$. Since the uniform initial condition ahead of the foam bank is at zero gas saturation, the total rise in injection-well pressure at a time when the leading edge of the foam bank is at radial position r_f is given by

$$
\begin{aligned}
p(r_w) - p(r_e) &= \frac{Q}{I_f} + \frac{Q}{2\pi H k \lambda_{rt}^I} \ln\left(\frac{r_e}{r_f}\right) \\
&= Q\left[I_f^{-1} + \frac{\ln(r_e/r_f)}{2\pi H k \lambda_{rt}^I}\right]
\end{aligned}
\tag{5.3}
$$

where λ_{rt}^I is the total relative mobility at the initial condition. The first term in square brackets reflects the constant pressure difference across the foam bank, and the second term the pressure difference ahead of the foam bank. Equation (5.3) implies that the total injection pressure is the sum of a constant term, proportional to injection rate Q, and a second term, which decreases with time as $\ln(r_e/r_f)$. If the injection pressure is fixed, then injection rate is given by

$$Q = [p(r_w) - p(r_e)]\left[I_f^{-1} + \frac{\ln(r_e/r_f)}{2\pi H k \lambda_{rt}^I}\right]^{-1} \tag{5.4}$$

Appendix C shows that foam injectivity I_f is given by

$$I_f = \left[\int_{r_w}^{r_f} \frac{1}{2\pi Hk\lambda_{rt}(r)} \mathrm{d}\ln r \right]^{-1} \tag{5.5}$$

which is approximately constant for $r_w \ll r_f \leq r_e$. We make Q dimensionless in Eq. (5.4) by dividing the injection rate by that with the same pressure difference at the initial state of the reservoir, which has uniform relative mobility λ_{rt}^I:

$$Q_D = \frac{\frac{\ln(r_e/r_w)}{2\pi Hk\lambda_{rt}^I}}{\left[I_f^{-1} + \frac{\ln(r_e/r_f)}{2\pi Hk\lambda_{rt}^I} \right]} = \left(I_{fD}^{-1} + \frac{\ln(r_e/r_f)}{\ln(r_e/r_w)} \right)^{-1} \tag{5.6}$$

where

$$I_{fD} \equiv \frac{\ln(r_e/r_w)}{2\pi Hk\lambda_{rt}^I} I_f \tag{5.7}$$

In other words, the injection rate required to keep injection pressure constant is inversely proportional to the sum of a constant (reflecting the foam bank) and a term that decreases with time (reflecting the shrinking region ahead of the foam bank).

5.3 RESULTS

There are two limiting cases for Eq. 5.6. If $I_{fD} \ll 1$ (an extremely strong foam), the required injection rate is nearly constant with time, as might be desirable if gas is obtained from a steady, continuous industrial process. Injection rate is also comparatively small, and thus the time to produce the reservoir would be long unless the well spacing were close. The other limiting case is $I_{fD} \gg 1$, i.e. foam injectivity is much greater than that of water before foam. This case is limited by the requirement that foam maintain mobility control at its leading edge; otherwise the foam does not accomplish its primary objective. It is possible to maintain mobility control at the leading edge of the foam bank and still have good injectivity (i.e., approach the second limiting case); this is a principal advantage of SAG foam processes. Appendix C shows an example where mobility at the leading edge of the foam bank is 0.68 of that ahead of it, but $I_{fD} = 4.5$.

Figures 5.1a and **b** illustrate the implications for optimal injection rate for two cases: $I_{fD} = 0.40$ (similar to the case of the parameters fitted to the data of Persoff et al. (1990), described in Appendix B), and 4.5, the "weak foam" case

where foam is just able to maintain mobility control relative to fluids ahead of it. The data of Persoff et al. (Table B.4) represents a relatively strong foam, meaning very low mobility within the foam bank. This is illustrated in **Figures 5.2a** and **b**, which show characteristics of constant mobility in t_D-x_D diagrams for the two cases. At all locations, the effective viscosity in the "weak foam" model is roughly ten times less than that in the Persoff model. Nonetheless, the "weak foam" model also maintains mobility control at its leading edge. The model of a constant I_{fD} is not valid for extremely short times (cf. **Figures C.1** and **C.2**), during which I_{fD} approaches its steady value. Those figures show that injectivity does go through a minimum shortly after gas injection begins, however. For the foam parameters corresponding to the data of Persoff et al. (1990) ($I_{fD} = 0.40$), the injection rate required to maintain fixed injection pressure is nearly constant after a time of low injectivity at startup. This would suit a continuous, fixed supply of gas, e.g. from a separation plant downstream of an industrial process. However, the injection rate would be less than that for water injection before gas injection, and the time to finish the EOR process is thus lengthened. For the foam just able to maintain mobility control, Figure 5.1b, the injection rate required to hold injection pressure constant increases with time, more than quadrupling as the leading edge of the foam bank reaches the outer edge of the cylindrical region assumed here. If gas were available on demand at any volumetric rate, then this process has the advantage of faster injection and faster completion of the EOR process.

| (a) | (b) |
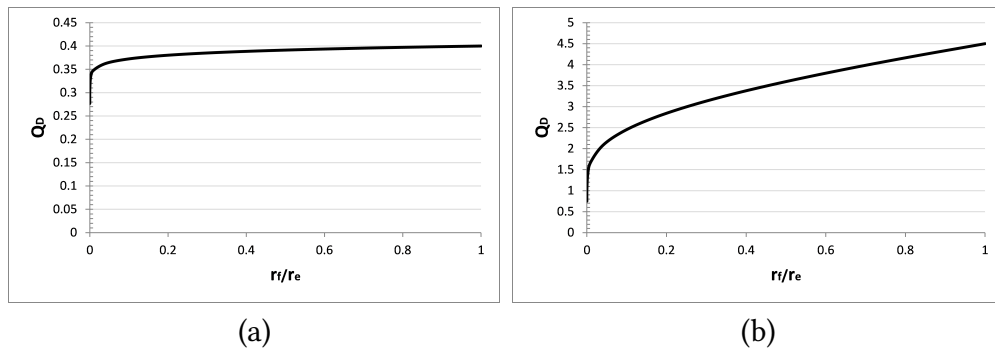
Figure 5.1: Dimensionless gas injection rate required to maintain constant injection pressure for (a) $I_{fD} = 0.40$ and (b) $I_{fD} = 4.5$ respectively.

Our approach suggests two design strategies for foam formulation. If the gas supply is flexible and able to meet increasing demand over time, then a process designed to maintain mobility control at its leading edge, while maximizing injectivity, would be best. This process maximizes injection rate and accelerates completion of the process. If gas is supplied at a fixed rate Q, then one might design a strong foam that would maintain relatively slow injection at fixed rate.

(a)   (b)
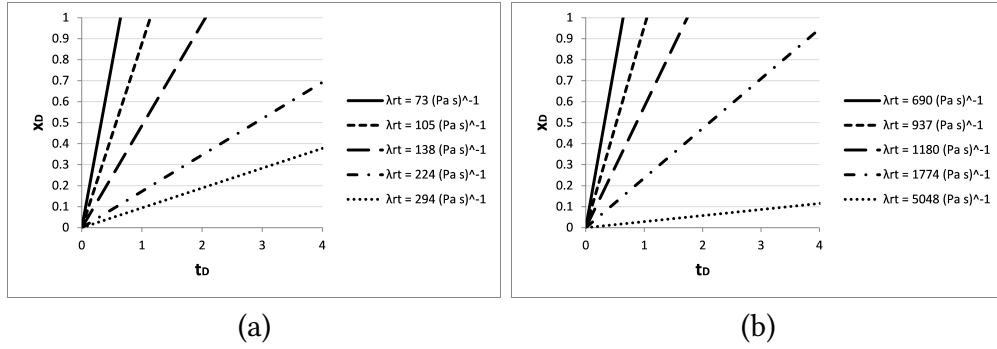
Figure 5.2: Time (t_D)-distance (x_D) diagrams from the fractional-flow solution for gas injection in a SAG process: (a) for model fit of Rossen and Boeije ((SPE 165282) to data of Persoff et al. (1990), (b) for gas injection in a SAG process for "weak-foam" model that still maintains mobility control at the front of the gas bank. See Table B.4 for parameter values.

If the pressure difference across the foam bank dominates injectivity, then the second term in the denominator of Eq. (5.4) is insignificant, and

$$I_f^{-1} = \frac{p(r_w) - p(r_e)}{Q} \tag{5.8}$$

In principle, Eq. (C.4) could be used to evaluate the injectivity of foam processes based only on the fractional-flow curve derived from the model fit to data (cf. Chapter 4). The problem is that this integral (Eq. (C.4)) diverges for $\eta \to 0$. We find that for the model fit to the data of Persoff et al. (1990) and the "weak foam" model (second and fifth columns of Table B.4) that a good fit is obtained using

$$p(r_w) - p(r_f) = \int_\varepsilon^{\eta_{shock}} \frac{Q}{4\pi H k \lambda_{rt}(S_w(\eta))} d\ln \eta \tag{5.9}$$

where ε is about $2 \cdot 10^{-6}$. This suggests that if a particular value of I_{fD} is desired, based for instance on the available gas supply, one should seek a foam formulation for which

$$I_{fD} = \frac{\ln(r_e/r_w)}{\lambda_{rt}^I} \left[\frac{1}{2} \int_\varepsilon^{\eta_{shock}} \frac{d\ln \eta}{\lambda_{rt}(S_w(\eta))} \right]^{-1} \tag{5.10}$$

The term in brackets depends only on phase mobilities and water fractional flow as functions of water saturation, and not on the geometry of a given well pattern; it could be calculated directly from laboratory foam-mobility data for a given foam formulation and geological formation.

5.4   COMPARISON TO INJECTIVITY IN FIVE-SPOT PATTERN

The modeling above is based on radial flow, which raises the question of relevance to a pattern flood. We therefore carried out simulations in a five-spot pattern using the reservoir simulator STARS from the Computer Modeling Group (2006). For symmetry reasons only one quarter of the pattern was modeled. In these simulations, gas (nitrogen) is injected into one (the bottom-left) corner of a square reservoir that is initially filled with surfactant solution. The production well is located in the opposite (top-right) corner. Effects of gravity are not considered in these 2D simulations. Grassia et al. (2014) and de Velde Harsenhorst et al. (2014) find that in a single-cycle SAG process a foam front can propagate indefinitely with little gravity override; thus we consider 2D areal simulations sufficient for comparison. The square geometry is built-up of 100x100 grid blocks and the well-to-well distance is 100 meters. Two sets of simulations were performed, to reflect the two cases in Figures 5.1a and b: one using the parameter values we fit to the data of Persoff et al. (1990) ("strong foam") and one with parameter values for the "weak foam". The parameter values are given in Table B.4.

Initial reservoir conditions and operating constraints are the same for both simulations. The initial reservoir pressure is set to 100 bar. Nitrogen is injected with a fixed pressure of 150 bar and the producing well is operated at a constant pressure of 100 bar.

5.4.1   *Radial-Flow Approximation*

One of the advantages of foam is that viscous fingering is reduced, thus increasing the period of approximate radial flow and delaying the time of gas breakthrough. The period of radial flow is a function of the mobility of the foam bank. **Figures 5.3** and **5.4** show gas-saturation profiles for both the strong- and weak-foam simulations. Results are plotted for various values of the fraction of the reservoir volume that is swept by gas. Circular arcs are plotted in the same figures to emphasize the difference between the simulations and perfectly radial flow.

(a) Swept fraction = 0.179

(b) Swept fraction = 0.583

(c) Swept fraction = 0.751
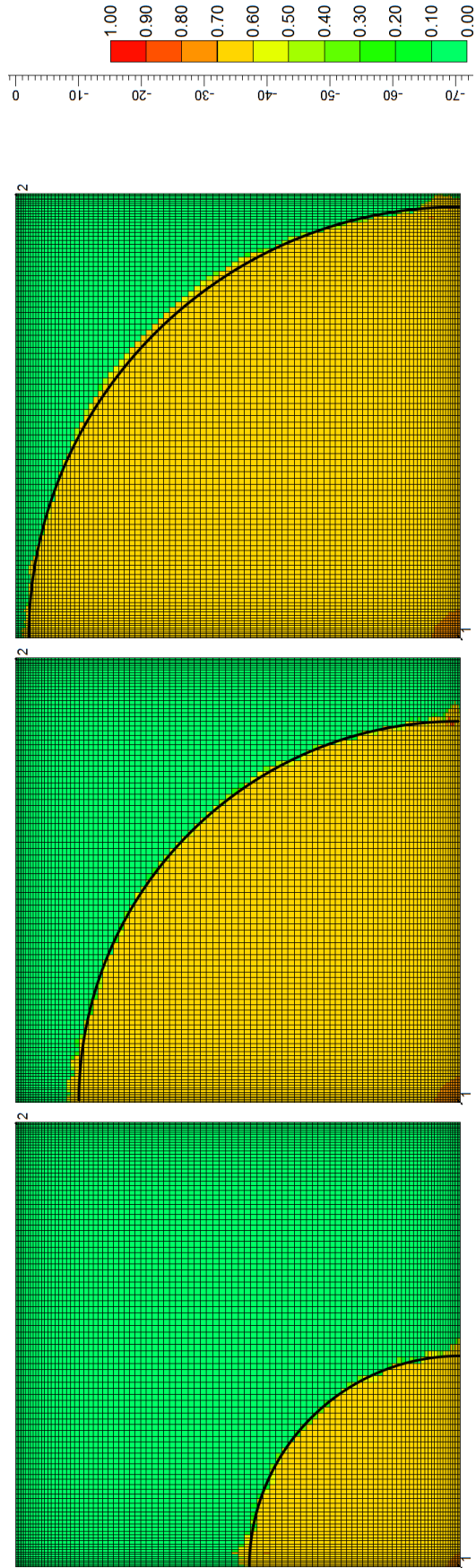
Figure 5.3: Gas saturation profiles for three different values of the swept fraction (strong-foam simulation).

(a) Swept fraction = 0.171

(b) Swept fraction = 0.462

(c) Swept fraction = 0.775
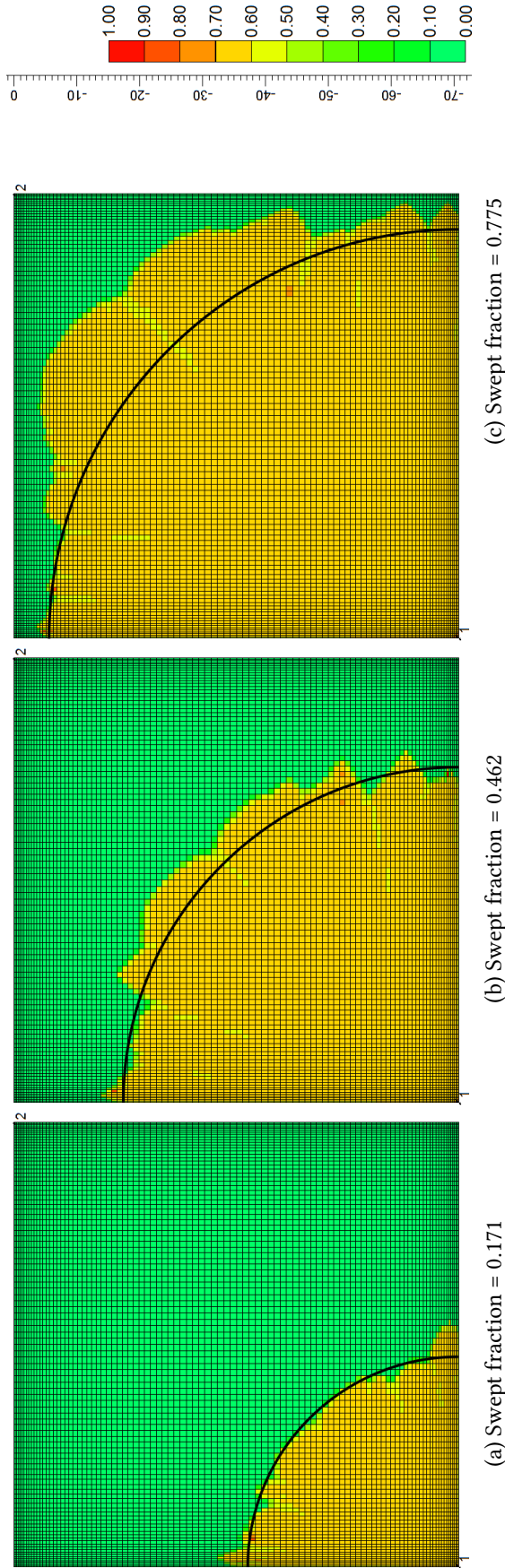
Figure 5.4: Gas saturation profiles for three different values of the swept fraction (weak-foam simulation).

Small deviations from the radial flow profile start only after about 75% of the reservoir has been swept for the strong-foam simulation, indicating good mobility control. For the weak foam, the deviations start much sooner. Modest deviations can already be observed after only 17% of the reservoir has been swept.

The gas saturation in the foam bank is fairly constant at a value of $S_g \approx 1 - fmdry = 0.63$ except close to the injection well where the gas saturation increases, indicating foam dry-out. Thus the injected gas pore volumes, at reservoir conditions, are approximately 0.63 times the swept fraction given above.

5.4.2   *Injection Rates*

For comparison with the analytical calculations we determined the gas injection rates in the simulations. We show these here as a function of the fraction of the reservoir that is swept. We determine the volume of gas in place based on the volume of water produced and an approximate gas saturation of 0.63 throughout the foam bank. We chose the swept fraction rather than the PV gas injected, because there is a large pressure drop (50 bar) over the reservoir, meaning gas compressibility is a significant issue leading to some ambiguity in the term "reservoir PV injected". Injection rates here are based on the constant injection-well pressure, 150 bar. **Figure 5.5** shows the injection rates for both the strong- and weak-foam simulations. These injection rates have been made dimensionless by dividing by the injection rate of water into a water-filled reservoir using the same initial conditions and operating constraints.

The injection rate for the strong foam is nearly constant from the point where it has swept about 5% to over 85% of the reservoir, as in the radial-flow model (Figure 5.1). The rate then drops suddenly as gas reaches the production well (after about 98% of the reservoir is swept). The first effect of foam reaching the production well is to greatly reduce productivity index of the production well and therefore, indirectly, the injection rate. The weak-foam simulations show a gradual increase in the injection rate until foam reaches the producer, which occurs after about 90% of the reservoir has been swept. The magnitude of the increase in injection rate is less than in the radial-flow model (Figure 5.1b), which might reflect either less increase in mobility near the injection well because of the finite-size grid (cf. Leeftink et al. (2015)) or an early breakthrough of gas and end of the process. The lower value of areal sweep for the weak foam as foam reaches the production well is a result of the uneven front illustrated in Figure 5.4. The sudden drop in injection rate as foam affects the production well is consistent with the findings of Namdar Zanganeh and

Rossen (2013). After the drop indicating arrival of foam at the production well, the injection rate rises again gradually as mobility in the production-well grid block increases (not shown in Figure 5.5). The injection rate is about twice as great for the weak foam as compared to the strong-foam case, thus reducing the time required to complete the process, but also leading to a reduction in sweep and a less-constant gas requirement over the process.
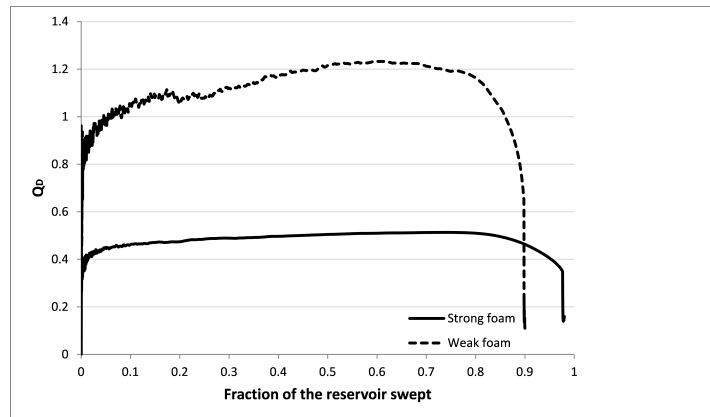
Figure 5.5: Dimensionless injection rate as a function of the swept fraction for both the strong- and weak-foam simulation.

5.4.3   Grid Effects

Leeftink et al. (2015) find that finite-difference simulations underestimate the effects of dry-out increasing injectivity in a SAG process and indicating the importance of a very fine grid resolution near the injection well. To check whether this has any influence on the outcome of the simulations we carried out a simulation using a coarser grid. Most of the simulations discussed here use a grid size near the well of 0.2 m. The coarse-grid simulation performed here uses a uniform grid size throughout the reservoir of approximately 0.7 m. Still 100x100 grid blocks are used in this new simulation and the parameter values for the strong foam were used. The resulting injection rates for the coarse- and fine-grid simulations are shown in **Figure 5.6**. These show a rather limited influence of the grid resolution, although the injection rate rises faster at short times with the finer grid, i.e. in better agreement with the radial flow model.
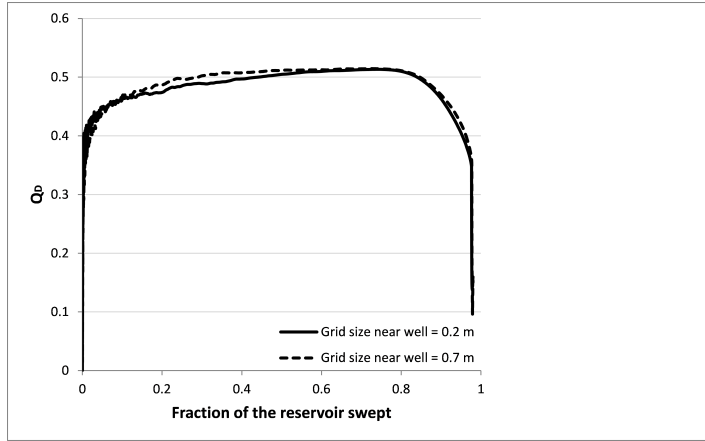
Figure 5.6: Dimensionless injection rate as a function of the swept fraction for strong-foam simulations: effect of grid resolution near injection well.

5.5   RELATION TO IDEALIZED SAG MODEL OF DE VELDE HARSENHORST ET AL. (2014)

The finding that the pressure difference across the foam bank during gas injection in a SAG process holds nearly constant in time accords with the idealized model for SAG processes developed by Shan and Rossen (2004) and extended by de Velde Harsenhorst et al. (2014) and Grassia et al. (2014). In that extremely simplified model, all the resistance to flow in the foam bank is concentrated in a narrow front located at the leading edge of the gas bank; the narrow front has width τ, which grows with distance traveled, consistent with the behavior of spreading waves in the method of characteristics. In radial flow, when the gas bank has traveled distance r_f,

$$\tau = \tau_D r_f \tag{5.11}$$

where τ_D is a constant, as is the relative mobility of gas in the foam bank r_f. τ_D is related to parameter τ^* in the model of de Velde Harsenhorst et al. as shown below. Dimensionless time, and therefore injection rate, are defined in terms of the ratio (τ_D/λ_{rf}). Mobility is assumed infinite (i.e., so large that it is unimportant) in the water ahead of and in the gas bank behind this narrow front of low mobility at the leading edge of the gas bank. In radial flow, with no gravity, the pressure rise at the injection well in this model is

$$p(r_w) - p(r_f) = \frac{Q}{2\pi Hk}\left(\frac{\tau_D}{\lambda_{rf}}\right) \tag{5.12}$$

The leading edge of the gas bank, as a function of time in radial flow, is given by

$$r_f = \sqrt{\left(\frac{2k[p(r_w) - p(r_f)]}{(1 - S_{wf})\phi}\left(\frac{\lambda_{rf}}{\tau_D}\right)t\right)} \qquad (5.13)$$

where S_{wf} is the water saturation in the foam bank. Dimensional and dimensionless injectivity of the foam bank (Eqs. (5.7) and (5.8)) are given by

$$I_f = 2\pi Hk\left(\frac{\lambda_{rf}}{\tau_D}\right) \qquad (5.14)$$

$$I_{fD} = \frac{\left(\frac{\lambda_{rf}}{\tau_D}\right)}{\left(\frac{\lambda_{rt}^I}{\ln(r_e/r_w)}\right)} \qquad (5.15)$$

By equating Eqs. (5.9) and (5.12) we can relate the parameters of the idealized model to the parameters derived for real foams based on laboratory data:

$$\left(\frac{\tau_D}{\lambda_{rf}}\right) = \int_{\varepsilon}^{\eta_{shock}} \frac{1}{2\lambda_{rt}(S_w(\eta))}d\ln\eta \qquad (5.16)$$

Parameter (τ_D/λ_{rf}) does not depend on density difference between phases. The corresponding parameter in the model for gravity segregation of de Velde Harsenhorst et al. (2014) is (τ^*/λ_{rf}), with

$$\left(\frac{\tau_D}{\lambda_{rf}}\right) = \left(\frac{\tau^*}{\lambda_{rf}}\right)\frac{\Delta\rho g}{p(r_w) - p(r_e)} \qquad (5.17)$$

where $\Delta\rho$ is the density difference between gas and aqueous phases. For the Persoff foam model (Figure C.1a) (λ_{rf}/τ_D) = 48 (Pa· s)$^{-1}$ and $S_{wf} = 0.37$; and for the "weak foam" model (Figure C.2b) (λ_{rf}/τ_D) = 651 (Pa· s)$^{-1}$ and $S_{wf} = 0.37$. These values are obtained by evaluating the integral in Eq. (5.16) for each model.

We check the radial propagation rate by evaluating Eq. (5.13) for a fixed time (t = 15 days for the Persoff model and t = 4 days for the weak foam model) and compare with the result obtained from the STARS simulation. The required

value of λ_{rf}/τ_D is obtained from Eq. (5.15) where values for I_{fD} equal to 0.4 and 4.5 are used for the Persoff and weak foam model respectively. The fixed times 15 and 4 days for the Persoff and weak foam model are chosen such that the deviation from the radial profile is limited (see **Figures 5.7** and **5.8**).
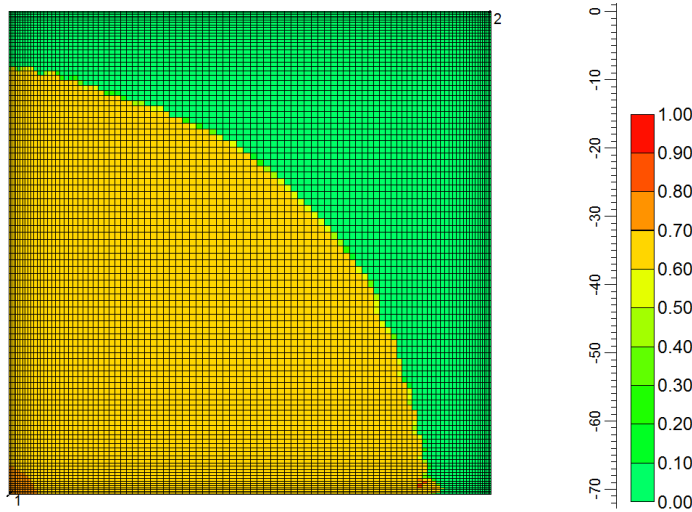
Figure 5.7: Gas saturation profile for the Persoff model at t = 15 days
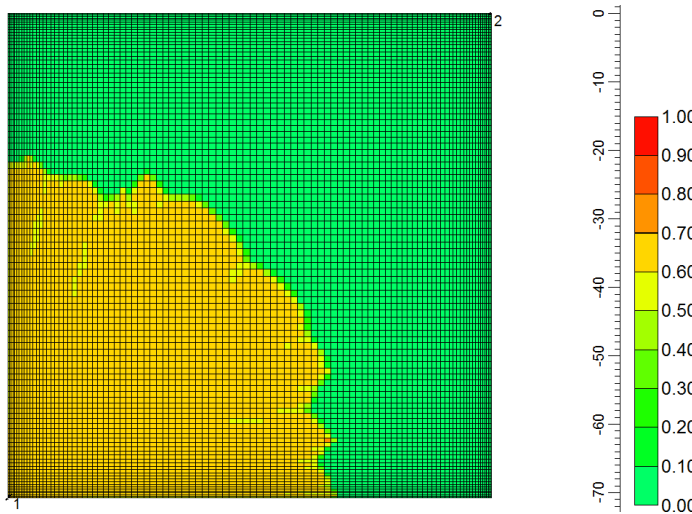
Figure 5.8: Gas saturation profile for the weak foam model at t = 4 days

From these figures we find that the foam front has advanced radially for approximately 60 meters in the Persoff model at t = 15 days whereas for the weak foam model the foam front is at 47 meters after 4 days.

According to the analytical expression for the radial position (Eq. (5.13)), the foam front is at r_f = 70 m for the Persoff model at t = 15 days and r_f = 133 m for the weak foam model at t = 4 days. The foam appears to propagate much faster

according to the analytical model compared to the STARS simulations. Propagation rates are approximately 17% faster for the Persoff model and up 183% faster for the weak foam model. In part, this discrepancy can be attributed to the assumption that all of the pressure drop occurs within the foam bank. The geometry of the quarter five-spot causes a large pressure drop near the production well as the flow converges towards it. We account for this below. Also, compressibility plays a modest part. Injected gas volume in the simulations is reported at the injection-well pressure of 150 bar. We expect most of the pressure difference between the injection well and the production well pressure of 100 bar to occur towards the front of the gas bank and near the production well, but an effect of gas expansion of order 10% is likely. Finally, gas mobility near the injection well is greater in the analytical model as shown in **Figures 5.9a and b**. The total mobility in the first grid block is 35% higher for the analytical model than for the numerical simulation. The lower mobility in the numerical simulations is caused by the finite grid size near the well which cannot resolve the drastic increase in mobility completely in the way the analytical solution can (Leeftink et al. (2015)). The large difference in the results for the weak foam case are, in part, caused by viscous fingering which occurs in the numerical simulations (**Figure 5.10**) (Farajzadeh (2013)). This figure shows the total mobility in the reservoir at $t = 8$ days. This time was chosen as fingering is clearly observed here. The color scale of the figure is clipped to emphasize the fingering within the foam bank. This effect is not taken into account in the idealized model and strongly affects the foam propagation rate due to large regions of very low mobility at the foam front.
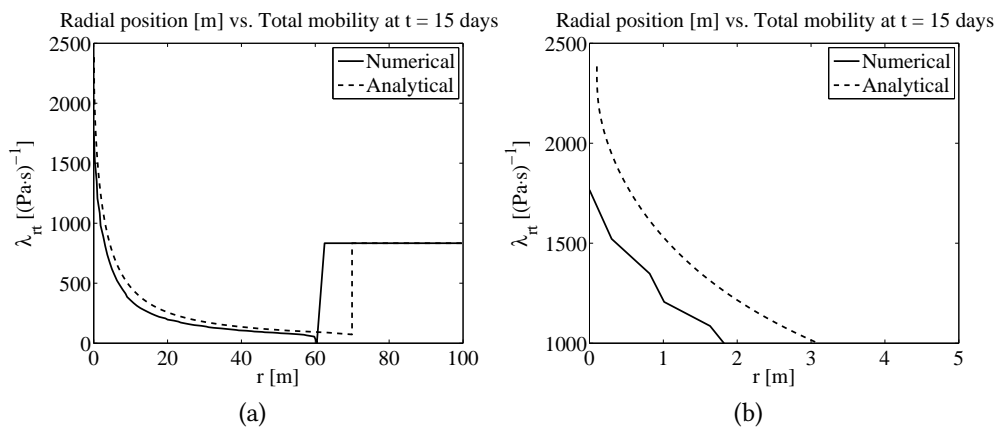
Figure 5.9: (a) Total mobility as a function of position for the strong-foam 5-spot simulation at $t = 15$ days. Position r is given along the diagonal between the two wells (b) Same plot, but zoomed in on region near the injection well to emphasize the difference in mobility in that region.
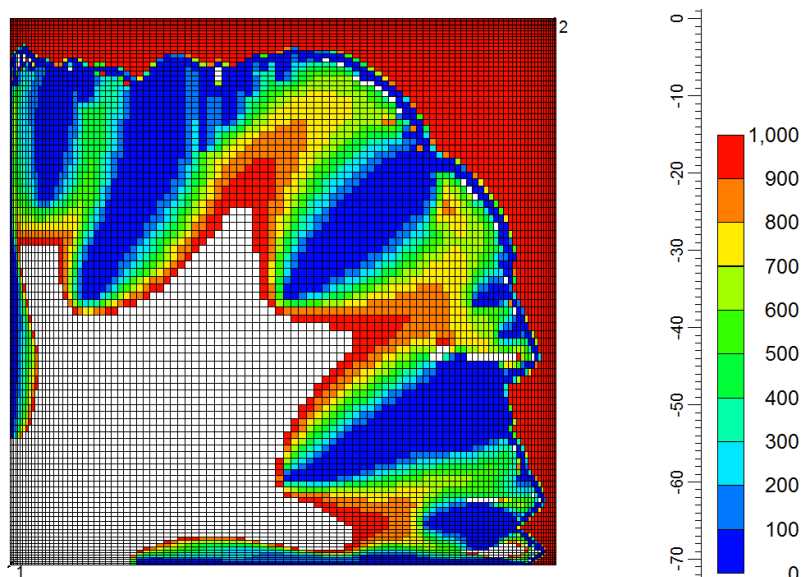
Figure 5.10: Total mobility $[(\text{Pa s})^{-1}]$ at $t = 8$ days throughout the reservoir for the weak-foam simulation clearly showing viscous fingering within the foam bank.

5.6 ACCOUNTING FOR RADIAL FLOW INTO THE PRODUCTION WELL

The 2D quarter five-spot simulation shows a less pronounced effect of foam on the injectivity compared to the radial flow model. For the Persoff model we find that the injectivity is not reduced as much in the 2D simulations as in the radial-flow model, whereas in the weak foam model the opposite effect is observed (i.e. 2D simulations show lower injectivity than analytical model). This discrepancy can, in part, be attributed to the more complex geometry of the quarter-five-spot in which the radial flow approximation does not always hold. A better approximation of this geometry would be to divide the geometry in two parts. Close to the injection well, there is radial flow out from the well. However, near the production well the flow is radially inward.

We consider the scenario where there is radial flow of foam out from the injection well and radial flow of water into the production well. This introduces an additional term in the expression for the pressure drop. which takes into account the pressure drop over the water-saturated region near the production well. We assume that most of the pressure drop occurs near the two wells, which means that the pressure drop over the inflow part of the pattern (near the production well) can be considered constant. At the start of the gas-injection process ($t_D = 0$), we assume that the inflow part of the process accounts for half of the total pressure drop across the quarter five-spot pattern. The pressure drop over the outflow part of the pattern consists of the pressure drop over the foam bank and the pressure difference over the water-filled region ahead of the

foam bank as in Eq. (5.3). Finally, we normalize the expression for the pressure difference for the fact that in- and outflow each account for half of the pressure drop in the pattern. The resulting expressions for the dimensionless pressure difference and injection rate are given by

$$\Delta p_D = \frac{\left[1 + \frac{1}{I_{fD}} + \frac{\ln\left(r_f/r_e\right)}{\ln(r_w/r_e)}\right]}{2} \tag{5.18}$$

$$Q_D = \frac{1}{\Delta p_D} \tag{5.19}$$

The resulting injection rates for the Persoff and weak foam model using the new expression for the pressure drop are shown in **Figure 5.11** as a function of the swept fraction of the reservoir, to allow for direct comparison with the STARS simulations. The calculation is carried out until the foam front reaches $r_f = r_e/2$. At that time the swept fraction is equal to $\pi/8$. The injection rates obtained in this way show better agreement with the STARS simulations although there is still a significant difference in magnitude between the two solutions.

The nature of the deviation - lower injectivity in the simulations than in the model - is in the direction expected given the effect of compressibility discussed above, inaccuracies in representing mobility in the injection-well grid block in the simulations (Leeftink et al. (2015)) and viscous fingering (Figure 5.10). Poor grid resolution is a fault of the simulation and failure to account for viscous fingering a weakness of the simple radial-flow model. The fit to the Persoff model is remarkably good. The fit even to the weak-foam model (about 40%) is reasonably good given all the simplifications in the model. Based entirely on the fractional-flow curve, one can make a quick estimate of injection rate needed to maintain injection pressure constant at the desired value in this 5-spot pattern.

5.7 CONCLUSIONS

Shan and Rossen (2004) show the advantages of a single-slug foam SAG process for overcoming gravity segregation in homogeneous reservoirs. They conclude that the best process is one that maintains injection pressure at its maximum allowable value throughout the period of gas injection. The effects of oil on foam and of mobile oil on three-phase mobilities is an additional complication to applying this model quantitatively. We believe however that the principles
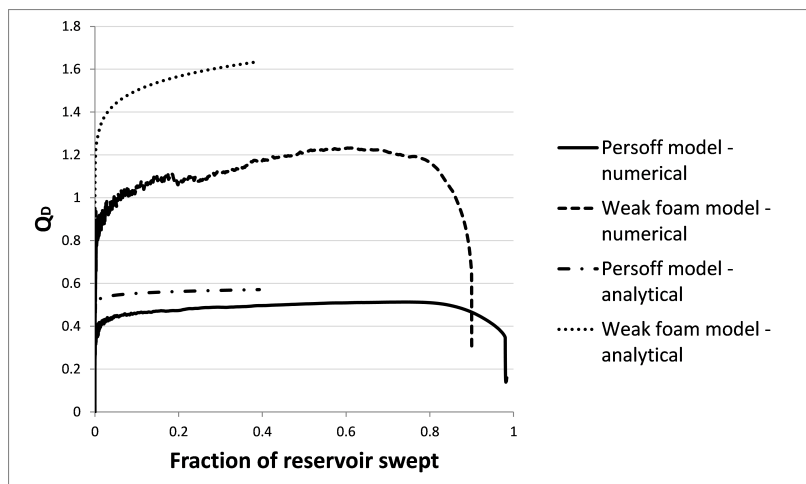
Figure 5.11: Dimensionless injection rate for Persoff and weak foam model using in-flow term in the pressure-drop equation, along with results from the numerical simulations.

derived here apply more generally than the specific simplifying assumptions made in the derivation. Our conclusions are as follows:

1. For a single-slug SAG process, the pressure difference across the foam bank during gas injection is nearly constant in time, if foam collapses or substantially weakens near the injection well.

2. If the injected foam is much less mobile throughout the foam bank than the fluids ahead of foam ("strong foam" case), then the injection rate required to maintain injection pressure constant is also nearly constant, at least during the period of radial flow around the injection well. The injection rate of gas is relatively small, however.

3. If the foam is just able to maintain mobility control with the fluids ahead of it ("weak foam" case), then injection rate must increase with time to maintain injection pressure at its optimal value. Such a process accelerates oil production, but the gas supply and production facilities must be prepared for increasing injection and production rates.

4. Simulations of a five-spot pattern agree reasonably well with the model based on radial flow. For a foam much less mobile than the fluids initially in the reservoir, the injection rate is nearly constant for the period where foam has swept from about 5% to over 95% of the pattern. For a weaker foam, just a bit less mobile than the fluids ahead of it, injection rate increases with time. The weaker foam also produces an uneven displacement front and earlier gas breakthrough.

5. Observed differences between the radial-flow model and quarter-five-spot simulations can, in part, be explained from the more complex geometry in the latter pattern. This pattern comprises both radial outflow and inflow parts. The inflow part, where the water flow converges towards the production well, introduces an additional pressure drop compared to the simple model which only accounts for radial outflow from the injection well. A better fit to the STARS simulations is found when incorporating the additional term in the expression for the pressure drop.

6. One can derive the implications for injectivity directly from the fractional-flow curve for foam using Eq. (5.10), at least in a region around the well where mobile oil is not present, and as long as the fractional-flow function accounts for the presence of immobile oil at the given saturation. One could use this approach to guide selection of a foaming agent, based on the available gas stream for a given project and the flexibility of the injection and production facilities.

7. One can also relate foam parameters obtained in the laboratory to the idealized SAG foam model of de Velde Harsenhorst et al. (2014), which predicts behavior similar to that shown in simulations with more complex models. The foam-front propagation rates obtained using the idealized model is similar to that found in the STARS simulations. Observed differences with our simulations can be attributed in part to the effects of compressibility and underestimation of the total mobility at the well in the simulations, which are an effect of the discretization of the domain in the simulation.

6

FOAM FLOODING IN CARBONATE ROCKS

6.1 INTRODUCTION

A common method of improving oil recovery from a reservoir is through the injection of gas in order to displace the oil and maintain pressure. The main problem with gas injection is that it suffers from poor sweep efficiency. Reasons for this include viscous fingering (due to the mobility contrast between the injected gas and the displaced phase), channeling (gas prefers to flow through high-permeability layers, thus low-permeability layers remain unswept) and gravity override (the injected gas has a lower density then the oil in place, therefore flowing to the top of the reservoir, causing an unswept lower region in the reservoir). Foam can help alleviate these problems by trapping the gas in bubbles, thereby reducing its mobility. This results in a more stable displacement front and thus an increase in volumetric sweep (Schramm (1994); Kovscek and Radke (1994); Rossen (1996)).

In this study we focus on the application of foam in carbonate formations. These rocks pose some specific challenges which need to be overcome in order for foam to be an effective method of enhancing the oil recovery. One of the main problems with carbonate reservoirs is that they typically have low permeability compared to sandstone reservoirs. Ehrenberg and Nadeau (2005) provide average values of porosity and permeability for over 40,000 reservoirs worldwide. As shown in **Figures 6.1a** and **b**, they find that carbonates on average have a significantly lower porosity than sandstone reservoirs, which leads to a lower average permeability as well. The effectiveness of foam in controlling gas mobility is greater in higher-permeability media as was first identified by Bernard and Holm (1964). Other studies including Falls et al. (1988); Khatib et al. (1988) and Moradi-Araghi et al. (1997) also find reduced effectiveness of foam in lower permeability media. Still, Szlendak et al. (2012) found that in-situ foaming enabled mobility control in tight ($\approx$10 mD) formations.

Foam has been studied extensively in heterogeneous rocks. When it comes to large-scale heterogeneities, such as layered reservoirs, foam injection is of-
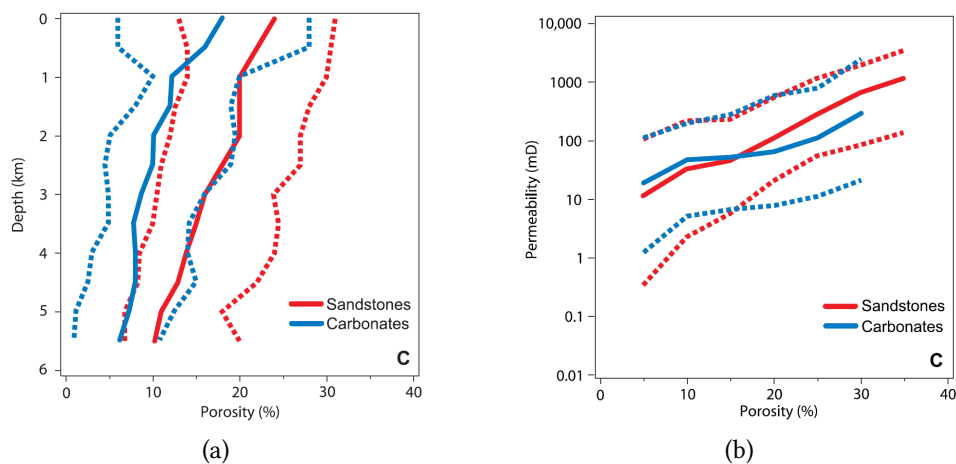
Figure 6.1: Global average (a) porosity vs. depth and (b) porosity vs. permeability plots for sandstone and carbonate reservoirs. The lines respectively represent the P10, P50 and P90 values (from Ehrenberg and Nadeau (2005)).

ten considered as an enhanced oil recovery method. This is because of the afore-mentioned advantage of foam that it reduces the mobility more in high- than in low-permeability zones. Thus in layered reservoirs, which would otherwise suffer from poor sweep efficiency, the use of foam means gas can be diverted to low-permeability zones, thereby increasing the sweep (e.g. Tsau et al. (1998)). Also, Bertin et al. (1999) found that when a layer of sandstone ($k = 0.1$ D) is in communication with a layer of unconsolidated sand ($k = 6.7$ D), then the foam front propagates at the same rate in both layers despite the large permeability contrast. Li et al. (2012) successfully used foam to recover remaining oil from a layered sandpack with a permeability contrast of 34:1 between the high- and low-permeability layer. Tanzil et al. (2002) found that foam can be more effective in heterogeneous bead-packs when the layering is perpendicular to the direction of flow. In these cases mobility reduction can be up to two orders of magnitude higher in the heterogeneous compared to homogeneous packs. This is caused by the increase in lamella-generation by snap-off across an abrupt increase in permeability.

On the other hand, fractures are often found to have a detrimental effect on foam stability. Haugen et al. (2012) found very low pressure build-up in fractures, indicating limited foam generation. Kovscek et al. (1995b) also found that foam generated in a rough-walled fracture was less resistant to flow than foam generated in a Berea foam generator. They argue that this is caused by the limited number of snap-off sites in the fracture, resulting in larger bubbles.

Rock wettability is another major concern for foam generation. Carbonate formations tend to be either mixed-wet or oil-wet (Alotaibi et al. (2010)). Suf-fridge et al. (1989) found limited foaming was possible in their Berea cores

which were modified to render them oil-wet. Sanchez and Hazlett (1992) observed that a wettability change to a more water-wet state was required in their beadpack experiments in order for foam to be generated. In Chapter 2 we show the reduced effectiveness of foam in oil-wet media, but also that foaming surfactants can be capable of changing an oil-wet medium to a more water-wet state.

One common problem with steady-state foam experiments is that multiple steady states can exist. Several coreflood experiments (Ransohoff and Radke (1988); Gauglitz et al. (2002)) find that with foam, the pressure gradient over the core is not necessarily a unique function of the superficial velocity. Ransohoff and Radke (1988) argue that there is a critical velocity above which lamellae division and snap-off are the dominant foam generation mechanisms, resulting in stronger foam. An example of this is shown in **Figure 6.2a**, from Gauglitz et al. (2002), who studied pressure gradient as a function of flow rate in a foam flood using Boise sandstone as the porous medium. They found that both strong (high ∇p) and weak (low ∇p) foam can exist at the same flow rate. In their liquid-saturation measurement, Kibodeaux and Rossen (1997) found that the water saturation is not monotonically increasing with increasing water-fractional flow (**Figure 6.2b**). They argue that weak and strong foam have separate fractional flow curves and the shift in the overall fractional flow curves is where there is a change between the two regimes.
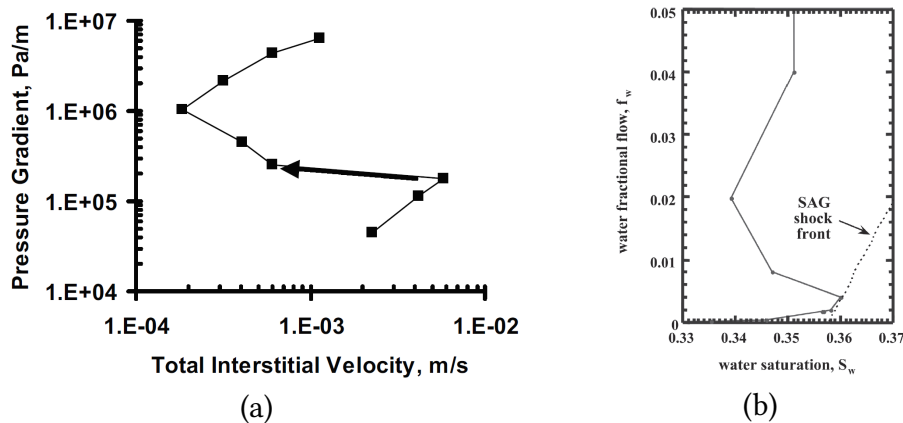
Figure 6.2: Multiple steady states during foam-flooding experiments: (a) more than one state can exist at a given flow rate (from Gauglitz et al. (2002)), (b) the fractional-flow curve is not a single-valued curve, caused by the presence of multiple foam regimes (measurements from Kibodeaux and Rossen (1997).

In this Chapter we study the ability of foam to be generated in a low-permeability carbonate. Our main set of foam-flood experiments are performed at high pressure (100 bar back-pressure), elevated temperature (55°C) and high salinity (200,000 ppm). Initially we focus on tests without the presence of crude oil to determine whether foam generation is possible in these rocks. Especially the

behaviour at high foam qualities (gas fractional flow) is of interest, because we show whether the foam generated in these rocks is suitable for a SAG injection process (Shan and Rossen (2004); Rossen and Bruining (2007)). As discussed in Chapter 4, it is crucial to know the behaviour at high foam quality in order to determine whether a SAG process can be successful. Afterwards we perform experiments with crude oil added to the co-injection process to determine its influence on foaming performance. Another experiment is aimed at determining the influence of rock heterogeneity on foaming performance. This experiment is carried out using a heterogeneous, vuggy carbonate core which is placed inside a CT scanner.

6.2   EXPERIMENTAL SETUP AND PROCEDURE

The setup used for the main set of experiments is similar to the one used in the porous-media screening tests as described in section 2.2.2. The main change is the use of 40-cm-long, 4-cm-diameter consolidated Indiana limestone cores instead of 13-cm-long beadpacks. To accommodate these cores, a longer core holder has to be used; it is mounted vertically in the thermobath. The operating conditions remain the same compared to the screening experiments (100 bar back-pressure, 55 °C and 200,000 ppm salinity). To analyze the pressure inside the core four differential pressure transducers (Endress+Hauser Deltabar S PMD75, range 0-3 bar) were installed to measure pressure drops within different sections of the core. In addition, another differential pressure transducer (Endress+Hauser Deltabar S PMD75, range 0-40 bar) was installed to measure the pressure drop over the entire core. Absolute pressure transmitters were installed up- and downstream of the core to monitor absolute pressure in the system; it can also be used to check whether the differential pressure measurements are correct. In all of the experiments described here, the flow direction is from the bottom of the core to the top. An overview of the setup used for this set of experiments is given in **Figure 6.3**.

Experiments were performed with two different surfactants at a salinity of 200,000 ppm. The surfactants were chosen based on their foaming performance as described in Chapter 2. Here we refer to these surfactants by their chemical name. We selected a non-ionic alkylpolyglycoside (hereinafter APG) and an anionic alcohol ethoxy sulphate (hereinafter AES). As in the screening experiments, we use a surfactant concentration of 0.5 wt./wt.% active content. The brine recipe is also the same as the one we used before with a salinity of 200,000 ppm(cf. Table 2.2).

In addition, another foam-flooding experiment was performed with a shorter, 17 cm, carbonate core inside a CT scanner (Siemens, 3rd generation). The core
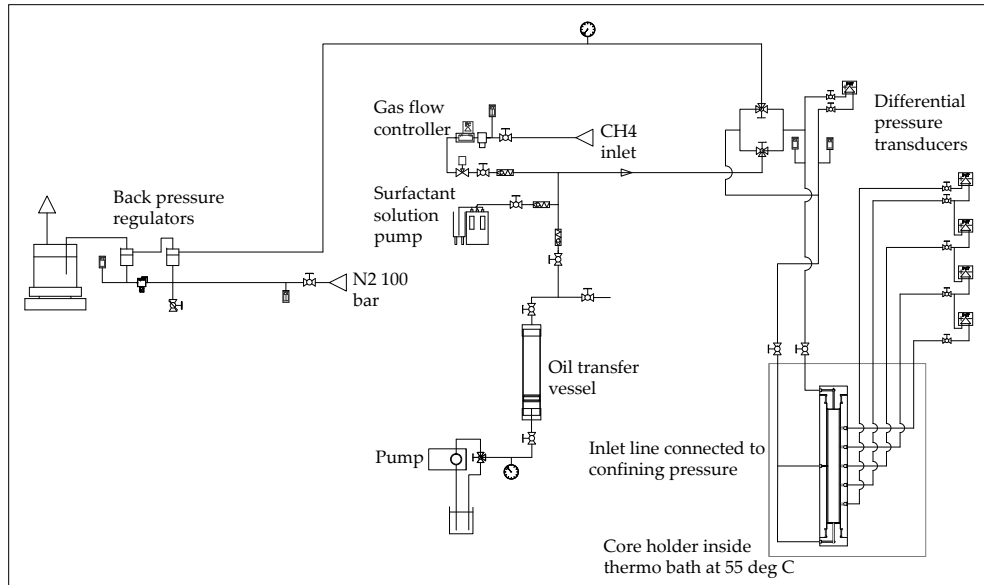
Figure 6.3: Schematic overview of setup used in long core experiments

is mounted vertically inside the opening of the CT scanner. This limits the size of the core that can be used. The rock used in this experiment was Edwards White, which is a heterogeneous, vuggy carbonate. These experiments were performed to determine the fluid saturations within the core. This experiment was designed to test whether the high level of heterogeneity of the cores in combination with their vuggy nature has a significant impact on the foaming performance. We were not trying to mimic reservoir conditions in these CT experiments, but rather generate as strong a foam as possible. This means performing the experiments at room temperature and using zero-salinity solutions. For safety reasons we make use of nitrogen gas for the CT experiments rather than the methane that is used in the other experiments in this chapter. The back-pressure is kept at 100 bar (i.e. the same as the other experiments) to avoid significant effects of compressibility. The surfactant used for this experiment is the non-ionic alkylpolyglycoside (APG) that is also used in the longer-core, Indiana limestone foam floods. A schematic of this experimental setup is given in **Figure 6.4**.

Two differential pressure transducers were installed to measure the pressure drop over the entire core and the middle segment of the core, respectively. In addition, two absolute-pressure transducers were used to monitor the pressure at the outlet of the core and at the end of the middle segment. In this way, the pressure in each segment could be monitored separately. This allowed for checking heterogeneity of the core in terms of permeability: that is, at least in a single-phase waterflood, sections of the core which cause higher pressure
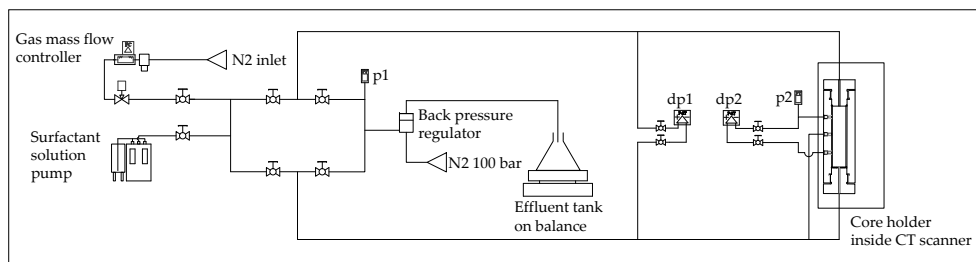
Figure 6.4: Schematic overview of setup used in CT visualization experiments

gradient have a lower effective permeability than sections with lower pressure gradient.

6.2.1   *Procedure*

Procedures for both the long-core and the CT experiments are similar to the procedure used in the screening experiments in bead-packs, as outlined in **Section 2.2.2**. Foam-flooding experiments are carried out using co-injection of gas and surfactant solution (0.5 wt./wt.% active content). The pressure drop over the core is monitored during the experiment and the effect the foam has on this is determined. The heterogeneity in the core in terms of permeability is also assessed by monitoring and comparing pressure drop in the different sections of the core. For the long-core experiments, the main goal is to perform steady-state foam floods at varying foam qualities. This will result in a plot of f_g vs. ∇p similar to those we used in our analysis in Chapters 3 and 4. We are especially interested in foam behaviour at very high foam qualities, because this is crucial for predicting the mobility of the gas front in a SAG-injection process (as discussed in Chapter 4). Thus we focus our experiments at foam qualities larger than 0.5, up to foam quality 0.99. We aim to construct fractional-flow curves based on experimental results. To determine whether the foam could be applied in a SAG process, one must find the point of tangency to the fractional-flow curve and the mobility at that point, which corresponds to the mobility of the foam front in a gas injection cycle of a SAG process. As in Chapter 4, because we focus on behaviour in the high-quality regime; we do not expect strongly shear-thinning behaviour and make use of the version of the STARS foam model that only incorporates the water-saturation-dependent function F_2. Thus we use the following functional form of the foam model:

$$FM = \frac{1}{1 + fmmob \cdot F_2} \tag{6.1}$$

For the CT experiment, we run the experiment until a steady state is reached. In addition to the overall steady-state pressure response we also observe the distribution of water saturation inside the porous medium. Especially the behaviour inside and around the vugs is of interest, as these are fairly large in size relative to the dimensions of the core, and may have significant impact on the development of foam.

6.3 RESULTS AND DISCUSSION

6.3.1 *Results From Long-Core Experiments*

Before starting foam injection, we measured the steady-state pressure gradient due to a single-phase water flood for different flow rates in order to measure the liquid permeability. The core is fairly homogeneous and has a permeability of 1.01 mD. In a separate test, the porosity of small (3.5 cm length, 3.1 cm diameter) core plugs of the same rock was measured using a Quantachrome Ultrapycnometer 1000. In total the porosity of 11 core plugs was measured and the average porosity was found to be 0.13.

The main results from the experiments performed using the long Indiana Limestone cores are pressure-drop measurements aimed at determining foam's ability to reduce total mobility. As mentioned above, the mobility of the foam at the front in a SAG injection process is defined by a point of tangency to the fractional-flow curve. Results presented here are mainly steady-state pressure-gradient over the mid-section of the core, excluding the entrance and exit regions. The foaming performance in the entry and exit regions of the core may not be representative for the overall foaming performance and are thus neglected. For the long-core experiments this means we use the cumulative pressure gradients as measured by the four internal pressure transducers.

The results are pressure-gradient measurements at varying foam qualities, but at fixed total superficial velocity, focused primarily on the high-quality regime. We can fit the STARS parameter values using the method outlined in Chapter 4. For the first experiment, we check whether the entrance and exit regions of the core significantly affect the foaming performance by comparing the pressure gradient over the entire core to that in the middle section. **Figure 6.5a** shows the pressure-gradient data for the experiment using the APG surfactant and an initial straight-line estimate as a fit. **Figure 6.5b** shows the result from the same experiment for the middle section of the core. The pressure gradient in the latter plot is approximately 25% higher than the result including the entry and exit regions. The section of the core where the pressure was mea-

sured is 67% of the total length of the core (26.8 vs. 40 cm) and the pressure drop measured in that section varied from 80 to 85% of the total pressure drop.

This means that the foam in the core as a whole is significantly weaker compared to the mid-section. We only use the pressure result from the mid-section of the core for the remainder of the analysis presented here. The total superficial velocity is kept constant in these measurements at 0.05 ml/min which for a 4-cm-diameter core is equivalent to $6.63 \cdot 10^{-7}$ m/s.

(a)   (b)
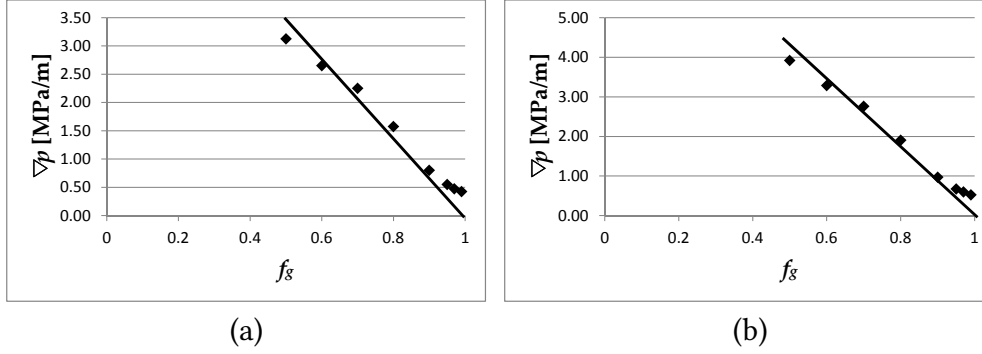
Figure 6.5: Steady-state pressure gradient (∇p) for the experiment using the APG surfactant as a function of foam quality (f_g). All data points are in the high-quality regime. Straight-line fit is first estimate and is used to estimate limiting water saturation S_w^*. (a) steady-state pressure gradients based on the pressure difference over the entire core (b) results without entry and exit regions.

All of the experimental data appear to be in the high-quality regime, which is indicated by the fact that with increasing foam quality, the pressure gradient decreases. A straight line provides a first-estimate fit through the data-points. This straight line trend also implies that the water relative permeability remains fairly constant here. We can use this to determine the limiting water saturation S_w^*, which corresponds to the STARS model parameter $fmdry$. We can determine the water relative permeability in the high-quality regime by rewriting Darcy's law as follows:

$$k_{rw}\left(S_w^*\right) = \frac{u_t \mu_w \left(1 - f_g\right)}{k \nabla p} \tag{6.2}$$

where f_g and ∇p are obtained from the straight-line fit through the data (cf. Chapter 3). For this data-set the value of $k_{rw}\left(S_w^*\right)$ is $5.0 \cdot 10^{-2}$. To accurately determine the value of $fmdry$, suitable gas and water relative permeability functions are needed. Mohamed and Nasr-El-Din (2012) provide relative-permeability curves for several carbonate rocks, including low-permeability

Indiana Limestone. We fit a Brooks-Corey-type relative-permeability function to their data with the following result:

$$k_{rw} = 0.28 \left(\frac{S_w - 0.32}{1 - 0.32 - 0.08} \right)^{2.41} \tag{6.3}$$

$$k_{rg} = 0.05 \left(\frac{1 - S_w - 0.08}{1 - 0.32 - 0.08} \right)^{1.02} \tag{6.4}$$

The value of S_w^* (or $fmdry$) can be determined by rewriting equation (6.3) into an expression for the saturation and using the aforementioned value of $k_{rw}\left(S_w^*\right)$. The resulting value of $fmdry$ is 0.59.

In Chapter 3 we discuss that the value of $fmmob$ can be obtained from the foam quality at the point of transition between the low- and high-quality regime (f_g^*). In this experiment, all the data points are in the high quality regime so there is no transition point. This means that the values of f_g^* and $fmmob$ cannot be determined. This is not a problem in this case since we are interested only in the mobility at the gas front in a SAG process. As discussed in Chapter 4 the mobility at the gas front occurs at the point of tangency to the fractional-flow curve, which for a foam flood is in the high-quality regime. To determine the point of tangency, first we need to determine the liquid saturations for all data points. We can then use the saturations to estimate the fractional-flow curve. The saturation can be determined in the same way we determined S_w^*, using the Darcy's law for the water phase along with the known relative-permeability function for k_{rw}.

The shock line is a straight line from the point of tangency to the initial condition (which in this case is at $S_w = 1$). The resulting fractional-flow curve fit along with the shock line from the point of tangency is shown in **Figure 6.6a**. A detailed view of the same fractional-flow curve around the point of tangency is shown **Figure 6.6b**, from which we can see that the water saturation at the point of tangency is equal to 0.581.

We then use the water saturation to determine the total mobility at the leading edge of the foam bank using equation (6.5) and compare it to the mobility of the displaced phase (in this case water):

$$\lambda_{rt}\left(S_w^t\right) = \lambda_{rw} + \lambda_{rg} = \frac{k_{rw}\left(S_w^t\right)}{\mu_w} + \frac{k_{rg}\left(S_w^t\right) \cdot FM\left(S_w^t\right)}{\mu_g} \tag{6.5}$$

where S_w^t is the water saturation at the point of tangency to the fractional-flow curve. For the experiment using the APG surfactant, the resulting value of $\lambda_{rt}\left(S_w^t\right)$ is equal to $1.42 \cdot 10^3$ [Pa·s]$^{-1}$. The experiment wass performed at 55°C at which the water viscosity is around 0.50 mPa·s (Kestin et al. (1978)).

Figure 6.6: (a) Water fractional flow for the experiment using the APG surfactant: points are experimental data where the liquid saturation is calculated using relative-permeability functions from data of Mohamed and Nasr-El-Din (2012). The resulting curve fit is obtained using the following STARS model parameter values: $fmmob = 20$, $fmdry = 0.59$, $epdry = 600$. Dashed line indicates shock from point of tangency back to initial state. (b) detailed view of the same fractional-flow curve around the point of tangency.

Therefore the mobility for water, which is the fluid that's being displaced, is $1/\mu_w = 2.0 \cdot 10^3$ [Pa·s]$^{-1}$. This means that the mobility of the leading edge of the foam bank is slightly lower than that of the water: $\lambda_{rt,foam}/\lambda_{rt,water} = 0.71$. Thus, the results indicate that, even though the foam is rather weak (i.e. has low apparent viscosity), it is still able to maintain mobility control over the displaced water phase. This result is similar to the 'weak foam' proposed in Chapter 5. Foam like this has the advantage that the injectivity is relatively high so a foam-injection process can be carried out in a shorter time. If used in the field, the resulting foam front may show some instabilities which could lead to lower sweep efficiency (cf. Section 5.4).

The fit through the pressure-gradient data of the APG experiment using the model parameters in Figure 6.6 is shown in **Figure 6.7**. Note that the transitional foam quality (f_g^*) is rather low for this set of parameters (around 0.25). This is a result of the chosen value of $fmmob$. Based on that value, the transitional foam quality would shift left or right, but the fit in the high-quality regime would remain the same (straight line through the data points).

We performed the same set of experiments using the same foam qualities with the AES surfactant. **Figure 6.8** shows the pressure-gradient results as a function of the foam quality. Apart from the lowest investigated foam quality ($f_g = 0.5$), all of the data points are in the high-quality regime. The straight line fit shown in the figure gives a first estimate of the behaviour in this regime.

The resulting water saturations are calculated using the same water relative-permeability function as before (i.e. Equation (6.3)) and are shown as fractional-
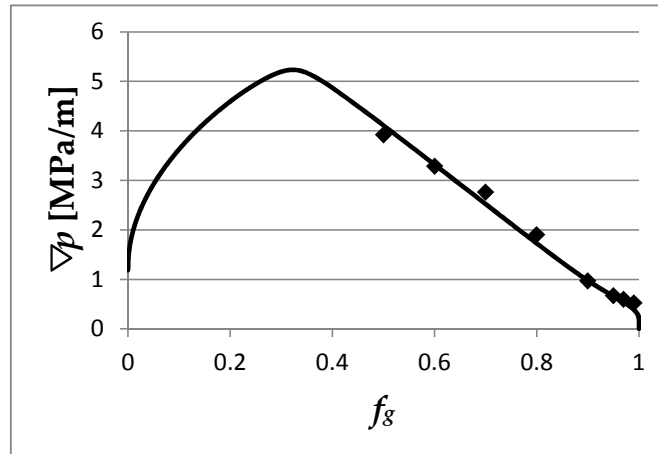
Figure 6.7: Steady state f_g vs. ∇p data for the experiment using the APG surfactant along with STARS model fit using the following parameter values: $fmmob = 20, fmdry = 0.59, epdry = 600$
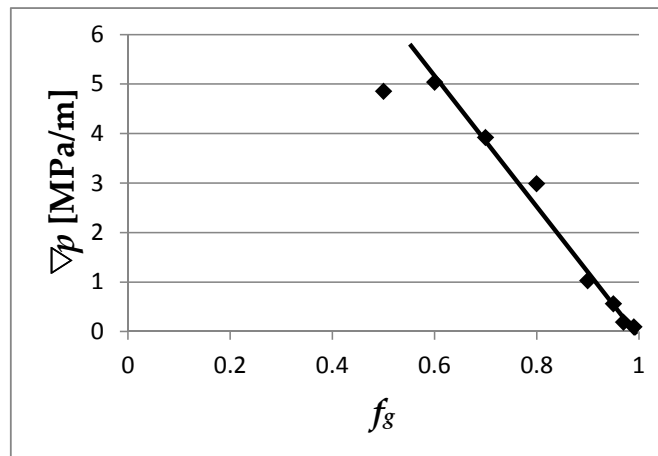
Figure 6.8: Steady state pressure gradient (∇p) for the experiment using the AES surfactant over the middle section of the core as a function of foam quality (f_g). All data points except the lowest foam quality studied ($f_g = 0.5$) are clearly in the high-quality regime. Straight line fit is first estimate and is used to determine limiting water saturation S_w^*.

flow data in **Figure 6.9a**. A more detailed close-up of the same fractional-flow data is shown in **Figure 6.9b**. The result shows that the water fractional flow is not a monotonically increasing function of the water saturation. This suggests that multiple steady states can be observed using this surfactant. This result is similar to that of Kibodeaux and Rossen (1997) and Xu and Rossen (2004), who also found multiple steady states can exist as discussed above. Rossen and Bruining (2007) argue that this kind of fractional-flow curve is actually a combination of two different curves, one for strong and one for weak foam. It is also possible that the large scatter in S_w values in Figure 6.9 may be the

result of experimental scatter. However, to bring the datum of $S_w = 0.62$ (at $f_g = 0.97$) down to $S_w = 0.57$, the measured pressure drop would have to be around 0.32 bar rather than the 0.21 bar that was measured. This is an increase of approximately 50%, which is beyond the expected scatter in our pressure measurements however.

According to Rossen and Bruining (2007), in such a case the shock goes to the weak-foam part of the fractional flow curve. Our fitting approach is not suitable for such data-sets and therefore we cannot fit the results from this experiment.

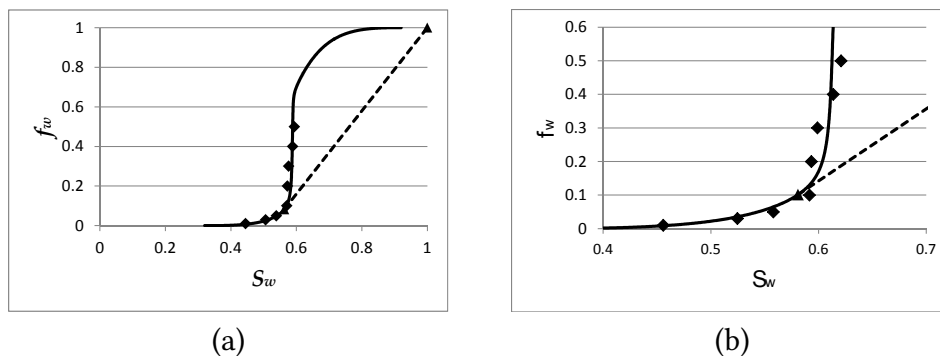(a)   (b)
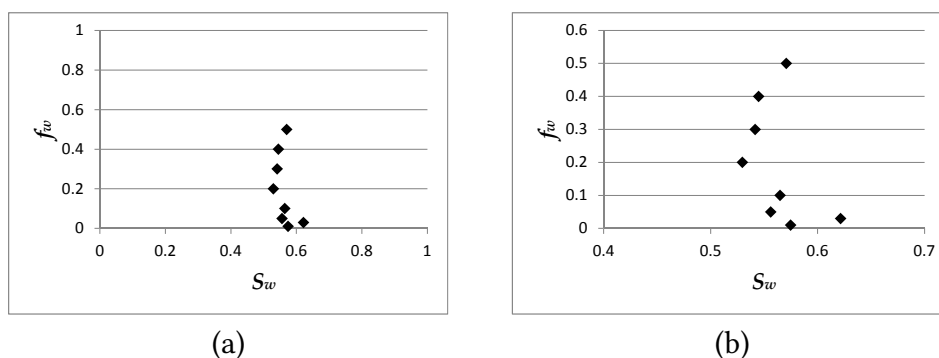
Figure 6.9: (a) Water fractional flow for the experiment using the AES surfactant: points are experimental data where the liquid saturation is calculated using relative permeability functions from Mohamed and Nasr-El-Din (2012). Multiple steady states can be observed (i.e. fractional flow does not increase monotonically with water saturation). (b) detailed view of the same experimental data more clearly showing the multiple steady-states in the fractional-flow curve.

THE EFFECT OF OIL   To determine the effect of oil on the foaming performance of both surfactants we performed an experiment where we added crude oil (32° API) to the co-injection process. The foam quality in this experiment is kept constant at $f_g = 0.5$. Without oil we managed to get a fairly strong foam at this foam quality with both surfactants so if there is any effect of the oil we should be able to clearly see it by a changing pressure gradient over the core. We maintained the same gas and surfactant solution that we also used in the previous experiment (i.e. 0.05 ml/min = $6.63 \cdot 10^{-7}$ m/s) and then we added the crude oil to the injection process. We do not include oil flow rate in the definition of foam quality. The oil flow rate used in these experiment is one quarter of the gas flow rate and since we use a foam quality of 0.5 this is also equal to one quarter of the surfactant solution flow rate ($Q_o = Q_g/4 = Q_w/4$). We first generated a foam in the core without oil and then started the oil-injection to see

its effect on the pressure gradient. **Figures 6.10** and **6.11** show the resulting pressure-gradient profiles for the APG and the AES experiment respectively. Both experiments are carried out using a salinity of 200,000 ppm. These plots comprise both the injection process without oil until a steady state is reached and the subsequent process where oil is co-injected along with the other fluids. The pressure gradient without oil is somewhat lower (3.0 vs. 3.9 and 4.8 MPa/m) than it was in the previous experiments even though the experimental conditions were kept constant. This could be the result of a change in permeability of the core. The same core was used throughout these experiments. Prolonged periods of liquid injection may have led to dissolution thereby affecting the permeability. It is also possible that some pollutants entered the system (e.g. impurities in the surfactant solution) which may have had a detrimental effect on the foaming performance.
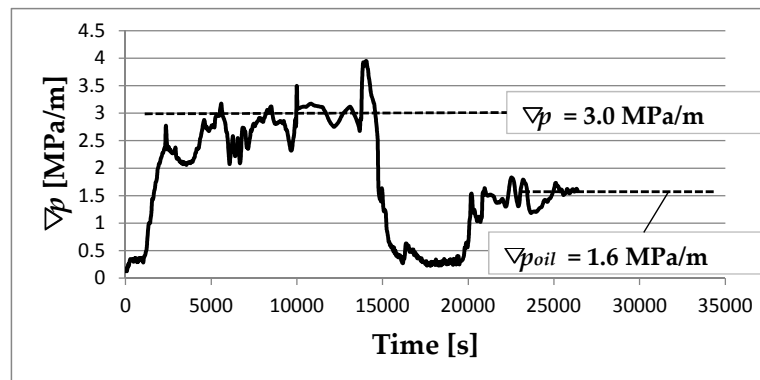
Figure 6.10: Pressure gradient results from the experiment with the APG surfactant when oil is added to the injection process. Steady state without foam is reached around $t = 14,000$ s after which oil injection is started, which reaches the core shortly thereafter.

Further observations show that both surfactants perform similarly. The maximum pressure gradient without oil is 3.0 MPa/m for both surfactants. Then when oil is added there is a short rise in the pressure gradient, because the oil has not yet reached the core, but the flow rate increases slightly. This is then followed by an abrupt decline in pressure gradient implying oil is destroying the foam almost completely. However, after this initial decline, a gradual increase in pressure gradient occurs meaning that some mobility reduction is again taking place. With oil, the steady-state pressure gradient is roughly halved compared to the injection process without oil for both surfactants (∇p =1.6 and 1.5 vs. 3.0 MPa/m).

We tried examining the foam structure qualitatively at the outlet of the core. We use RADEL tubing for our fluid lines which can be used at high pressure, but is still transparent, allowing "by eye" observations of the fluids inside. From our
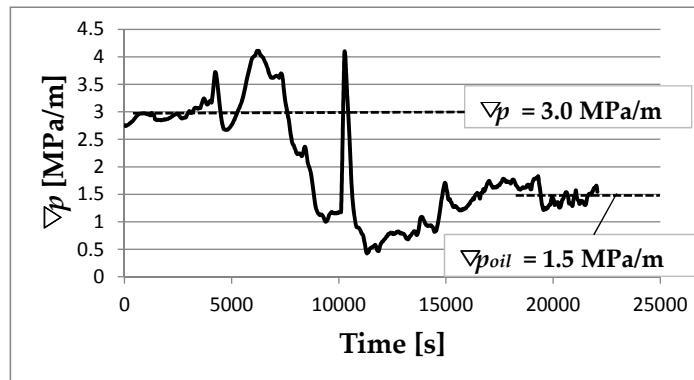
Figure 6.11: Pressure gradient results from the experiment with the AES surfactant when oil is added to the injection process. Steady state without foam is reached around $t = 5,000$ s after which oil injection is started, which reaches the core shortly thereafter.

qualitative observations we find that the fluids at the outlet of the core are more like an emulsion than a foam. A representative example of the observations is shown in Figure 6.12 which shows the fluids inside the RADEL tubing. Overall we find that foaming in the presence of oil is challenging in these rocks, but that some mobility reduction can still be achieved.

Figure 6.12: Fluids at the outlet of the core; appearing more like an emulsion than a foam.

6.3.2   *CT Experiments*

CT scans depend on attenuation coefficients which are different for every material. The original attenuation coefficients are commonly transformed into Hounsfield units (also known as CT numbers) using a linear transformation. Hence one can use these to distinguish the liquid (aqueous surfactant solution;

no oil), gas and the rock itself. To calculate rock porosity and fluid saturations inside the core we make use of the method outlined in detail in Rangel-German et al. (1999). Here we only mention the parts of their method relevant to our study (i.e. limited to two-phase flow), but we do use the same nomenclature as in their study. First we calculate the rock's porosity by comparing attenuation coefficients of a dry core with one that is fully saturated with liquid:

$$\phi = \frac{CT_{cw} - CT_{cd}}{CT_w - CT_a} \tag{6.6}$$

where CT_{cw} is the CT number for the rock at a matrix location that is fully saturated with liquid. CT_{cd} is the CT number for a dry core at a matrix location, and CT_w is the CT number for the liquid (water). Since we do not use any salinity in the liquid solution, CT_w is close to 0 for this study. CT_a is the CT number for air, which is about -1000.

For two-phase, gas-liquid systems, the liquid saturation inside the core can be calculated as follows.

$$S_w = \frac{CT_{aw} - CT_{cd}}{CT_{cw} - CT_{cd}} \tag{6.7}$$

where CT_{aw} is the CT number for the core saturated with both liquid and gas. This is the CT number we obtain from the scans that are taken during the foam flooding experiments.

Figure 6.13a shows a vertical scan through the core. This scan clearly shows multiple distinct vugs that are several mm in size (for reference, the core is 17 cm in length and 4 cm in diameter). These vugs appear as black spots on the scan, because of their lower attenuation coefficient. The resulting porosity map for the core is shown in **Figures 6.13b** and **c**. We show the porosity map twice, because the vugs have porosity equal to 1. Therefore, these dominate the porosity map and it is hard to distinguish details in the regions with lower porosity. Therefore, we plot the figure again with the color axis clipped so every porosity value higher than 0.3 is shown as full scale.

We measured the both liquid permeability and porosity of this rock in similar fashion to the previous set of experiments and find that on average the permeability is around 0.5 mD and the porosity is 0.2. The foam floods in this experiment are all carried out using a very high foam quality of $f_g = 0.99$ and total superficial velocity of $5.31 \cdot 10^{-7}$ m/s. This quality was chosen because the low permeability (0.5 mD) means that large pressure gradients are expected. Also, the absence of salts in the surfactant solution and carrying out the experiment at ambient temperature means that a fairly strong foam can be generated leading to even higher pressure gradients. Since we only aim to visualize the

<center>(a)   (b)   (c)</center>
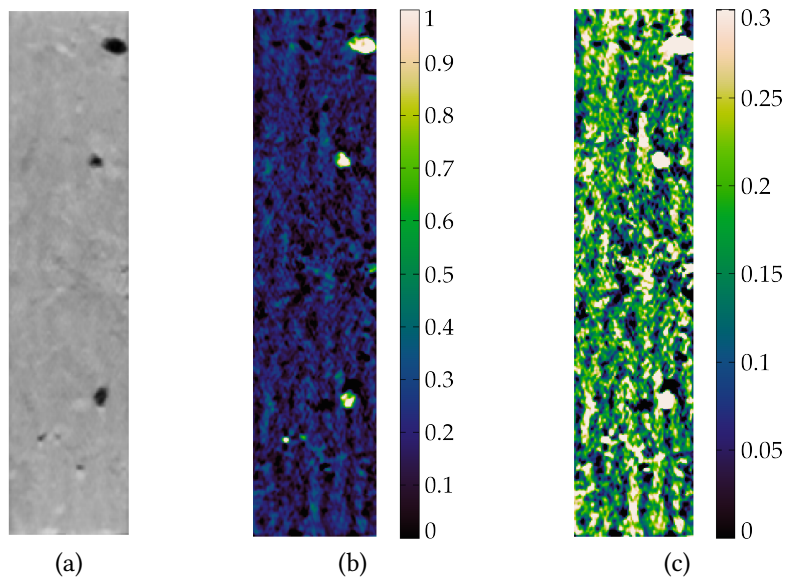
Figure 6.13: (a) CT scan of Edwards White core, showing several vugs several mm in size, (b) Porosity ϕ shown with a range of 0 to 1 indicating high porosity in the vugs, (c) Porosity ϕ shown with a range of 0 to 0.3 indicating other heterogeneities are present besides the vugs

influence of heterogeneities, this limitation of the foam quality is reasonable. Pressure-gradient results from this experiment are shown in **Figure 6.14**. We applied this relatively low superficial velocity in order to maintain a pressure drop over the core within the range of the transducer and also to avoid damaging the core. As can be seen from the graph, the maximum observed pressure gradient is roughly 18 MPa/m, which for a 17 cm core equates to a 30 bar pressure drop. This also means that there is some ambiguity in the terms Pore Volume (PV) and foam quality, because these are defined with respect to the 100 bar back pressure.
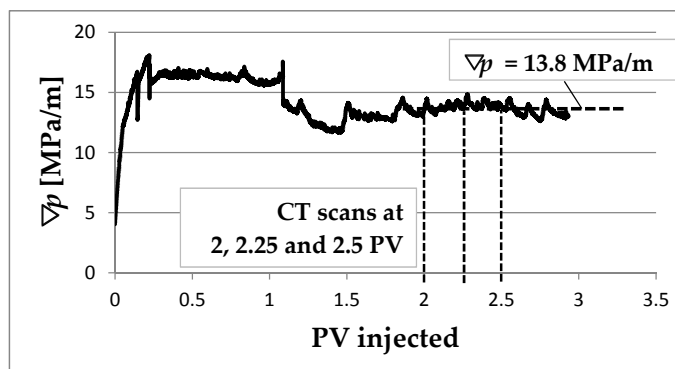
Figure 6.14: Pressure gradient over the entire Edwards White core in the CT visualization experiment ($u_t = 5.31 \cdot 10^{-7}$ m/s, $f_g = 0.99$).

The figure also shows that, at least in terms of pressure gradient, a steady state is achieved in this core. There are still some observable pressure fluctuations after 2 PV of fluids has been injected, but these fluctuations are not significantly larger than those found in previous experiments using the more homogeneous Indiana Limestone cores. This implies that the rock heterogeneities, such as the vugs, do not cause large fluctuations in the pressure response on a macro-scale. The resulting steady-state pressure gradient is approximately 13.8 MPa/m. Under these conditions, this is equivalent to a mobility reduction factor (*MRF*) of around 12.8 compared to the mobility of water. So even at very high foam quality it is still possible to generate fairly strong foam in this rock. The observed mobility reduction factor is also significantly higher than that in the previous set of experiments using the Indiana Limestone cores even though those were performed in higher-permeability rock. This means that the salinity and the elevated temperature used in that experiment have a severe impact on the foaming performance. As mentioned, the experiment was limited to very high foam quality. An attempt was done to carry out measurements at lower foam quality ($f_g = 0.8$), but the generated foam was too strong. Even when we lowered the flow rate further down to the minimum value of the equipment, still the resulting pressure gradients exceeded the transducer range and thus this experiment was terminated.

CT SCANS DURING EXPERIMENT   In total, five CT scans were made of the core during the foam flooding experiment using $f_g = 0.99$. All of the scans were taken with the core at steady state in terms of pressure gradient. The first three CT scans were respectively taken, as indicated in Figure 6.14, after 2, 2.25 and 2.5 PV of fluid injection. After these three scans, we tried using a different foam quality, the aforementioned experiment with $f_g = 0.8$ which was terminated due to excessive pressure build-up. Afterwards the high-foam-quality experiment using $f_g = 0.99$ was resumed and two more scans were taken once steady state had been reached once more. The latter two scans were taken to determine the reproducibility of the results.

By combining the CT results during the experiment with scans of a dry core and a core fully saturated with surfactant solution we can convert the resulting scans in liquid saturation maps using Eq. (6.7). We analyze the results in three different ways. First we look at the average liquid saturation at every vertical position inside the core. That is, we take the arithmetic average of every horizontal line of saturation voxels and use the result as a measure of the variation in saturation throughout the core. Next, we look at the complete, non-averaged, data to see how the heterogeneities affect the saturations in the foam on the core scale. Finally, we focus on the saturations in the vugs and

see how the fluids are distributed there and how this distribution changes with time.

The resulting average saturation profiles as a function of the height of the core from this experiment are shown in **Figures 6.15a** and **b**. The former shows just the saturation profile from the first scan (at 2 PV injected). This shows a relatively constant saturation of $S_w = 0.37$ throughout the core, although there are some minor fluctuations from this number. The only place where the liquid saturation changes drastically is towards the outlet of the core. This is caused by the capillary end effect which causes liquid hold-up towards the core's outlet. The fluctuations in the saturation that are observed also do no coincide with the axial location of the vugs: thus at a core scale the vugs do not seem to have a great effect on the average saturation. Figure 6.15b shows the combined average saturation profile from all the CT scans. This shows there is only minor variation in the saturation in time, indicating that a steady state is reached and is not affected greatly by the heterogeneities in the rock.
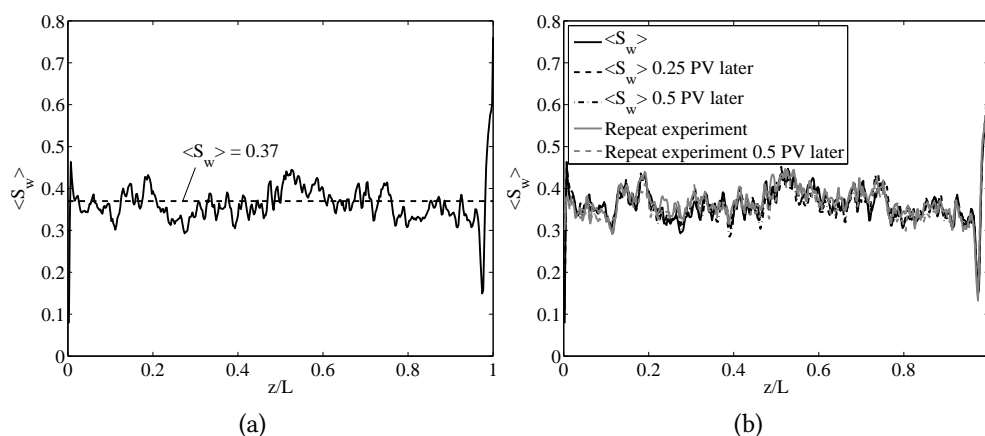
Figure 6.15: Average saturation taken at every vertical position throughout the core after the system reached steady state at: (a) $t = 2$ PV, (b) multiple points in time after state (a).

Based on the average saturation profiles, we might conclude that the rock heterogeneities have no effect on the saturation inside the core since the resulting average all appear to be constant throughout the core and also steady in time. However, a look at the complete non-averaged CT scans, as shown in **Figures 6.16a** through **e**, shows that on the core scale large variations in saturation are found. These figures show the five complete, non-averaged, saturation profiles. These are the profiles used as input data in the average profiles discussed above. These non-averaged profiles show fairly dramatic fluctuations in saturation. Especially in the middle of the core ($z/l \approx 0.5$) drastic changes from very high- to very low-liquid saturation are found. This is found for all

five of the scans, implying that the heterogeneities in the core affect the foam. It is possible that there is layering in the core in the flow direction which could cause differences in saturation as foam in one layer would reduce the mobility more than in others. Broad features are consistent among the scans, but there is also substantial fluctuation in saturation on the fine scale from image to image. This suggests either scatter in the CT images or fluctuation in saturation on the fine scale. The core needs to be analyzed in greater detail to fully explain these large fluctuations in saturation.

(a)   (b)   (c)   (d)   (e)
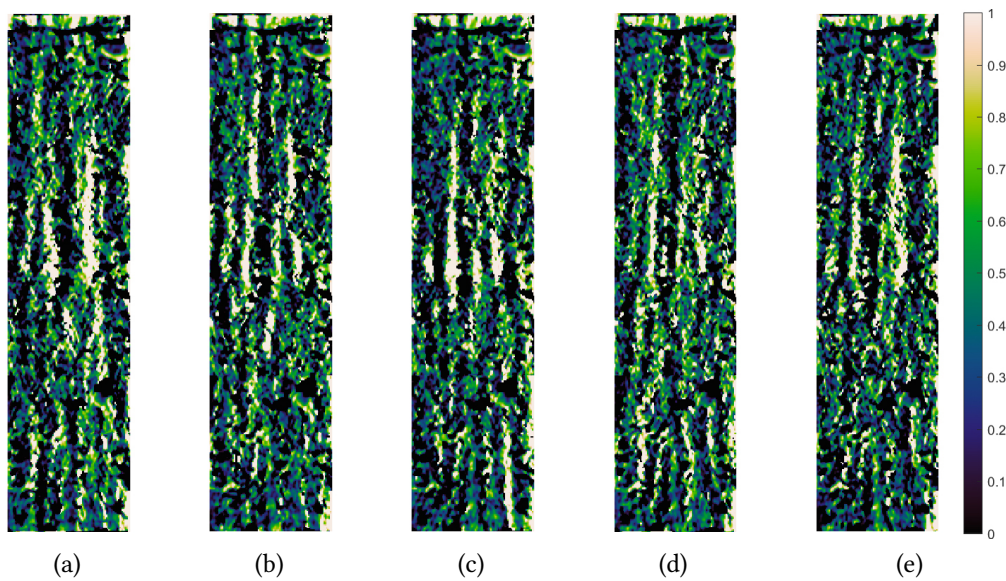
Figure 6.16: Liquid saturation (S_w) throughout the core taken at different points in time for experiment with $f_g = 0.99$. Scan (a) was taken when steady state was reached (at 2 PV injected). Scan (b) and (c) were respectively taken 0.25 PV and 0.5 PV later. Scan (d) was taken after steady state had been reached in the repeat experiment. Scan (e) was taken 0.5 PV after scan (d). Data were not averaged in any way.

Finally we focus on the flow behaviour inside the vugs. As shown in the scan of the dry core (Figure 6.13a), there are three large vugs, several mm in size along the right-hand side of Figures 6.13a and b. **Figures 6.17a** to **c** show the saturation profiles in the vugs indicated on the leftmost figure. The second figure from the left shows a detailed view of the given vug. The second figure from the right shows the saturation profile in the vug from the first scan that is taken and the rightmost figure shows the result of the last scan. The resulting saturation profile remains constant through time for each of the vugs indicating that a steady state is reached. We find that two regions can be distinguished within each vug: one filled with liquid and the other filled with gas. The latter is located slightly above the liquid region. There is a clear interface

separating the two regions which remains stable through time (that is, it is in the same location in the last scan as in the first). This means that there is no foam inside the vugs, but the effect of the vugs appears to be limited to the vugs itself. Directly outside the vugs we can already see changes in saturation (green colors in the saturation profiles) which implies foam is present there.

(a)

(b)

(c)
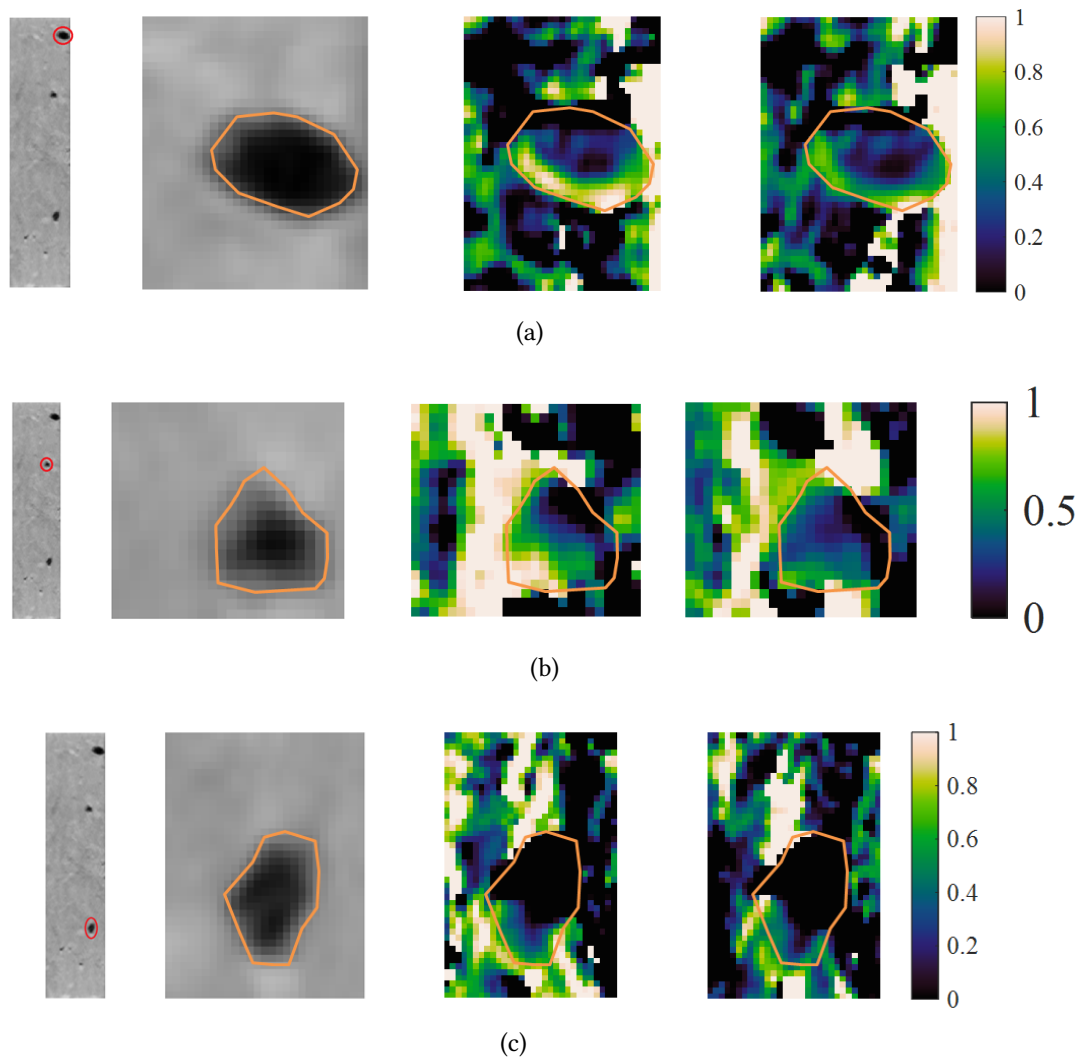
Figure 6.17: Liquid saturation (S_w) inside the three major vugs. Left figure of dry core indicates the vug of which the saturation profile is shown. Second figure from the left shows detailed view of the vug. Second figure from the right shows profile from the first scan that is taken. Rightmost figure shows the profile of the last scan that is taken. Profiles show separate regions for liquid (white color in the profile) and gas (black) in the vugs with gas being on top of the liquid. The interface between the two phases remains at roughly the same location throughout the experiment.

6.4 CONCLUSIONS

The long-core experiments show that foam EOR is possible in low-permeability carbonate rocks. However, foam strength is considerably smaller compared to previous experiments we conducted in high-permeability unconsolidated bead-packs. This finding agrees with previous studies (e.g. Khatib et al. (1988)) who found reduced foam strength in low-permeability rocks. The two different surfactants we tested here show similar foam strength, but the experiment with the AES surfactant shows indications of multiple steady states at very high foam qualities. As a result of this, our fitting approach to determine whether this surfactant is suitable for a SAG foam application cannot be applied accurately to that case, because we do not know where to place the shock on the fractional flow curve. For the experiment using the APG experiment we did not find these multiple steady states during the experiments so for this experiment we can use our fitting approach. We find that at the leading edge of a foam front in a gas-injection cycle of a SAG process, this foam is just about able to maintain mobility control over the displaced phase. It is comparable to the 'weak foam' formulation discussed in Chapter 5. When crude oil is added to the injection process, the foam strength is reduced. In our experiments we found that the resulting steady-state pressure gradient is roughly halved in the presence of oil. Also we observed that the fluids at the outlet appear more like an emulsion than a foam. Still, some mobility reduction can be achieved with crude oil added to the injection process.

CT visualization experiments in heterogeneous, vuggy rocks show that foaming is also possible in these rocks. Based on average saturation profiles we conclude that the influence of vugs is limited. Saturation is fairly uniform throughout the core indicating that there is foam present. The detailed, non-averaged saturation profiles of the entire core show more-chaotic behaviour than the average values. At steady state, regions of high and low liquid saturation are present very close to each other. This might be the result of layering in the heterogeneous core. The core needs to be analysed in greater detail (e.g. through μCT imaging) to verify this conclusion. The influence of the vugs does not prevent the generation of foam on the core scale. We find that there are two distinct regions inside the vugs, one filled with gas and one with liquid.

7

CONCLUSIONS AND RECOMMENDATIONS

The work described in this thesis explores various aspects of foam enhanced oil recovery and is especially focused towards the use of foam in carbonate formations. To this end, several topics are discussed, from surfactant screening to designing parameter-fitting approaches, modeling SAG injection processes and ultimately performing experiments in consolidated carbonate cores. Here we present the major conclusions from this work and give some recommendations for further study of this topic.

7.1 CONCLUSIONS

7.1.1 *A Methodology for Screening Surfactants for Foam Enhanced Oil Recovery in an Oil-Wet Reservoir*

A necessary first step towards a successful foam EOR project is finding a foaming surfactant appropriate for use under harsh operating conditions. Here, we introduce a screening methodology for foaming surfactants that can be used both to quickly screen large numbers of surfactants through bulk-foam tests and also provide quantitative foaming performance data through foam flooding tests. The methodology takes into account the effect of oil, salinity and wettability of the porous medium. The main conclusions from our screening methodology are as follows:

1. Salinity is a major concern when evaluating surfactants. In this study, 26 of 31 surfactants analysed precipitated at the highest salinity levels tested (200,000 ppm).

2. As expected, presence of crude oil was detrimental to foaming performance in bulk for most surfactants. In water-wet porous media, the mobility reduction factor also decreased significantly with oil injected. However, some surfactants still produced fairly strong foams with oil present. For the oil-wet medium we did not find a general trend of reduced foam

strength in the presence of crude oil. In fact, in some experiments mobility was reduced more when oil was injected along with the other fluids.

3. Foaming performance in water-wet porous media correlated well with bulk-foam testing at the same temperature: we found that surfactants that showed decent foaming potential in bulk also led to significant mobility reduction factors in the water-wet bead pack. This correlation is not as strong for the oil-wet pack.

4. Wettability (or hydrophilicity of the bead surface) plays a major role in foaming performance. In general, foam strength tends to be significantly lower in oil-wet porous media compared to water-wet packs. Also, surfactant performance in oil-wet porous media does not correlate with that in water-wet media. The best performing surfactant in the water-wet pack was not the same as the best performer in the oil-wet pack. This can also explain the discrepancy in results found in literature, about correlating bulk-foaming performance with that in porous media, where porous media tests were carried out using oil-wet media. The influence of crude oil was much more limited for the oil-wet pack compared to the water-wet one; that is, *MRF* is not reduced as drastically by the presence of oil in the oil-wet pack as in the water-wet pack.

5. Overall, surfactants 2 and 6 proved to be the best-performing surfactants from these tests, with high salinity tolerance and good foam strength in water-wet and oil-wet porous media. Therefore these surfactants were recommended for use in further testing in consolidated cores.

7.1.2   *Fitting Foam Simulation Model Parameters to Data I: Co-Injection of Gas and Liquid*

Design of effective foam projects requires accurate simulation of foam behavior in the formation. We present a method for fitting parameters in the STARS foam model (excluding the effect of oil) to data for pressure gradient ∇p (or, equivalently, resistance factor RF or apparent viscosity μ_{app}) as a function of foam quality at a single superficial velocity. The approach estimates the non-Newtonian behavior in the low-quality regime from the same set of data. The same method would apply to the parameters of the foam model in ECLIPSE, and a similar method to those in UTCHEM. Its advantages are simplicity and directness. The model fit would be appropriate for an EOR process involving foam injection at finite water fraction, but not a SAG foam process involving large slugs of gas and liquid. For the latter process, model parameters should be fit to data relevant to that process, i.e. at extremely high foam quality.

This approach assumes an abrupt transition between high- and low-quality foam regimes, i.e. a large value of *epdry*. The parameter values quickly obtained by this method can provide the initial guess for a computer-based least-squares fit of all parameters, including a smaller value of *epdry*, and a check on the parameters so obtained.

7.1.3 *Fitting Foam Simulation Model Parameters to Data II: SAG Foam Applications*

Others have shown that the fractional-flow curve is the key to predicting the performance of a SAG foam process during gas injection (e.g., Shan and Rossen (2004)). Here we show how to use the fractional-flow plot to fit foam model parameters to steady-state foam coreflood data and thereby predict the SAG displacement that is implied by these data. For reasons discussed in the text we believe steady-state data to be more reliable for model fitting than a single dynamic SAG coreflood. For illustration we use the STARS local-equilibrium foam model here, but the same approach could be used with other foam models. During the period of gas injection, the success of a SAG foam process hinges on the properties of foam at the point of tangency that defines the leading edge of the gas bank. Correctly fitting the $f_w(S_w)$ data from the corefloods implies a correct fit both to the velocity and the mobility of the foam bank.

Accurate measurements of water saturation in the experiment, or, failing that, a reliable water relative-permeability function $k_{rw}(S_w)$, is key to upscaling the data to a SAG flood, as noted previously by Ashoori and Rossen (2012). For the data of Ma et al. (2013), using S_w values inferred from measured mobilities and a plausible $k_{rw}(S_w)$ function instead of the directly measured S_w values results in a factor-of-two difference in the predicted mobility at the leading edge of the foam bank during gas injection in a SAG process.

A SAG process involving multiple slugs depends not only on foam behavior at low water fractional flow but, further from the well, on behavior at larger water fractional flow. The examples presented here indicate the challenge in obtaining a fit to both ranges of data. Compromises must be made between fitting all the saturation, mobility, and fractional-flow data. It may be that a new functional form is needed for the effect of capillary pressure and water saturation on foam that could better fit the whole range of data.

We do not compute gas injectivity in the cases shown because nearly the entire foam bank is predicted to lie beyond the range of the data - that is, starting with the shock near the lowest-f_w value and decreasing in f_w from there. The fact that in the STARS dry-out model foam does not collapse even at S_{wr} does have an important effect on predicted injectivity, however. For the fit to

the Persoff et al. (1991) data mobility at the well is about 20 times less than that expected if foam collapses at S_{wc}, and for the fits to the data of Ma et al. (2013) mobility at the well is between 1000 and 1500 times less than expected. Injectivity calculated with the model would be exceedingly poor.

One advantage of the method presented here, of fitting $f_w(S_w)$ data directly for SAG processes, is that it immediately shows whether the form of the model itself is inappropriate for SAG. A simple spreadsheet can instantly show the fit to $f_w(S_w)$ data for any parameter set. Thus, it is easy to judge the best value of *fmmob* for a given value of *epdry* and then vary *epdry* in the search for the best fit to all the data.

7.1.4   *Modeling Foam Flow in Radial SAG Injection*

We propose a simple model for modeling the flow of foam during the gas-injection cycle of a SAG process. Here we explore two different cases, one where the injected foam is much less mobile throughout the foam bank than the fluids ahead of foam ("strong foam" case) and one where the foam is just able to maintain mobility control with the fluids ahead of it ("weak foam" case). We check the proposed model by comparing its result to those from two-dimensional numerical simulations using the STARS simulator. Our conclusions are as follows:

1. For a single-slug SAG process, the pressure difference across the foam bank during gas injection is nearly constant in time, if foam collapses or substantially weakens near the injection well.

2. For the "strong foam" case, the injection rate required to maintain injection pressure constant is also nearly constant, at least during the period of radial flow around the injection well. The injection rate of gas is relatively small, however.

3. For the "weak foam" case, the injection rate must increase with time to maintain injection pressure at its optimal value. Such a process accelerates oil production, but the gas supply and production facilities must be prepared for increasing injection and production rates.

4. Simulations of a five-spot pattern agree reasonably well with the model based on radial flow. For a foam much less mobile than the fluids initially in the reservoir, the injection rate is nearly constant for the period where foam has swept from about 5% to over 95% of the pattern. For a weaker foam, just a bit less mobile than the fluids ahead of it, injec-

tion rate increases with time. The weaker foam also produces an uneven displacement front and earlier gas breakthrough.

5. Observed differences between the radial-flow model and quarter-five-spot simulations can, in part, be explained from the more complex geometry in the latter pattern. This pattern comprises both radial outflow and inflow parts. The inflow part, where the water flow converges towards the production well, introduces an additional pressure drop compared to the simple model, which only accounts for radial outflow from the injection well. A better fit to the STARS simulations is found when incorporating the additional term in the expression for the pressure drop.

6. One can derive the implications for injectivity directly from the fractional-flow curve for foam using Eq. (5.10), at least in a region around the well where mobile oil is not present, and as long as the fractional-flow function accounts for the presence of immobile oil at the given saturation. One could use this approach to guide selection of a foaming agent, based on the available gas stream for a given project and the flexibility of the injection and production facilities.

7. One can also relate foam parameters obtained in the laboratory to the idealized SAG foam model of de Velde Harsenhorst et al. (2014), which predicts behavior similar to that shown in simulations with more complex models. The foam-front propagation rates obtained using the idealized model is similar to that found in the STARS simulations. Observed differences with our simulations can be attributed in part to the effects of compressibility and underestimation of the total mobility at the well in the simulations, which are an effect of the discretization of the domain in the simulation.

7.1.5   *Foam Flooding in Carbonate Rocks*

Carbonate formations pose specific challenges to foam EOR through their low-permeability and heterogeneous nature. We carried out a series of experiments to determine whether foam is a suitable method of mobility control in these rocks. Specifically, we check if the generated foam in our experiment can be used in a SAG injection process. Also we check how heterogeneities affect the foaming performance through a CT visualization experiment using a heterogeneous Edwards White core. The main conclusions derived from this study are as follows:

The long-core experiments, carried out in Indiana Limestone cores, show that foam EOR in low-permeability carbonate rocks is possible. However, the

observed foam strength is considerably less than that in previous experiments we conducted in high-permeability unconsolidated bead-packs. This finding agrees with previous studies (e.g. Khatib et al. (1988)) who found reduced foam strength in low-permeability rocks. The two different surfactants we tested here show similar foam strength, but the experiment with the AES surfactant shows indications of multiple steady states at very high foam qualities. As a result of this, our fitting approach to determine whether this surfactant is suitable for a SAG foam application cannot be applied accurately here, because we do not know where to draw the shock front on the fractional-flow curve. For the experiment using the APG surfactant we did not find these multiple steady states occurring during the experiments, so for this experiment we can use our fitting approach. We find that at the leading edge of a foam front in a gas-injection cycle of a SAG process, this foam is just about able to maintain mobility control over the displaced phase. It is comparable to the 'weak foam' formulation that we discussed in Chapter 5. When crude oil is added to the injection process, the foam strength is reduced. In our experiments the resulting steady-state pressure gradient is roughly halved in the presence of oil. Also we observed that the fluids at the outlet appear more like an emulsion than a foam. Still, some mobility reduction can be achieved with crude oil added to the injection process.

CT visualization experiments in heterogeneous, vuggy rocks show that foaming is also possible in these rocks. Based on average saturation profiles we conclude that the influence of the relatively small, discontinuous vugs in these cores is limited. Cross-section-average saturation is fairly constant along the core. The detailed non-averaged saturation profiles of the entire core show more chaotic behaviour than the average values. At steady state, regions of high and low liquid saturation are present very close to each other. This might be the result of layering in the heterogeneous core where in high-permeability layers the foam would reduce the mobility more than in other layers. The latter conclusion is fairly speculative and the core needs to be analysed in greater detail (e.g. through μCT imaging) to verify this conclusion. The influence of the vugs is limited to the immediate vicinity of the vugs and does not prevent the generation of foam on the core scale. We find that there are two distinct regions inside the vugs, one filled with gas and one with liquid.

7.2   RECOMMENDATIONS

This study constitutes a step towards the implementation of foam as an EOR method in carbonate formations. Before a field trial can commence there are

still several research topics which require further study. These topics include the following:

- The effect of oil on foam stability needs to be examined further. Our long-core tests provide only basic information on the influence of oil: that is, the effect of a specific crude oil on the stability of the foam. Further study is needed to shed light on the effect of different oil-related parameters, such as the oil's composition and saturation.

- The numerical simulations performed in this study are done using a commercial simulator, CMG STARS. Its source code is closed; hence not all of the inner workings of the simulator are known. Simulations using an open-source simulator can be used to verify the results from the STARS simulator.

- Our CT experiments in heterogeneous rocks are inconclusive: the influence of vugs and other heterogeneities still need further study. The resulting saturation profiles for this rock look very heterogeneous in terms of saturation. Pore-network visualization, using, e.g. µCT imaging techniques, are necessary to determine what causes these erratic saturation profiles.

- The parameter-fitting approach outlined here is a good start, but not a least-squares fit. Implementation of least-squares fit might improve the fit somewhat, but care needs to be taken not to neglect the physics of the system. A least squares fit is likely to have multiple solutions, so it is necessary to determine which is the correct one, for which the method outlined here is a necessary start.

- Adsorption is a major issue in selecting an appropriate surfactant. Here we finally selected a non-ionic and an anionic surfactant for testing in long cores. The latter may suffer from worse adsorption in a carbonate formation, due to the zeta potential of the calcite surface. This is somewhat speculative as active clays may influence the overall surface charge of the rock. Therefore, adsorption measurements required to determine which surfactants suffer greatest adsorption in the utilised rock.

A

SURFACTANT SCREENING DATA
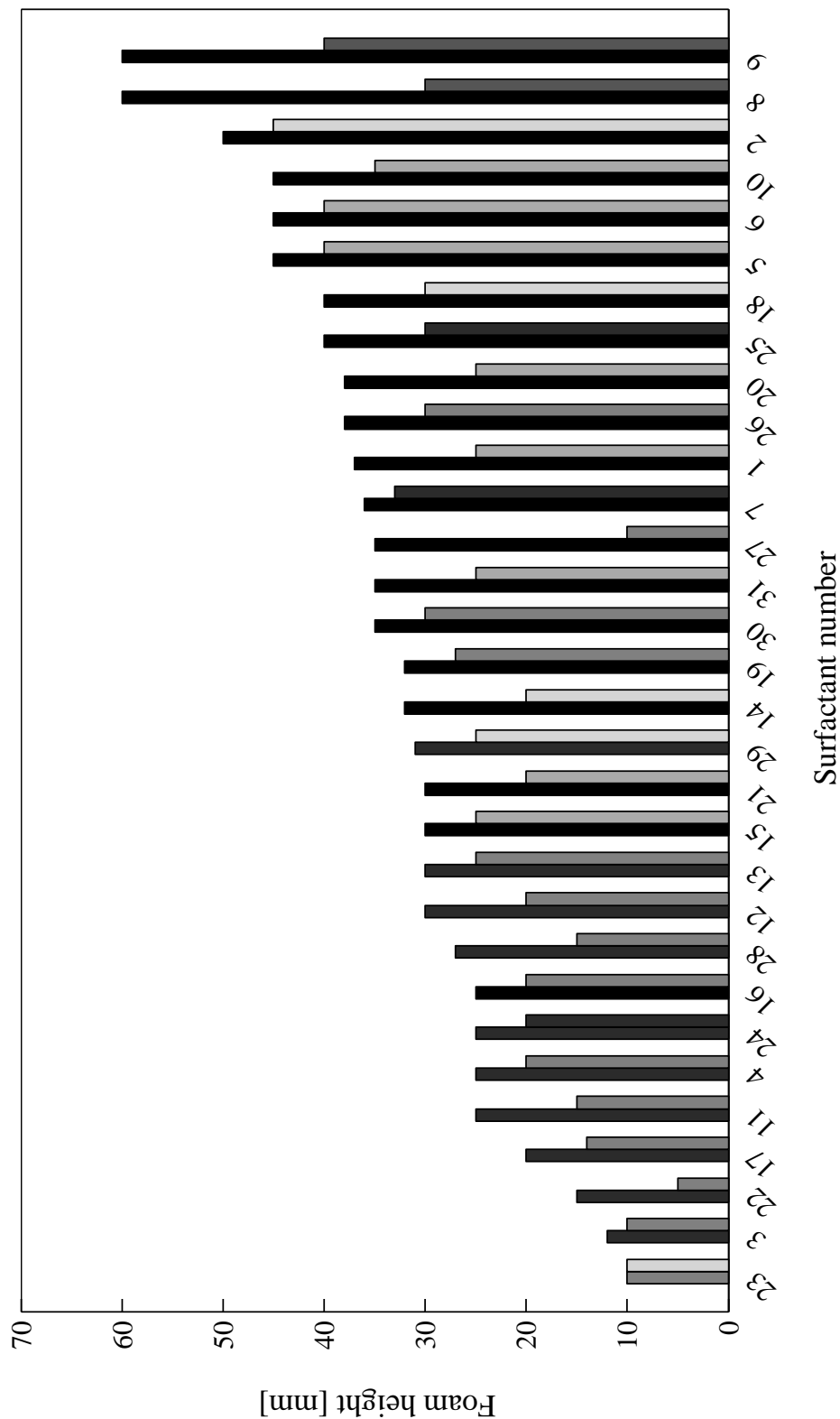
Figure A.1: Foam heights for all surfactants. No oil is present during these tests; salinity = 70,000 ppm. For each surfactant, the left column indicates the initial foam height; the right column indicates the foam height after 10 minutes. Shade of grey indicates foam texture: ▢ = coarse foam, ▨ = medium to coarse foam, ▨ = medium foam, ▨ = medium to fine foam, ▨ = fine foam, ■ = very fine foam
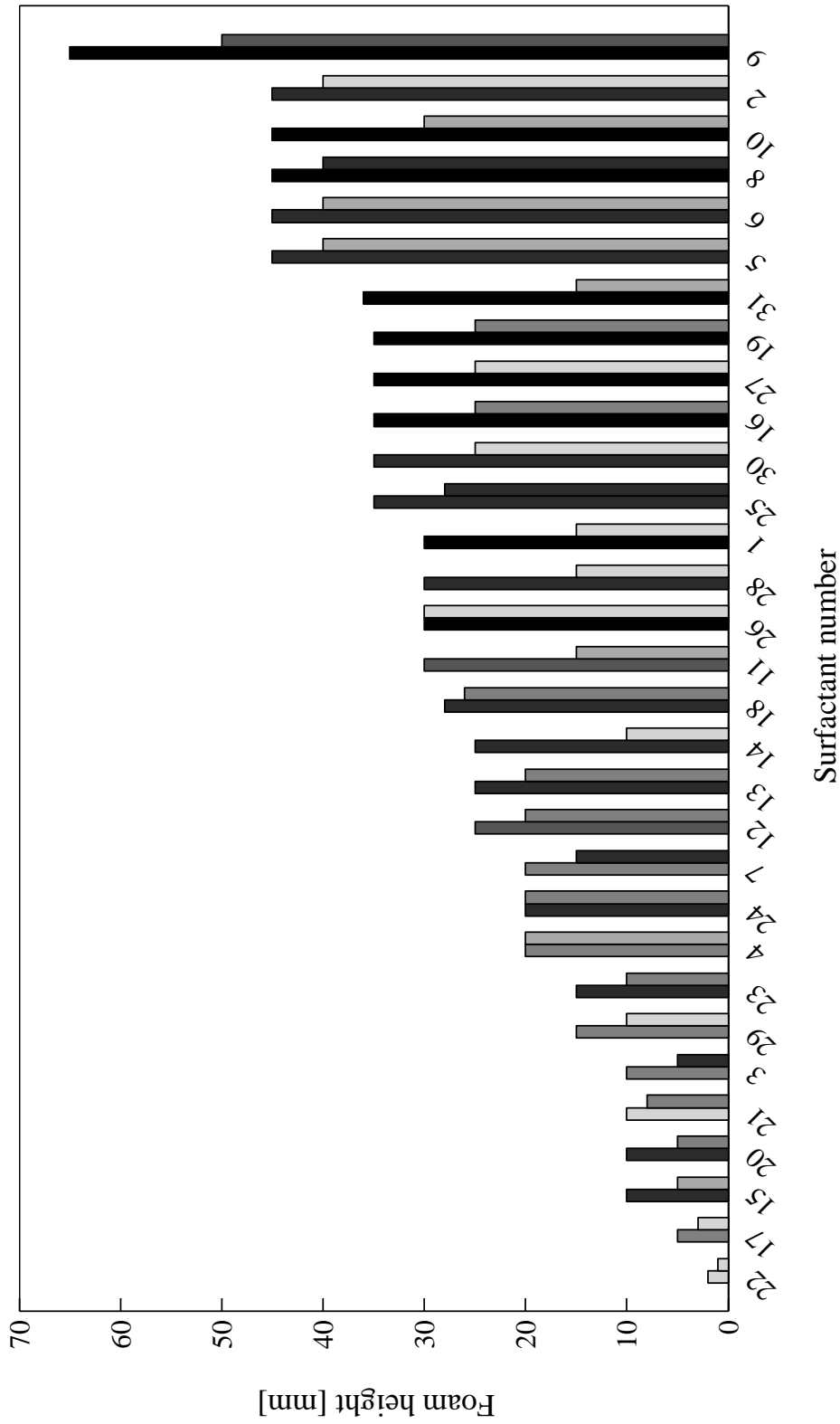
Figure A.2: Foam heights for all surfactants. No oil is present during these tests; salinity = 120,000 ppm. For each surfactant, the left column indicates the initial foam height; the right column indicates the foam height after 10 minutes. Shade of grey indicates foam texture: ▪ = coarse foam, ▪ = medium to coarse foam, ▪ = medium foam, ▪ = medium to fine foam, ▪ = fine foam, ▪ = very fine foam
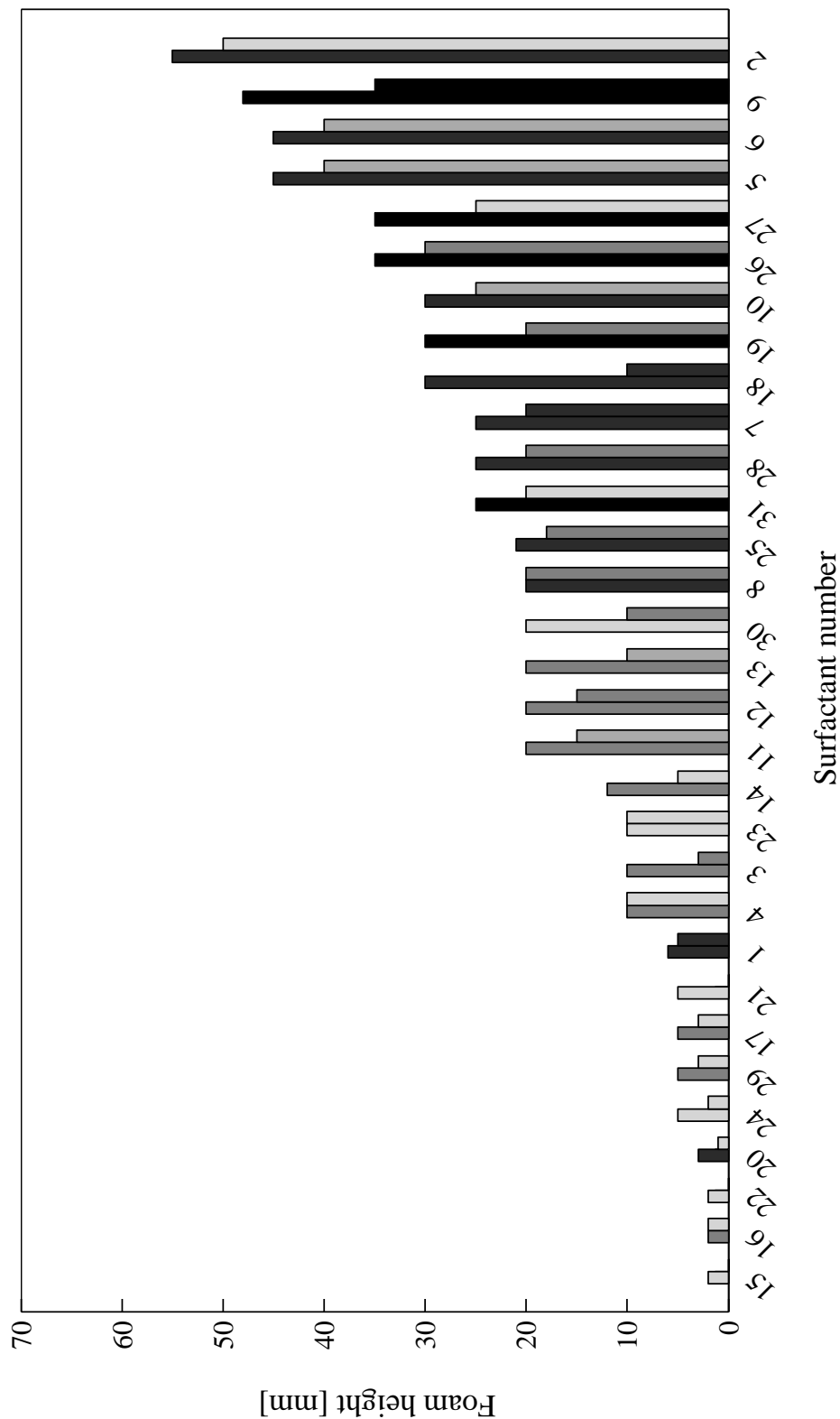
Figure A.3: Foam heights for all surfactants. No oil is present during these tests; salinity = 200,000 ppm. For each surfactant, the left column indicates the initial foam height; the right column indicates the foam height after 10 minutes. Shade of grey indicates foam texture: ▨ = coarse foam, ▨ = medium to coarse foam, ▨ = medium foam, ▨ = medium to fine foam, ▨ = fine foam, ■ = very fine foam
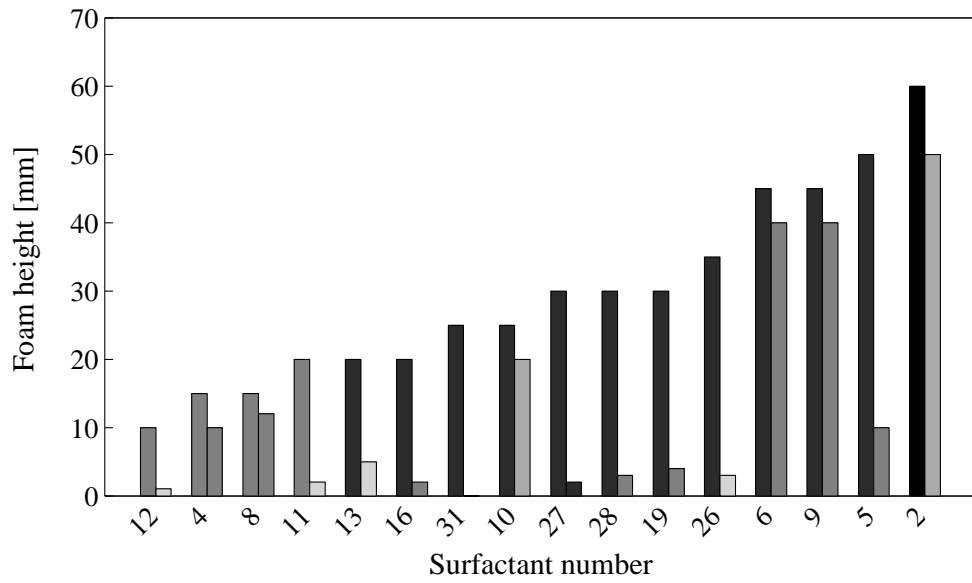
Figure A.4: Foam heights for all surfactants in the presence of oil; salinity = 70,000 ppm. For each surfactant, the left column indicates the initial foam height; the right column indicates the foam height after 10 minutes. Shade of grey indicates foam texture: ▢ = coarse foam, ▨ = medium to coarse foam, ▨ = medium foam, ▨ = medium to fine foam, ■ = fine foam, ■ = very fine foam
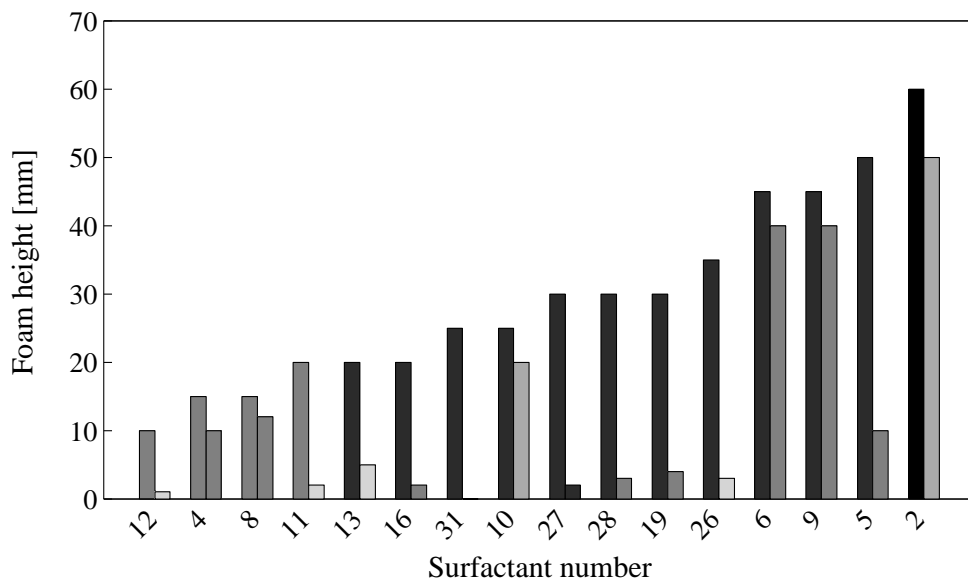
Figure A.5: Foam heights for all surfactants in the presence of oil; salinity = 120,000 ppm. For each surfactant, the left column indicates the initial foam height; the right column indicates the foam height after 10 minutes. Shade of grey indicates foam texture: ▢ = coarse foam, ▨ = medium to coarse foam, ▧ = medium foam, ▩ = medium to fine foam, ▪ = fine foam, ■ = very fine foam
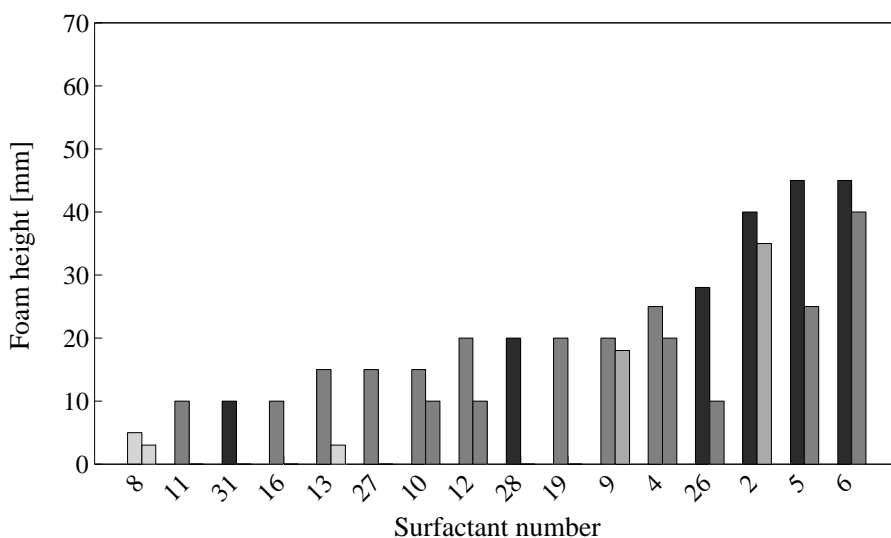
Figure A.6: Foam heights for all surfactants in the presence of oil; salinity = 200,000 ppm. For each surfactant, the left column indicates the initial foam height; the right column indicates the foam height after 10 minutes. Shade of grey indicates foam texture: ▢ = coarse foam, ▨ = medium to coarse foam, ▧ = medium foam, ▩ = medium to fine foam, ▪ = fine foam, ■ = very fine foam

Table A.1: Assessment of surfactant performance in test tubes at a salinity of 70,000 ppm. No oil is present in the test tubes during these experiments. In the precipitation column, * indicates that these surfactants showed considerably more precipitation compared to other surfactants. Foam texture indication: VF - very fine, F- fine M - medium, C - coarse, XX - no foam.

SURFACTANT NUMBER	PRECIPITATION (PASS (V) OR FAIL (X))	INITIAL FOAM HEIGHT [MM] AND TEXTURE	FOAM HEIGHT [MM] AND TEXTURE AFTER 10 MINUTES
1	V	37, VF	25, M-C
2	V	50, VF	45, C
3	X, flakes*	12, F	10, M
4	X, flakes	25, F	20, M
5	X, slight	45, VF	40, M-C
6	V	45, VF	40, M-C
7	V	36, VF	33, F
8	V	60, VF	30, M-F
9	V	60, VF	40, M-F
10	V	45, VF	35, M-C
11	V	25, F	15, M
12	V	30, F	20, M
13	X, flakes	30, F	25, M
14	V	32, VF	20, C
15	X, layer	30, VF	25, M-C
16	V	25, VF	20, M
17	X, layer	20, F	14, M
18	V	40, VF	30, C
19	V	32, VF	27, M
20	X, layer	38, VF	25, M-C
21	V	30, VF	20, M-C
22	X, layer	15, F	5, M
23	X, suspension*	10, M	10, C
24	X, slight	25, F	20, F
25	X, slight	40, VF	30, F
26	V	38, VF	30, M
27	X, flakes	35, VF	10, M
28	V	27, F	15, M
29	X, layer	31, F	25, C
30	V	35, VF	30, M
31	V	35, VF	25, M-C

Table A.2: Assessment of surfactant performance in test tubes at a salinity of 120,000 ppm. No oil is present in the test tubes during these experiments. In the precipitation column, * indicates that these surfactants showed considerably more precipitation compared to other surfactants. Foam texture indication: VF - very fine, F- fine M - medium, C - coarse, XX - no foam.

SURFACTANT NUMBER	PRECIPITATION (PASS (V) OR FAIL (X))	INITIAL FOAM HEIGHT [MM] AND TEXTURE	FOAM HEIGHT [MM] AND TEXTURE AFTER 10 MINUTES
1	X, layer	30, VF	15, C
2	V	45, F	40, C
3	X, flakes*	10, M	5, F
4	X, flakes	20, M	20, M-C
5	X, slight	45, F	40, M-C
6	V	45, F	40, M-C
7	X, layer	20, M	15, F
8	X, layer	45, VF	40, F
9	V	65, VF	50, M-F
10	V	45, VF	30, M-C
11	V	30, M-F	15, M-C
12	V	25, M-F	20, M
13	V	25, F	20, M
14	X, layer	25, F	10, C
15	X, layer	10, F	5, M-C
16	V	35, VF	25, M
17	X, layer	5, M	3, C
18	X, layer	28, F	26, M
19	V	35, VF	25, M
20	X, layer	10, F	5, M
21	X, layer	10, C	8, M
22	X, layer	2, C	1, C
23	X, suspension*	15, F	10, M
24	X, layer	20, F	20, M
25	X, flakes	35, F	28, F
26	X, slight	30, VF	30, C
27	X, flakes	35, VF	25, C
28	X, slight	30, F	15, C
29	X, layer	15, M	10, C
30	X, layer	35, F	25, C
31	V	36, VF	15, M-C

Table A.3: Assessment of surfactant performance in test tubes at a salinity of 200,000 ppm. No oil is present in the test tubes during these experiments. In the precipitation column, * indicates that these surfactants showed considerably more precipitation compared to other surfactants. Foam texture indication: VF - very fine, F- fine M - medium, C - coarse, XX - no foam.

SURFACTANT NUMBER	PRECIPITATION (PASS (V) OR FAIL (X))	INITIAL FOAM HEIGHT [MM] AND TEXTURE	FOAM HEIGHT [MM] AND TEXTURE AFTER 10 MINUTES
1	X, layer	6, F	5, F
2	V	55, F	50, C
3	X, flakes*	10, M	3, M
4	X, layer	10, M	10, C
5	X, slight	45, F	40, M-C
6	V	45, F	40, M-C
7	X, layer	25, F	20, F
8	X, layer	20, F	20, M
9	X, suspension	48, VF	35, VF
10	V	30, F	25, M-C
11	X, layer	20, M	15, M-C
12	V	20, M	15, M
13	X, layer	20, M	10, M-C
14	X, layer	12, M	5, C
15	X, suspension	2, C	0, XX
16	X, layer	2, M	2, C
17	X, layer	5, M	3, C
18	X, layer	30, F	10, F
19	V	30, VF	20, M
20	X, layer	3, F	1, C
21	X, layer	5, C	0, XX
22	X, layer	2, C	0, X
23	X, suspension*	10, C	10, C
24	X, slight	5, C	2, C
25	X, layer	21, F	18, M
26	X, flakes	35, VF	30, M
27	X, flakes	35, VF	25, C
28	X, flakes	25, F	20, M
29	X, layer	5, M	3, C
30	X, layer	20, C	10, M
31	X, layer	25, VF	20, C

Table A.4: Assessment of surfactant performance in test tubes in the presence of oil at a salinity of 70,000 ppm. Foam texture indication: VF - very fine, F - fine, M - moderate, C - coarse, XX - no foam

SURFACTANT NUMBER	PRECIPITATION (PASS (v) OR FAIL (x))	INITIAL FOAM HEIGHT [MM] AND TEXTURE	FOAM HEIGHT [MM] AND TEXTURE AFTER 10 MINUTES
2	V	60, VF	50, M-C
4	V	15, F	15, M
5	V	45, VF	10, M
6	V	45, VF	45, M
8	V	40, F	40, F
9	V	50, F	10, M
10	V	30, F	22, M
11	V	25, F	5, C
12	V	20, M-F	10, C
13	V	20, M-F	5, C
16	V	25, F	5, M
19	V	28, F	5, M
26	V	35, F	5, C
27	V	30, F	5, M
28	V	28, F	5, M
31	V	35, F	3, C

Table A.5: Assessment of surfactant performance in test tubes in the presence of oil at a salinity of 120,000 ppm. Foam texture indication: VF - very fine, F - fine, M - moderate, C - coarse, XX - no foam

SURFACTANT NUMBER	PRECIPITATION (PASS (V) OR FAIL (X))	INITIAL FOAM HEIGHT [MM] AND TEXTURE	FOAM HEIGHT [MM] AND TEXTURE AFTER 10 MINUTES
2	V	60, VF	50, M-C
4	V	15, M	10, M
5	V	50, F	10, M
6	V	45, F	40, M
8	V	15, M	12, M
9	V	45, F	40, M
10	V	25, F	20, M-C
11	V	20, M	2, C
12	V	10, M	1, C
13	V	20, F	5, C
16	V	20, F	2, M
19	V	30, F	4, M
26	V	35, F	3, C
27	V	30, F	2, F
28	V	30, F	3, M
31	V	25, F	0, XX

Table A.6: Assessment of surfactant performance in test tubes in the presence of oil at a salinity of 200,000 ppm. Foam texture indication: VF - very fine, F - fine, M - moderate, C - coarse, XX - no foam

SURFACTANT NUMBER	PRECIPITATION (PASS (v) OR FAIL (x))	INITIAL FOAM HEIGHT [MM] AND TEXTURE	FOAM HEIGHT [MM] AND TEXTURE AFTER 10 MINUTES
2	V	40, F	35, M-C
4	V	25, M	20, M
5	V	45, F	25, M
6	V	45, F	40, M
8	V	5, C	3, C
9	V	20, M	18, M-C
10	V	15, M	10, M
11	V	10, M	0, XX
12	V	20, M	10, M
13	V	15, M	3, C
16	V	10, M	0, XX
19	V	20, M	0, XX
26	V	28, F	10, M
27	V	15, M	0, XX
28	V	20, F	0, XX
31	V	10, F	0, XX

Table A.7: Mobility reduction factor for all of the tested surfactant-salinity combinations in the water-wet bead-pack without crude oil present

SURFACTANT NUMBER	SALINITY ($\times 1000$ PPM)	MRF
2	70	2278
	120	1889
	200	939
6	70	1333
	120	929
	200	741
9	70	1222
	120	1167
10	70	233
	120	121
	200	19
12	70	19
	120	14
	200	13
19	70	26
	120	21
	200	13
26	70	17
31	70	18
	120	17

Table A.8: Mobility reduction factor for all of the tested surfactant-salinity combinations in the water-wet bead-pack in the presence of crude oil

SURFACTANT NUMBER	SALINITY ($\times 1000$ PPM)	MRF (AS IN TABLE A.7)	MRF WITH OIL
2	70	2278	536
	120	1889	952
	200	939	410
6	70	1333	12
	120	929	250
	200	741	267
9	70	1222	833
	120	1167	556
10	70	233	200
	120	121	83
	200	19	22

Table A.9: Mobility reduction factor for all of the tested surfactant-salinity combinations in the oil-wet bead-pack

SURFACTANT NUMBER	SALINITY ($\times 1000$ PPM)	MRF	MRF WITH OIL
2	70	123	175
	120	150	183
	200	33	25
6	70	139	148
	120	68	59
	200	125	146
9	70	122	206
	120	130	81
10	70	6	1
	120	4	1
	200	1	1

B

FOAM MODEL PARAMETERS, RELATIVE-PERMEABILITY
FUNCTIONS AND FLUID PROPERTIES

This Appendix shows the relation between the STARS foam model and similar foam model from other reservoir simulators. The relative-permeability functions and fluid properties used in this study are also given here along with a method of adjusting experimental data for compressibility.

B.1   RELATION OF FOAM PARAMETERS IN OTHER FOAM MODELS TO THOSE IN STARS

Table B.1 lists the STARS foam model parameters used in this study and the corresponding parameters in the foam models in ECLIPSE (Schlumberger (2010)) and UTCHEM (Cheng et al. (2000)). The parameter names listed here for ECLIPSE and UTCHEM are not necessarily the variable names in the code, but rather names defined in the simulators' reference manuals (or, for UTCHEM, in Cheng et al. (2000)). Also note that the UTCHEM model has some differences with the STARS model (e.g., shear-thinning rheology is based on gas superficial velocity rather than capillary number).

Note that in some cases the simulators use symbols with conventional definitions different from those in the reference manual. In particular, in the ECLIPSE foam model f_w is not water fractional flow but a parameter like *epdry*, and

Table B.1: Foam model parameter terminology in three different reservoir simulators

STARS	ECLIPSE	UTCHEM
fmmob	M_r	R
epdry	f_w	ε
fmdry	S_w^l	S_w^*
fmcap	N_c^r	u_g
epcap	e_c	σ

in UTCHEM σ is not surface tension but a power-law parameter for shear-thinning foam.

The ECLIPSE foam model is substantially similar to that in STARS in how it handles the two effects that are the focus of this study. UTCHEM differs in some ways. Instead of Eq. (3.3) UTCHEM interpolates the mobility-reduction factor between R (its value in the low-quality regime) and 1 over an interval $(S_w^* \pm \varepsilon)$. Thus a small value of ε corresponds to a large value of *epdry* in STARS. The differences between these methods of interpolation of mobility reduction as a function of S_w have a major impact on the modeling of SAG foam floods (Dong and Rossen (2007)), but these differences are outside the scope of this study. Also, UTCHEM represents shear-thinning in the low-quality regime as a function of gas superficial velocity rather than capillary number, which simplifies the fitting of the shear-thinning parameter σ from the procedure for *epcap* we outline above. Cheng et al. note that σ, the power-law exponent for foam, is related to *epcap* by

$$\sigma \cong \frac{1}{1 + epcap} \tag{B.1}$$

B.2   RELATIVE-PERMEABILITY FUNCTIONS AND FLUID PROPERTIES USED

The relative-permeability functions employed in this study are all of the form:

$$k_{rw} = k_{rw}^0 \left(\frac{S_w - S_{wr}}{1 - S_{wr} - S_{gr}} \right)^{n_w} \tag{B.2}$$

$$k_{rg} = k_{rg}^0 \left(\frac{1 - S_w - S_{gr}}{1 - S_{wr} - S_{gr}} \right)^{n_g} \tag{B.3}$$

where k_{rw}^0, k_{rg}^0, S_{wr}, S_{gr}, n_w and n_g are constants which vary per investigated data-set. **Table B.2** gives the values of these constants for each of the data sets that are investigated in our parameter-fitting approach for co-injection of gas and liquid (cf. Chapter 3). **Table B.3** gives the relative-permeability constants for the cases investigated in our parameter fitting approach for SAG applications along with some additional fluid properties (cf. Chapter 4). Finally, **Table B.4** gives the values of these constants and the other fluid properties and foam parameters used in the radial flow modeling of a SAG injection process (cf. Chapter 5).

Table B.2: Relative-permeability constants and other properties of the studies used in the fitting of foam model parameters to co-injection processes (cf. Chapter 3)

	MA ET AL. (2013)	ALVAREZ ET AL. (2001)	MORADI-ARAGHI ET AL. (1) (1997)	MORADI-ARAGHI ET AL. (2) (1997)	CHABERT ET AL. (2012)
k_{rw}^0	0.7888	0.20	0.20	0.20	0.28
k_{rg}^0	1	0.94	0.94	0.94	0.05
S_{wc}	0.05	0.20	0.20	0.20	0.32
S_{gr}	0.05	0.20	0.20	0.20	0.08
n_w	2.7233	4.2	4.2	4.2	1.02
n_g	2.2868	1.3	1.3	1.3	2.41

Table B.3: Relative-permeability constants, fluid properties and foam parameters used in fitting data for SAG foam applications (cf. Chapter 4)

	PERSOFF ET AL. (1991) MODEL FIT FROM ROSSEN ET AL. (1995)	MA ET AL. (2013) (STRAIGHT-LINE k_{rw} FUNCTION (FIGURE 4.8))	MA ET AL. (2013) (THEIR k_{rw} AND k_{rg} FUNCTIONS)
k_{rw}^0	0.2	0.0109	0.7888
k_{rg}^0	0.94	1	1
S_{wr}	0.2	0.05	0.05
S_{gr}	0.2	0.05	0.05
n_w	4.2	1	1.96
n_g	1.3	2.29	2.29
μ_w [Pa·s]	$1.2 \cdot 10^{-3}$	$1.0 \cdot 10^{-3}$	$1.0 \cdot 10^{-3}$
μ_g [Pa·s]	$2.0 \cdot 10^{-5}$	$2.0 \cdot 10^{-5}$	$2.0 \cdot 10^{-5}$
k [m^2]	$1.0 \cdot 10^{-12}$	$1.58 \cdot 10^{-10}$	$1.58 \cdot 10^{-10}$

Table B.4: Relative-permeability constants, fluid properties and foam parameters used in the radial-flow model and simulations (cf. Chapter 5)

	PERSOFF ET AL. (1990) "STRONG FOAM"	MA ET AL. (2013) STARS F_w FUNCTION	MA ET AL. (2013) MODIFIED F_w FUNCTION	"WEAK FOAM"
k_{rw}^0	0.2	0.0109	0.0109	0.2
k_{rg}^0	0.94	1	1	0.94
S_{wr}	0.2	0.05	0.05	0.2
S_{gr}	0.2	0.05	0.05	0.2
n_w	4.2	1	1	4.2
n_g	1.3	2.29	2.29	1.3
μ_w [Pa·s]	$1.2 \cdot 10^{-3}$	$1.0 \cdot 10^{-3}$	$1.0 \cdot 10^{-3}$	$1.0 \cdot 10^{-3}$
μ_g [Pa·s]	$2.0 \cdot 10^{-5}$	$2.0 \cdot 10^{-5}$	$2.0 \cdot 10^{-5}$	$2.0 \cdot 10^{-5}$
$fmmob$	25000	40000	50000	2500
$fmdry$	0.37	0.13	0.13	0.37
$epdry$	2500	150	100	20000

B.3   ADJUSTING DATA FOR COMPRESSIBILITY

The data of Ma et al. (2013) is adjusted for compressibility by assuming that the gas density varies linearly along the core (in effect, that the pressure gradient is uniform along the core). The pressure as a function of its position in the core can thus be written as

$$p(x) = p_L + (p_0 - p_L)\frac{x}{L} \tag{B.4}$$

where $p(x)$ is the pressure in the core at position x. Pressures p_L and p_0 apply respectively at the outlet and the inlet of the core. For the data of Ma et al. the value of p_L is equal to atmospheric pressure since no back pressure was applied in their experiments. L is the length of the core. We also assume the ideal gas law applies so the gas superficial velocity is inversely proportional to the pressure.

$$u_g(x) = u_g^L \frac{p_L}{p(x)} \tag{B.5}$$

where u_g^L is the gas superficial velocity at $x = L$. An expression for the average gas superficial velocity u_g in the core is found by integrating the function for u_g over the length of the core:

$$\langle u_g \rangle = \int_0^L \frac{u_g(x)}{L} = u_g^L \left[\frac{p_L}{p_0 - p_L} \ln\left(\frac{p_0}{p_L}\right) \right] \tag{B.6}$$

C

PRESSURE DIFFERENCE ACROSS A FOAM BANK IN A SINGLE-SLUG SAG FOAM PROCESS

We consider the pressure difference between the injection well ($r = r_w$) and the leading edge of the foam bank, which is at position r_f, during gas injection in a single-slug SAG process. Darcy's law in horizontal radial flow gives

$$u_t(r) = \frac{Q}{2\pi Hr} = -k\lambda_{rt}(r)\frac{dp}{dr} \tag{C.1}$$

where u_t is total superficial velocity, Q total volumetric (in this case, gas) injection rate, H formation thickness, k absolute permeability, λ_{rt} total relative mobility and p pressure. Rearranging,

$$p(r_w) - p(r_f) = \int_{r_w}^{r_f} \frac{Q}{2\pi Hk\lambda_{rt}(r)} d\ln r \equiv \frac{Q}{I_f} \tag{C.2}$$

Suppose $r_w = 0$; then $r^2/r_e^2 = x_D$ and $d\ln(r) = \frac{1}{2}d\ln(x_D)$ (Eq. (5.1)), and

$$p(r_w) - p(r_f) = \int_{0}^{x_D(r_f)} \frac{Q}{4\pi Hk\lambda_{rt}(x_D)} d\ln x_D \tag{C.3}$$

Let η be the slope of the characteristics, i.e. $\eta = dx_D/dt_D = df_w/dS_w$ for the values of S_w along each characteristic. Along each characteristic, η is a constant, and $x_D = \eta t_D$. At fixed time t_D, $d\ln x_D = d\ln \eta$. Moreover, mobilities are functions of water saturation S_w, which is constant along each characteristic and therefore implicitly a function of η. Thus

$$p(r_w) - p(r_f) = \int_{0}^{\eta_{shock}} \frac{Q}{4\pi Hk\lambda_{rt}(S_w(\eta))} d\ln \eta \tag{C.4}$$

where η_{shock} is the slope of the fractional-flow curve at the point of tangency representing the shock at $r = r_f$.

This integral depends only on mobilities and the fractional-flow curve $f_w(S_w)$ and therefore is independent of time: the implication is that the pressure dif-

ference across the foam bank is independent of time. Two observations immediately follow: First, if mobility at the well $\lambda_{rt}(S_w(\eta = 0))$ is finite, this integral diverges to infinity; the injection pressure according to Eq. (C.4) is infinite. Second, because $x_D = 0$ corresponds to $r = r_w$, not $r = 0$ (Eq. (5.1)), the integral in Eq. (C.4) is not exact and injection pressure is not actually infinite. The difference between Eq. (C.4) and the true injection pressure depends on mobility in the region near the well, where r is of the order of r_w. We contend that if mobility is sufficiently large near the wellbore that resistance to flow near the well is insignificant compared to resistance to flow further out, where Eq. (C.4) is accurate, then the implication of Eq. (C.4) is correct: the difference in pressure across the foam bank is nearly constant as the foam bank advances radially outward from the injection well. In other words, if mobility is sufficiently great near the well, the pressure difference in Eq. (C.2) is nearly constant for $r_w \ll r_f \leq r_e$. It remains to demonstrate that this conjecture is correct. For the following calculations we assume a wellbore radius $r_w = 0.1$ m and an outer radius $r_e = 100$ m. We define dimensionless pressure rise as that with foam divided by that injecting water at the same volumetric injection rate with $S_w = 1$ throughout the reservoir (i.e., at the initial state of the reservoir).

Figure C.1a shows the dimensionless pressure difference across the foam bank and total pressure difference to outer radius r_e as a function of pore volumes gas injected, for the model parameters derived in Chapter 4 from data of Persoff et al. (1990). The parameter values and physical properties used are described in Appendix B. For simplicity we have assumed a zero oil saturation, as in the data of Persoff et al., to which the model was fit. This model fit was designed specifically to represent a SAG flood, but, as noted in Chapter 4, there are almost no data for the extremely dry conditions between the leading edge of the foam bank and the injection well. At time $t_D = 0$, before gas injection, total dimensionless pressure difference is 1 (at the initial state of the reservoir), but by $t_D = 0.001$ it has risen to 2.39. It is remarkable that the pressure difference across the foam bank is so nearly constant with time, given that with this model fit foam does not collapse completely at the injection well - gas mobility is reduced there by a factor of 21 (cf. Chapter 4). Evidently, as posited above, if mobility is finite but comparatively large in the near-wellbore region, the pressure difference across the foam bank is nearly constant with time.

The importance of accurately modeling foam at the injection well is illustrated by another model fit in Chapter 4, that to the data of Ma et al. (2013). In Chapter 4 a good fit is obtained to the range of steady-state foam-mobility and water-saturation data provided by Ma et al., but, again, with few data to fit representing the dry conditions between the injection well and the leading edge of the foam bank. To fit those data, they selected parameter values whereby gas

mobility is reduced at the injection well by a factor of about 1000, and gas mobility hardly varies within the foam bank. As a result, the injectivity of the gas bank in this SAG process is worse than that of a 20 cp fluid. As shown in **Figure C.1b**, dimensionless injection pressure across the foam bank is enormous and grows with time.

This behavior reflects the form of the dryout function in the STARS foam model (Cheng et al. (2000); Computer Modeling Group (2006)), in which foam does not collapse completely even at irreducible water saturation S_{wr} (Eq. (3.3)).

Figure C.1: Dimensionless pressure difference across foam bank (dashed line) and total pressure difference from r_w to r_e (solid line): (a) for model fit of Rossen and Boeije ((SPE 165282) to data of Persoff et al. (1990) (b) for model fit of Rossen and Boeije ((SPE 165282) to data of Ma et al. (2013).

Namdar Zanganeh et al. (2011) suggest a simple modification of this function, whereby the dryout factor at $S_w = S_{wr}$ is subtracted from that at all values of S_w. Foam is thus completely destroyed at $S_w = S_{wr}$. This modified dryout equation becomes:

$$F_2 = \left(0.5 + \frac{\arctan(epdry(S_w - fmdry))}{\pi} \right)$$
$$- \left(0.5 + \frac{\arctan(epdry(S_{wr} - fmdry))}{\pi} \right)$$

(C.5)

To fit the range of data of Ma et al. with the new dryout function, the other parameters must be adjusted as well, as illustrated in Table B.4. With the new model fit, the mobility at the leading edge of the foam bank is 31 $(\text{Pa·s})^{-1}$, whereas with the previous fit it is somewhat lower, 22 $(\text{Pa·s})^{-1}$. More important, gas mobility is high near the injection well, where foam collapses. As shown in Fig. C.2a, the pressure difference across the foam bank is nearly constant with time, until the leading edge of the foam bank exits the region of interest at $t_D = 0.93$.

As a final example, we take a parameter set not derived from data, but which would give a foam just sufficient to maintain mobility control. We return here

to the STARS foam model (Eq. (4.1)). For the parameter values in the final column of Table B.4, foam mobility is 682 $(Pa \cdot s)^{-1}$ at the leading edge of the foam bank, a little less than the mobility ahead of it, 1000 $(Pa \cdot s)^{-1}$. Because of larger mobility near the well, the dimensionless pressure difference across the foam bank is only about 22% of that at the initial condition. The dimensionless pressure differences over time are shown in Fig. C.2b. It is possible to maintain mobility control with a SAG process and greatly increase injectivity over that without gas.

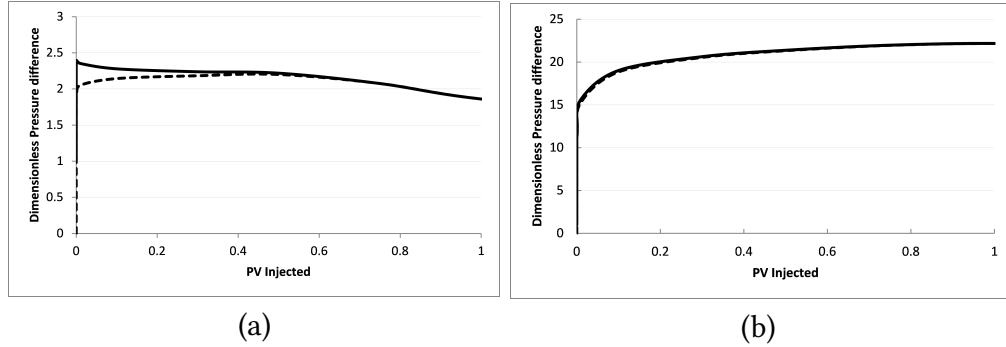(a)   (b)

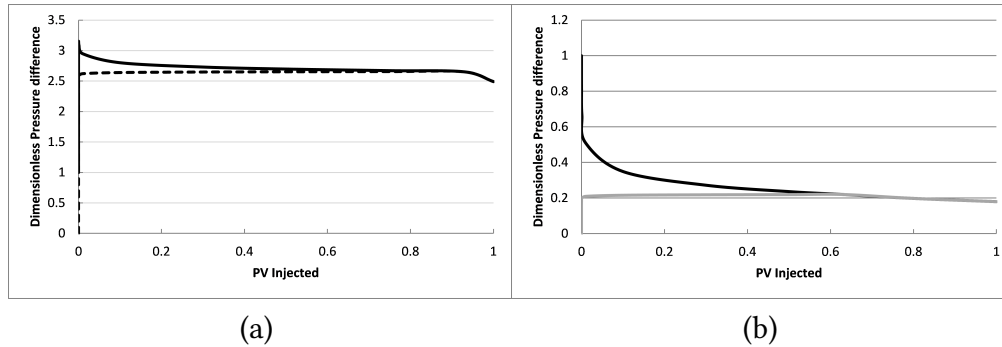Figure C.2: Dimensionless pressure difference across foam bank ((a) dashed line (b) gray line) and total pressure difference from r_w to r_e (black line): (a) for model fit of Rossen and Boeije ((SPE 165282) to data of Ma et al. (2013) using alternate form of dryout function where foam collapses at the injection well (b) for "weak" foam that is just sufficient to maintain mobility control at its leading edge.

BIBLIOGRAPHY

Aarra, M. G., Skauge, A., and Martinsen, H. A. FAWAG: A Breakthrough for EOR in the North Sea. *SPE Annual Technical Conference and Exhibition*, (SPE 77695), San Antonio, TX, USA, 29 September - 2 October 2002.

Afsharpoor, A. Mechanistic Foam Modeling and Simulations: Gas Injection During Surfactant-Alternating-Gas Processes Using Foam-Catastrophe Theory. Master's thesis, Louisiana State University, August 2009.

Alotaibi, M. B., Nasralla, R. A., and Nasr-El-Din, H. A. Wettability Challenges in Carbonate Reservoirs. *SPE Improved Oil Recovery Symposium*, (SPE 129972), Tulsa, OK, USA, 24-28 April 2010.

Alvarez, J. M., Rivas, H. J., and Rossen, W. R. Unified Model for Steady-State Foam Behavior at High and Low Foam Qualities. *SPE Journal*, 6:325–333, 2001.

Andrianov, A., Farajzadeh, R., Mahmoodi Nick, M., Talanana, M., and Zitha, P. L. J. Immiscible Foam for Enhancing Oil Recovery: Bulk and Porous Media Experiments. *SPE Enhanced Oil Recovery Conference*, (SPE 143578), Kuala Lumpur, Malaysia, 19-21 July 2011.

Ashoori, E. and Rossen, W. R. Can Formation Relative Permeabilities Rule Out a Foam EOR Process? *SPE Journal*, 17:340–351, 2012.

Ashoori, E., van der Heijden, T. L. M., and Rossen, W. R. Fractional-Flow Theory of Foam Displacements with Oil. *SPE Journal*, 15:260–273, 2010.

Bernard, G. G. and Holm, L. W. Effect of Foam on Permeability of Porous Media to Gas. *Society of Petroleum Engineers Journal*, 4:267–274, 1964.

Bertin, H. J., Apaydin, O. G., Castanier, L. M., and Kovscek, A. R. Foam Flow in Heterogeneous Porous Media: Effect of Cross Flow. *SPE Journal*, 4:75–82, 1999.

Bird, R. B., Stewart, W. E., and Lightfoot, E. N. *Transport Phenomena*. John Wiley & Sons, Inc.; 2nd edition, 2002.

Blaker, T., Aarra, M. G., Skauge, A., Rasmussen, L., Celius, H. K., Martinsen, H. A., and Vassenden, F. Foam for Gas Mobility Control in the Snorre Field:

The FAWAG Project. *SPE Reservoir Evaluation & Engineering*, 5:317–323, August 2002.

Boeije, C. S. and Rossen, W. R. Fitting Foam-Simulation-Model Parameters to Data: I. Coinjection of Gas and Liquid. *SPE Reservoir Evaluation & Engineering*, Vol. 18 (02)(SPE 174544):pp. 264 – 272, May 2015.

Bond, D. C. and Holbrook, O. C. Gas Drive Oil Recovery Process. *US patent 2866507*, December 1958.

BP Statistical Review of World Energy June 2015. Technical report.

Chabert, M., Morvan, M., and Nabzar, L. Advanced Screening Technologies for the Selection of Dense CO2 Foaming Surfactants. *SPE Improved Oil Recovery Symposium*, Tulsa, OK, USA, 14-18 April 2012. ISSN 978-1-61399-197-8.

Chen, P. and Mohanty, K. K. Wettability Alteration in High Temperature Carbonate Reservoirs. *SPE Improved Oil Recovery Symposium*, (SPE 169125), Tulsa, OK, USA, 12-16 April 2014.

Cheng, L., Reme, A. B., Shan, D., Coombe, D. A., and Rossen, W. R. Simulating Foam Processes at High and Low Foam Qualities. *SPE/DOE Symposium on Improved Oil Recovery*, (SPE 59287), Tulsa, OK, USA, 3-5 April 2000.

Computer Modeling Group. *STARS User's Guide.* Calgary, Alberta, Canada, Version 2006.

Coombe, D. A. personal communication. 2012.

de Velde Harsenhorst, R. M., Dharma, A. S., Andrianov, A., and Rossen, W. R. Extension and Verification of a Simple Model for Vertical Sweep in Foam Surfactant-Alternating-Gas Displacements. *SPE Reservoir Evaluation & Engineering*, 17:373–383, 2014.

Dong, Y. and Rossen, W. R. Insights from Fractional-Flow Theory for Models for Foam IOR. *14th European Symposium on Improved Oil Recovery*, Cairo, Egypt, 22-24 April 2007.

Duerksen, J. H. Laboratory Study of Foaming Surfactants as Steam-Diverting Additives. *SPE Reservoir Engineering*, 1:44–52, 1986.

Ehrenberg, S. N. and Nadeau, P. H. Sandstone vs. carbonate petroleum reservoirs: A global perspective on porosity-depth and porosity-permeability relationships. *AAPG Bulletin*, 89:435–445, April 2005.

Essary, R. L. and Rogers, E. E.   Techniques and Results of Foam Redrilling Operations-San Joaquin Valley, California.   *SPE Symposium on Formation Damage Control*, (SPE-5715-MS), Houston, TX, USA, 29-30 January 1976.

Ettinger, R. A. and Radke, C. J. Influence of Texture on Steady Foam Flow in Berea Sandstone. *SPE Reservoir Engineering*, 7(01):83–90, 1992.

Faisal, A., Bisdom, K., Zhumabek, B., Zadeh, A. M., and Rossen, W. R.   Injectivity and Gravity Segregation in WAG and SWAG Enhanced Oil Recovery. *SPE Annual Technical Conference and Exhibition*, (SPE 124197), New Orleans, Louisiana, USA, 4-7 October 2009.

Falls, A. H., Hirasaki, G. J., Patzek, T. W., Gauglitz, D. A., Miller, D. D., and Ratulowski, J. Development of a Mechanistic Foam Simulator: The Population Balance and Generation by Snap-Off. *SPE Reservoir Engineering*, 3:884–892, 1988.

Farajzadeh, R., Andrianov, A., Krastev, R., Hirasaki, G. J., and Rossen, W. R. Foam-Oil Interaction in Porous Media: Implications for Foam Assisted Enhanced Oil Recovery. *Advances in Colloid and Interface Science*, 183-184:1 – 13, 2012. ISSN 0001-8686. doi: http://dx.doi.org/10.1016/j.cis.2012.07.002. URL `http://www.sciencedirect.com/science/article/pii/S0001868612001121`.

Farajzadeh, R. personal communication. 2013.

Fisher, A. W., Foulser, R. W. S., and Goodyear, S. G. Mathematical Modeling of Foam Flooding. *SPE/DOE Symposium on Enhanced Oil Recovery*, (SPE/DOE 20195), Tulsa, OK, USA, 22-25 April 1990.

Friedmann, F., Chen, W. H., and Gauglitz, P. A. Experimental and Simulation Study of High-Temperature Foam Displacement in Porous Media. *SPE Reservoir Engineering*, 6:37–75, 1991.

Gauglitz, P. A., Friedmann, F., Kam, S. I., and Rossen, W. R. Foam Generation in Homogeneous Porous Media. *Chemical Engineering Science*, 57:4037–4052, 2002.

Grassia, P., Mas-Hernández, E., Shokri, N., Cox, S. J., Mishuris, G., and Rossen, W. R. Analysis of a Model for Foam Improved Oil Recovery. *Journal of Fluid Mechanics*, 751:346–405, 2014.

Gupta, R., Mohan, K., and Mohanty, K. K. Surfactant Screening for Wettability Alteration in Oil-Wet Fractured Carbonates. *SPE Annual Technical Conference and Exhibition*, (SPE 124822), New Orleans, LA, USA, 4-7 October 2009.

Haugen, A., Fernø, M. A., Graue, A., and Bertin, H. J. Experimental Study of Foam Flow in Fractured Oil-Wet Limestone for Enhanced Oil Recovery. *SPE Reservoir Evaluation & Engineering*, 2012.

Hirasaki, G. J. and Lawson, J. B. Mechanisms of Foam Flow in Porous Media: Apparent Viscosity in Smooth Capillaries. *SPE Journal*, 25:176–190, 1985.

Hirasaki, G. J., Miller, C. A., Szafranski, R., Lawson, J. B., and Akiya, N. Surfactant/Foam Process for Aquifer Remediation. *SPE International Symposium on Oilfield Chemistry*, (SPE 37257), Houston, TX, USA, 18-21 February 1997a.

Hirasaki, G. J., Miller, C. A., Szafranski, R., Lawson, J. B., Meinardus, M. J., Londergan, J. T., Jackson, R. E., Pope, G. A., and Wade, W. H. Field Demonstration of the Surfactant/Foam Process for Aquifer Remediation. *SPE Annual Technical Conference and Exhibition*, (SPE 39292), San Antonio, TX, USA, 5-8 October 1997b.

Islam, M. R. and Farouq-Ali, S. M. Numerical Simulation of Foam Flow in Porous Media. *Journal of Canadian Petroleum Technology*, 29(4):47–51, 1990.

Kam, S. I. and Rossen, W. R. A Model for Foam Generation in Homogeneous Porous Media. *SPE Journal*, 8:417–425, 2003.

Kam, S. I., Nguyen, Q. P., and Rossen, W. R. Dynamic Simulations With an Improved Model for Foam Generation. *SPE Journal*, 12:35–48, 2007.

Kapetas, L., van El, W. A., and Rossen, W. R. Representing Slow Foam Dynamics in Laboratory Corefloods for Enhanced Oil Recovery. *SPE Improved Oil Recovery Symposium*, (SPE 169059), Tulsa, OK, USA, 12-16 April 2014.

Kapetas, L., Vincent-Bonnieu, S., Danelis, S., and Rossen, W. R. Effect of Temperature on Foam Flow in Porous Media. *SPE Middle East Oil & Gas Show and Conference*, (SPE 172820), Manama, Bahrain, 8-11 March 2015.

Kestin, J., Sokolov, M., and Wakeham, W. A. Viscosity of Liquid Water in the Range -8 degC to 150 degC. *Journal of Physical and Chemical Reference Data*, 7(3):941 − 948, July 1978.

Key World Energy Statistics. Technical report, International Energy Agency, 2014.

Khatib, Z. I., Hirasaki, G. J., and Falls, A. H. Effects of Capillary Pressure on Coalescence and Phase Mobilities in Foams Flowing through Porous Media. *SPE Reservoir Engineering*, 3:919–926, 1988.

Kibodeaux, K. R. and Rossen, W. R. Coreflood Study of Surfactant-Alternating-Gas Foam Processes: Implications for Field Design. *SPE Western Regional Meeting*, (SPE 38318), Long Beach, CA, USA, 25-27 June 1997.

Kibodeaux, K. R., Zeilinger, S. C., and Rossen, W. R. Sensitivity Study of Foam Diversion Processes for Matrix Acidization. *SPE Annual Technical Conference and Exhibition*, (SPE 28550), New Orleans, LA, USA, 26-28 September 1994.

Kim, J. S., Dong, Y., and Rossen, W. R. Steady-State Flow Behavior of CO2 Foam. *SPE Journal*, 10:405–415, 2005.

Kloet, M. B., Renkema, W. J., and Rossen, W. R. Optimal Design Criteria for SAG Foam Processes in Heterogeneous Reservoirs. *SPE EUROPEC/EAGE Annual Conference and Exhibition*, (SPE 121581), Amsterdam, The Netherlands, 8-11 June 2009.

Kovscek, A. R. and Radke, C. J. *Fundamentals of Foam Transport in Porous Media*. Number 242 in Advances in Chemistry Series. American Chemical Society, Washington, DC, USA, 1994.

Kovscek, A. R., Patzek, T. W., and Radke, C. J. A Mechanistic Population Balance Model for Transient and Steady-State Foam Flow in Boise Sandstone. *Chemical Engineering Science*, 50(23):3783–3799, December 1995a.

Kovscek, A. R., Tretheway, D. C., Persoff, P., and Radke, C. J. Foam Flow Through a Transparent Rough-Walled Rock Fracture. *Journal of Petroleum Science and Engineering*, 13:75–86, 1995b.

Kovscek, A. R., Chen, Q., and Gerritsen, M. Modeling Foam Displacement with the Local-Equilibrium Approximation: Theory and Experimental Verification. *SPE Journal*, 15:171–183, 2010.

Kristiansen, T. S. and Holt, T. Properties of Flowing Foam in Porous Media Containing Oil. *SPE/DOE Symposium on Enhanced Oil Recovery*, (SPE/DOE 24182), Tulsa, OK, USA, 22-24 April 1992.

Kuehne, D. L., Frazier, R. H., Cantor, J., and Horn Jr., W. Evaluation of Surfactants for CO2 Mobility Control in Dolomite Reservoirs. *SPE/DOE Symposium on Enhanced Oil Recovery*, (SPE/DOE 24177), Tulsa, OK, USA, 22-24 April 1992.

Kular, G. S., Lowe, K., and Coombe, D. Foam Application in an Oil Sands Steam Flood Process. *SPE Annual Technical Conference and Exhibition*, (SPE 19690), San Antonio, TX, USA, 8-11 October 1989.

Kumar, K., Dao, E. K., and Mohanty, K. K. Atomic Force Microscopy Study of Wettability Alteration by Surfactants. *SPE Journal*, 13:137–145, 2008.

Lake, L. W. *Enhanced Oil Recovery*. Prentice Hall, Englewood Cliffs, New Jersey, USA, 1989.

Lake, L. W., Johns, R. T., Pope, G. A., and Rossen, W. R. *Fundamentals of Enhanced Oil Recovery.* Society of Petroleum Engineers, Richardson, TX, 2014, 2014.

Lau, H. C. and O'Brien, S. M. Effects of Spreading and Nonspreading Oils on Foam Propagation Through Porous Media. *SPE Reservoir Engineering*, 3:893–896, 1988.

Law, D. H., Yang, Z. M., and Stone, T. Effect of Presence of Oil on Foam Performance: A Field Simulation Study. *SPE Symposium on Reservoir Simulation*, (SPE 18721), Houston, TX, USA, 6-8 February 1989.

Le, V. Q., Nguyen, Q. P., and Sanders, A. W. A Novel Foam Concept with CO2 Dissolved Surfactants. *SPE/DOE Symposium on Improved Oil Recovery*, (SPE 113370), Tulsa, OK, USA, 20-23 April 2008.

Lee, H. O. and Heller, J. P. Laboratory Measurements of CO2-Foam Mobility. *SPE Reservoir Engineering*, 5:193–197, 1990.

Leeftink, T., Latooij, C., and Rossen, W. Injectivity errors in simulation of foam EOR. *Journal of Petroleum Science and Engineering*, 126:26 – 34, 2015. ISSN 0920-4105.

Lescure, B. M. and Claridge, E. L. CO2 Foam Flooding Performance vs. Rock Wettability. *SPE Annual Technical Conference and Exhibition*, (SPE 15445), New Orleans, LA, USA, 5-8 October 1986.

Li, R. F., Hirasaki, G. J., Miller, C. A., and Masalmeh, S. K. Wettability Alteration and Foam Mobility Control in an Layered, 2D Heterogeneous Sandpack. *SPE Journal*, 17:1207–1220, 2012.

Ma, K., Farajzadeh, R., Lopez-Salinas, J. L., Miller, C. A., Biswal, S. L., and Hirasaki, G. J. Non-uniqueness, Numerical Artifacts, and Parameter Sensitivity in Simulating Steady-State and Transient Foam Flow Through Porous Media. *Transport in Porous Media*, 102(3):325–348, 2014.

Ma, K., Lopez-Salinas, J. L., Puerto, M. C., Miller, C. A., Biswal, S. L., and Hirasaki, G. J. Estimation of Parameters for the Simulation of Foam Flow through Porous Media. Part 1: The Dry-Out Effect. *Energy & Fuels*, 27(5): 2363–2375, 2013.

Mamun, C. K., Rong, J. G., Kam, S. I., Liljestrand, H. M., and Rossen, W. R. Extending Foam Technology from Improved Oil Recovery to Environmental Remediation. *SPE Annual Technical Conference and Exhibition*, (SPE 77557), San Antonio, TX, USA, 29 September - 2 October 2002.

Mannhardt, K., Novosad, J. J., and Schramm, L. L. Foam/Oil Interaction at Reservoir Conditions. *SPE/DOE Symposium on Enhanced Oil Recovery*, (SPE 39681), Tulsa, OK, USA, 19-22 April 1998.

Martinsen, H. A. and Vassenden, F. Foam-Assisted Water Alternating Gas (FAWAG) Process on Snorre. *10th European Symposium on Improved Oil Recovery*, Brighton, UK, 18-20 August 1999.

Mayberry, D. J., Afsharpoor, A., and Kam, S. I. The Use of Fractional-Flow Theory for Foam Displacement in Presence of Oil. *SPE Reservoir Evaluation & Engineering*, 11:707–718, 2008.

Melzer, L. S. Carbon Dioxide Enhanced Oil Recovery (CO2 EOR): Factors Involved in Adding Carbon Capture, Utilization and Storage (CCUS) to Enhanced Oil Recovery. February 2012. Melzer Consulting for the National Enhanced Oil Recovery Initiative, Center for Climate and Energy Solutions.

Mohamed, I. M. and Nasr-El-Din, H. A. Formation Damage Due to CO2 Sequestration in Deep Saline Carbonate Aquifers. *SPE International Symposium and Exhibition on Formation Damage Control*, (SPE 151142), Lafayette, LA, USA, 15-17 February 2012.

Mohammadi, S. and Coombe, D. Characteristics of Steam-Foam Drive Process in Massive Multi-Zone and Thin Single-Zone Reservoirs. *SPE Western Regional Meeting*, (SPE 14030), Bakersfield, CA, USA, 30 March - 1 April 1992.

Mohammadi, S. S., Coombe, D. A., and Stevenson, V. M. Test of Steam-foam Process for Mobility Control in South Casper Creek Reservoir. *Journal of Canadian Petroleum Technology*, 32:49–54, 1993.

Moradi-Araghi, A., Johnston, E. L., Zomes, D. R., and Harpole, K. J. Laboratory Evaluation of Surfactants for CO2-Foam Applications at the South Cowden Unit. *SPE International Symposium on Oilfield Chemistry*, (SPE 37218), Houston, TX, USA, 18-21 February 1997.

Muggeridge, A., Cockin, A., Webb, K., Frampton, H., Collins, I., Moulds, T., and Salino, P. Recovery Rates, Enhanced Oil Recovery and Technological Limits. *Philosphical Transactions of the Royal Society A*, 372, 2013.

Myers, T. J. and Radke, C. J. Transient Foam Displacement in the Presence of Residual Oil: Experiment and Simulation Using a Population-Balance Model. *Industrial & Engineering Chemistry Research*, 39:2725–2741, 2000.

Namdar Zanganeh, M. and Rossen, W. Optimization of Foam Enhanced Oil Recovery: Balancing Sweep and Injectivity. *SPE Reservoir Evaluation & Engineering*, 16:51–59, 2013.

Namdar Zanganeh, M., Kam, S. I., LaForce, T., and Rossen, W. R. The Method of Characteristics Applied to Oil Displacement by Foam. *SPE Journal*, 16:8–23, 2011.

Nguyen, Q. P., Zitha, P. L. J., Currie, P. K., and Rossen, W. R. CT Study of Liquid Diversion with Foam. *SPE Production & Operations*, 24:12–21, 2009.

Osterloh, W. T. and Jante, M. J. Effects of Gas and Liquid Velocity on Steady-State Foam Flow at High Temperature. *SPE/DOE Symposium on Enhanced Oil Recovery*, (SPE/DOE 24179), Tulsa, OK, USA, 22-24 April 1992.

Patzek, T. W. and Myhill, N. A. Simulation of the Bishop Steam Foam Pilot. *SPE California Regional Meeting*, (SPE 18786), Bakersfield, CA, USA, 5-7 April 1989.

Persoff, P., Pruess, K., Benson, S., Wu, Y., Radke, C., Witherspoon, P., and Shikari, Y. Aqueous Foams for Control of Gas Migration and Water Coning in Aquifer Gas Storage. *Energy Sources*, 12(4):479–497, 1990. URL `http://dx.doi.org/10.1080/00908319008960220`.

Persoff, P., Radke, C. J., Pruess, K., and Benson, S. M. A Laboratory Investigation of Foam Flow in Sandstone at Elevated Pressure. *SPE Reservoir Engineering*, 6:185–192, 1991.

Rangel-German, E., Akin, S., and Castanier, L. Multiphase-Flow Properties of Fractured Porous Media. *SPE Western Regional Meeting*, (SPE 54591), Anchorage, Alaska, 26-28 May 1999.

Ransohoff, T. C. and Radke, C. J. Mechanisms of Foam Generation in Glass-Bead Packs. *SPE Reservoir Engineering*, 3:573–585, 1988.

Robelius, F. *Giant Oil Fields - The Highway to Oil.* PhD thesis, Uppsala Universitet, 2007.

Robert, J. A. and Mack, M. G. Foam Diversion Modeling and Simulation. *SPE Production & Facilities*, 12:123–128, 1997.

Rossen, W. R. *Foams in Enhanced Oil Recovery*. in R. K. Prud'homme and S. Khan, ed., Foams: Theory, Measurements and Applications. Marcel Dekker, New York, 1996.

Rossen, W. R. Numerical Challenges in Foam Simulation: A Review. *SPE Annual Technical Conference and Exhibition*, (SPE 166244), New Orleans, LA, 30 September-2 October 2013.

Rossen, W. R. and Boeije, C. S. Fitting Foam-Simulation-Model Parameters to Data: II. Surfactant-Alternating-Gas Foam Applications. *SPE Reservoir Evaluation & Engineering*, Vol. 18 (02):pp. 273 – 283, (SPE 165282), May 2015.

Rossen, W. R. and Bruining, J. Foam Displacements With Multiple Steady States. *SPE Journal*, 12:5–18, 2007.

Rossen, W. R. and Wang, M. W. Modeling Foams for Acid Diversion. *SPE Journal*, 4:92–100, 1999.

Rossen, W. R., Zeilinger, S. C., Shi, J. X., and Lim, M. T. Simplified Mechanistic Simulation of Foam Processes in Porous Media. *SPE Journal*, 4:279–287, 1999.

Rossen, W. R., van Duijn, C., Nguyen, Q. P., Shen, C., and Vikingstad, A. K. Injection Strategies to Overcome Gravity Segregation in Simultaneous Gas and Water Injection Into Homogeneous Reservoirs. *SPE Journal*, 15:76–90, 2010.

Sanchez, J. M. and Hazlett, R. D. Foam Flow Through an Oil-Wet Porous Medium: A Laboratory Study. *SPE Reservoir Engineering*, 7:91–97, 1992.

Schlumberger. *ECLIPSE* Reservoir Simulation Software, Version 2010.2, Technical Description*, 2010.

Schramm, L. L. *Foams: Fundamentals and Applications in the Petroleum Industry*. Number 242 in Advances in Chemistry Series. American Chemical Society, Washington, DC, USA, 1994. URL `http://pubs.acs.org/doi/abs/10.1021/ba-1994-0242.fw001`.

Seethepalli, A., Adibhatla, B., and Mohanty, K. K. Wettability Alteration During Surfactant Flooding of Carbonate Reservoirs. *SPE/DOE Fourteenth Symposium on Improved Oil Recovery*, (SPE 89423), Tulsa, OK, USA, 17-21 April 2004 2004.

Shan, D. and Rossen, W. R. Optimal Injection Strategies for Foam IOR. *SPE Journal*, 9:132–150, 2004.

Shi, J. X. and Rossen, W. R. Improved Surfactant-Alternating-Gas Foam Process to Control Gravity Override. *SPE/DOE Improved Oil Recovery Symposium*, (SPE 39653), Tulsa, OK, USA, 19-22 April 1998.

Shojai Kaveh, N., Rudolph, E. S. J., Wolf, K.-H. A. A., and Ashrafizadeh, S. A. Wettability Determination by Contact Angle Measurements: hvbB Coal-Water System With Injection of Synthetic Flue Gas and CO2. *Journal of Colloid and Interface Science*, 364:237–247, 2011.

Singh, R. and Mohanty, K. K. Foams SStabilize by In-Sity Surface Activated Nanoparticles in Bulk and Porous Media. *SPE Annual Technical Conference and Exhibition*, (SPE-170942-MS), Amsterdam, The Netherlands, 27-29 October 2014.

Skauge, A., Aarra, M. G., Surguchev, L., Martinsen, H. A., and Rasmussen, L. Foam-Assisted WAG: Experience from the Snorre Field. *SPE/DOE Improved Oil Recovery Symposium*, (SPE 75157), Tulsa, OK, USA, 13-17 April 2002.

Stone, H. L. A Simultaneous Water and Gas Flood Design with Extraordinary Vertical Gas Sweep. *International Petroleum Conference*, (SPE 91724), Puebla, PUE, Mexico, 7-9 November 2004.

Suffridge, F. E., Raterman, K. T., and Russell, G. C. Foam Performance Under Reservoir Conditions. *SPE Annual Technical Conference and Exhibition*, (SPE 19691), San Antonio, TX, USA, 8-11 October 1989.

Szlendak, S. M., Nguyen, N., and Nguyen, Q. P. Successful Laboratory Investigation of Low-Tension-Gas (LTG) Flooding for Tertiary Oil Recovery in Tight FFormation (10mD to Gas). *SPE Annual Technical Conference and Exhibition*, (SPE 159841), San Antonio, TX, USA, 8-10 October 2012.

Tanzil, D., Hirasaki, G. J., and Miller, C. A. Mobility of Foam in Heterogeneous Media: Flow Parallel and Perpendicular. *SPE Journal*, 7:203 − 212, 2002.

Tsau, J.-S. and Grigg, R. B. Assessment of Foam Properties and Effective in Mobility Reduction for CO2-Foam Floods. *SPE International Symposium on Oilfield Chemistry*, (SPE 37221), Houston, TX, USA, 18-21 February 1997.

Tsau, J.-S., Yaghoobi, H., and Grigg, R. B. Smart Foam to Improve Oil Recovery in Heterogeneous Porous Media. *SPE Improved Oil Recovery Symposium*, (SPE 29677), Tulsa, OK, USA, 19-22 April 1998.

Turta, A. T. and Singhal, A. K. Field Foam Applications in Enhanced Oil Recovery Projects: Screening and Design Aspects. *SPE International Conference and Exhibition*, (SPE 48895), 1998.

Vikingstad, A. K., Skauge, A., Høiland, H., and Aarra, M. Foam-oil interaction analyzed by static foam tests. *Colloids and Surfaces A: Physicochemical and Engineering Aspects*, 260:189–198, 2005.

Walsh, M. P. and Lake, L. W. Applying Fractional-Flow Theory to Solvent Flooding and Chase Fluid. *Journal of Petroleum Science and Engineering*, 2: 281–303, 1989.

Wang, L. and Mohanty, K. K. Improving Oil Recovery in Gas-Flooded, Oil-Wet Carbonate Reservoirs by Wettability Altering Surfactants. *SPE International Symposium on Oilfield Chemistry*, (SPE 164126), The Woodlands, TX, USA, 8-10 April 2013 2013.

Wolfram, C., Shelef, O., and Gertler, P. J. How Will Energy Demand Develop in the Developing World? Technical Report 17747, National Bureau of Economic Research, 2012.

Xing, D., Wei, B., McLendon, W., Enick, R., McNulty, S., Tricket, K., Mohamed, A., Cummings, S., Eastoe, J., Rogers, S., Crandall, D., Tennant, B., McLendon, T., Romanov, V., and Soong, Y. CO2-Soluble, Nonionic, Water-Soluble Surfactants That Stabilize CO2-in-Brine Foams. *SPE Journal*, 17-04:1172–1185, December 2012.

Xu, Q. and Rossen, W. R. Effective Viscosity of Foam in Periodically Constricted Tubes. *Colloids and Surfaces A: Physicochemical and Engineering Aspects*, 216: 175–194, 2003.

Xu, Q. and Rossen, W. R. Experimental Study of Gas Injection in Surfactant-Alternating-Gas Foam Process. *SPE Reservoir Evaluation & Engineering*, 7: 438–448, 2004.

Yang, S. H. and Reed, R. L. Mobility Control Using CO2 Forms. *SPE Annual Technical Conference and Exhibition*, (SPE 19689), San Antonio, Texas, USA, 8-11 October 1989.

Zeilinger, S. C., Wang, M., Kibodeaux, K. R., and Rossen, W. R. Improved Prediction of Foam Diversion in Matrix Acidization. *SPE Production Operations Symposium*, (SPE 29529), Oklahoma City, OK, USA, 2-4 April 1995.

Zerhboub, M., Touboul, E., and Ben-Naceur, K. Matrix Acidizing: A Novel Approach to Foam Diversion. *SPE Annual Technical Conference and Exhibition*, (SPE 22854), Dallas, TX, USA, 6-9 October 1991.

Zhou, Z. and Rossen, W. R. Applying Fractional-Flow Theory to Foam Processes at the "Limiting Capillary Pressure. *SPE Advanced Technology Series*, 3:154–162, 1995.

NOMENCLATURE

$epcap$	Parameter that captures shear-thinning behavior in the low-quality regime
$epdry$	Parameter controlling the abruptness of foam collapse
F_1, F_2, etc.	Factors to account for effects of water saturation and other conditions on foam
f_g	Gas fractional flow
f_g^*	Gas fractional flow at transition between foam regimes
f_g^+	Specific gas fractional flow used for fitting function F_5
f_w	Water fractional flow
$fmcap$	parameter that is set to the smallest capillary number expected to be encountered by foam in the simulation
$fmdry$	Water saturation in vicinity of which foam collapses
$fmmob$	Reference gas mobility-reduction factor for wet foams
g	Gravitational acceleration
H	Formation thickness
I_f	Foam injectivity
I_{fD}	Dimensionless foam injectivity
k	Permeability
k_{rg}	Gas relative permeability without foam
k_{rg}^0	Pre-factor in gas relative permeability function
k_{rg}^f	Gas relative permeability with foam
k_{rw}	Water relative permeability
k_{rw}^0	Pre-factor in water relative permeability function
MRF	Mobility reduction factor
N_{ca}	Capillary number
n_g	Corey exponent for gas relative permeability function
n_w	Corey exponent for water relative permeability function
P_c	Capillary pressure
P_c^*	Limiting capillary pressure
p_0	Pressure at inlet of core

p_D	Dimensionless pressure
p_f	Pressure in the presence of foam
p_L	Pressure at outlet of core
p_w	Pressure in the absence of foam
Q	Volumetric injection rate
Q_D	Dimensionless volumetric injection rate
r	Radial position
r_e	Radius of region of interest
r_f	Radial position of leading edge of foam bank
r_w	Wellbore radius
RF	Mobility reduction factor as defined by Moradi-Araghi et al. (1997)
S_{gr}	Residual gas saturation
S_w	Water saturation
S_{wc}	Connate water saturation
S_{wf}	Water saturation in the foam bank
S_{wr}	Irreducible water saturation
S_w^*	Limiting water saturation
T	Temperature
t	Time
t_D	Dimensionless time
u_g	Gas superficial velocity
u_t	Total superficial velocity
u_w	Water superficial velocity
x_D	Dimensionless position
∇p	Pressure gradient
∇p_{lim}	Lower limit of pressure gradient expected in simulations
η	Slope of characteristics: ($= \mathrm{d}x_d/\mathrm{d}t_d = \mathrm{d}f_w/\mathrm{d}S_w$)
φ	Porosity
λ_{rf}	Relative mobility of gas in foam bank
λ_{rt}	Total relative mobility
λ_{rt}^I	Total relative mobility at the initial condition
μ_{app}	Apparent viscosity of foam
μ_g	Gas viscosity
μ_w	Water viscosity
ρ	Density
σ_{wg}	Gas-water surface tension
τ	Width of foam front
τ_D	Dimensionless width of foam front
τ_D	Dimensionless width of foam front
τ^*	Width of foam front in model of de Velde Harsenhorst et al. (2014)

SUMMARY

Conventional oil recovery techniques cannot recover all of the oil from a reservoir. Currently, only 20 to 40% of the oil that is initially in place in the reservoir is recovered. Enhanced Oil Recovery (EOR) methods are required to recover part of the remaining 60 to 80%. A common EOR method is the injection of gas into the reservoir to displace oil and maintain pressure. Such a process tends to suffer from poor sweep efficiency, because of reservoir heterogeneity, viscous instability between injected the gas and the more-viscous fluids it displaces, and gravity override of gas. The application of foam EOR is a method of addressing these problems. Foam traps the gas in individual bubbles, thereby reducing its mobility, which causes a more-stable displacement front and thus an increase in volumetric sweep.

The work described in this thesis explores various aspects of foam enhanced oil recovery and is especially focused towards the use of foam in carbonate formations. To this end, several topics are discussed, from surfactant screening to designing parameter-fitting approaches, modeling surfactant-alternating-gas (SAG) injection processes and ultimately performing experiments in consolidated carbonate cores.

A necessary first step towards a successful foam EOR project is finding a foaming surfactant appropriate for use under harsh operating conditions. In **Chapter 2**, we introduce a screening methodology for foaming surfactants that can be used both to quickly screen large numbers of surfactants through bulk-foam tests and also provide quantitative foaming performance data through foam flooding tests. We find that salinity is a major concern for surfactant performance, with 26 out of 31 tested surfactant precipitating at the highest salinity investigated (200,000 ppm), rendering them unsuitable for our conditions. For the foam-flood tests, another problem is the wettability of the formation in which the surfactants are to be used. The ability of the foam to reduce the gas's mobility is significantly less in hydrophobic- than in hydrophilic media and also the correlation with the bulk-foam experiments is not as strong for the hydrophobic experiment.

In **Chapters 3** and **4** we discuss methods for determining accurate parameter values for use in foam-flood simulations. We present a simple and direct method for fitting the parameters present in the local-equilibrium foam model in the reservoir simulator STARS. Similar models are present in other simulators such as ECLIPSE or UTCHEM so our method is also applicable there. We

discuss co-injection and SAG injection processes separately as these require different fitting approaches. The latter process requires specific attention to the behaviour at very high foam quality (gas fractional flow). The fractional-flow curve is the key to predicting the performance of a SAG foam process during gas injection. During the period of gas injection, the mobility at the leading edge of the gas bank determines whether a SAG process can be successful at maintaining mobility control over the displaced phase. This point corresponds to the point of tangency to the fractional-flow curve, which, in the presence of strong foam, occurs at very high foam quality.

In **Chapter 5** we introduce a simple radial-flow model for foam during the gas-injection cycle of a SAG process based on fractional-flow theory. We distinguish two different cases, one where the injected foam is much less mobile throughout the foam bank than the fluids ahead of foam ("strong foam" case) and one where the foam is just able to maintain mobility control with the fluids ahead of it ("weak foam" case). We find that the pressure difference across the foam bank is nearly constant in time as long as the foam collapses near the injection well. For the "strong foam" case, the injection rate required to maintain constant injection pressure is nearly constant as well, but for the "weak foam" case the injection rate must increase with time. We compare results obtained using this model from 2D simulations in a quarter-five-spot pattern. For the "strong foam" we find decent agreement between the two during the period where the flow in the 2D pattern is approximately radial. The "weak foam" simulation shows some deviation from the model, as some frontal instabilities are observed leading to viscous fingering within the foam bank.

Finally, in **Chapter 6** we discuss foam-flooding experiments in low-permeability, carbonate rocks. Even in very harsh conditions (that is: 1 mD Indiana limestone rock, 200,000 ppm salinity, temperature of $55°$C and the presence of crude oil), we still manage to create a foam, albeit a fairly weak foam. We also apply our parameter-fitting approach for SAG injection processes to the experimental results and find that the generated foam is just about able to maintain mobility control over the displaced phase, meaning it is similar to the "weak foam" case discussed above. Another set of experiments is performed using heterogeneous, Edwards White carbonate rock. CT visualization allows one to determine the influence of the heterogeneities in this rock, such as vugs several mm in size, by measuring the liquid saturation inside the rock during the experiment. We find that foaming is possible in this rock, but that saturations are not uniform throughout the core even when the pressure gradient across the core reaches a steady-state.

SAMENVATTING

Conventionele oliewinningstechnieken zijn niet in staat om alle olie te winnen uit een reservoir. Op dit moment wordt slechts 20 tot 40% gewonnen van de olie die initieel in het reservoir aanwezig is. Verbeterde oliewinningsmethodes (Engels: Enhanced Oil Recovery (EOR)) zijn benodigd om de achtergebleven 60 tot 80% te winnen. Een gebruikelijke EOR methode is de injectie van gas in het reservoir om de olie te verplaatsen en de druk in het reservoir te behouden. Het 'sweep'-rendement van zo'n proces is vaak laag, vanwege heterogene reservoirs, viskeuze instabiliteit tussen het geïnjecteerde gas en de viskeuzere vloeistoffen die worden verplaatst en de neiging van het gas om naar de bovenkant van een reservoir te stromen door de zwaartekracht. Deze problemen kunnen worden aangepakt door de toepassing van schuim EOR. Schuim zorgt ervoor dat het gas in individuele belletjes wordt opgesloten. Hierdoor wordt de mobiliteit van het gas verminderd, wat zorgt voor een stabieler verplaatsingsfront en dus in een verhoogde volumetrische 'sweep'.

Dit proefschrift verkent verscheidene aspecten van verbeterde oliewinning met behulp van schuim en is vooral gespitst op het gebruik van schuim in carbonaat-formaties. Hiertoe worden verschillende onderwerpen beschouwd, van het screenen van oppervlakte-actieve stoffen (Engels: surfactants) tot het ontwerpen van methodes om parameters te fitten en het modelleren van injectie processen waar surfactants en gas alternerend worden geïnjecteerd (Engels: surfactant-alternating-gas (SAG)). Tot slot worden experimenten uitgevoerd in kalksteen kernen.

Een benodigde eerste stap voor een succesvol schuim EOR project is het vinden van een schuim-surfactant die kan worden gebruikt onder moeilijke omstandigheden. In **Hoofdstuk 2** introduceren we een screening methode die ten eerste kan worden gebruikt om een groot aantal surfactants te screenen door middel van bulk-schuim tests. Verder kan ook kwantitatief worden bepaald hoe het schuim zich gedraagt in poreuze media met behulp van experimenten waarin deze media worden doorstroomt met schuim. Onze experimenten tonen aan dat het zoutgehalte van de oplossingen van grote invloed is op de prestaties van de surfactants. Van de 31 geteste surfactants slaan er 26 neer bij het hoogste gebruikte zoutgehalte (200,000 ppm). Hierdoor zijn deze niet geschikt voor gebruik onder onze omstandigheden. Uit de doorstromingsexperimenten blijkt dat de bevochtigbaarheid (Engels: wettability) van het poreuze medium ook problematisch is voor het creÃ«ren van schuim. In hydrofobe me-

dia is het schuim minder goed in staat om de mobiliteit van het gas te reduceren dan in hydrofiele media. Ook is de correlatie met het gedrag in de bulk-foam experimenten niet zo sterk in de hydrofobe doorstromingsexperimenten.

Hoofdstukken 3 en **4** gaan over methodes voor het bepalen van nauwkeurige waardes van parameters die gebruikt worden in stroming-simulaties van schuim in poreuze media. We presenteren een eenvoudige methode om de parameters te bepalen die aanwezig zijn in het lokale-evenwichtsmodel van de reservoir-simulator STARS. Soortgelijke modellen zijn aanwezig in andere simulatoren zoals ECLIPSE en UTCHEM dus deze methode is ook daar toepasbaar. Co-injectie en SAG injectie processen worden apart behandeld, omdat hiervoor verschillende benaderingen nodig zijn. Voor het laatstgenoemde proces moet specifiek worden gelet op het gedrag bij erg hoge kwaliteit van het schuim (de gas-fractie van het debiet). Met de fractionele stromingscurve kan het gedrag tijdens de periode van gasinjectie in een SAG proces worden voorspeld. Het succes van een SAG proces hangt af van de mobiliteit aan de voorzijde van het gasfront. Als deze mobiliteit lager is dan die van de verplaatste fase is het proces succesvol in het controleren van de mobiliteit. Dit punt valt samen met een tangentieel punt aan de fractionele stromingscurve. Bij sterk schuim komt dit punt overeen met een erg hoge schuimkwaliteit.

In **Hoofdstuk 5** introduceren we een eenvoudig radiaal stromingsmodel voor schuim tijdens de gasinjectie-cyclus van een SAG proces. Dit model is gebaseerd op fractionele stromingstheorie. We onderscheiden twee verschillende gevallen, één waar het geïnjecteerde schuim veel minder mobiel is dan de verplaatste vloeistof ("sterk schuim") en één waar het schuim net sterk genoeg is om voor mobiliteitscontrole te zorgen ("zwak schuim"). Hieruit blijkt dat het drukverschil over de schuimbank bijna constant blijft zolang het schuim volledig uiteenvalt nabij het injectiepunt. Voor het "sterke schuim" is de injectiesnelheid die benodigd is om een constante injectiedruk te behouden ook bijna constant, maar voor het "zwakke schuim" moet de injectiesnelheid toenemen naarmate de tijd vordert. Resultaten van dit model zijn ook vergeleken met die van 2D-simulaties in een kwart vijf-spot geometrie. Voor het "sterke" schuim komen de resultaten goed overeen voor de periode waarin de stroming in de 2D-geometrie bij benadering radiaal is. Voor het "zwakke schuim" is er wat afwijking tussen het model en de 2D-simulatie. Dit komt doordat er instabiliteiten optreden in het schuimfront die ervoor zorgen dat het gas zich een weg vingert door het te verplaatsen water.

Tot slot worden in **Hoofdstuk 6** de resultaten besproken van een reeks schuim-doorstromingsexperimenten in kalksteen met een lage permeabiliteit. Zelfs onder erg moeilijke omstandigheden (dit houdt in: 1 mD Indiana Limestone gesteente, 200,000 ppm salinity, temperatuur van 55°C en in aanwezigheid

van ruwe olie) blijkt het mogelijk te zijn om een schuim te genereren, ook al is het een vrij zwak schuim. Ook is de parameter fit methode for SAG injectie processen toegepast op de experimentele resultaten. Hieruit blijkt dat het gegenereerde schuim net in staat is mobiliteitscontrole te behouden over de verplaatste fase. Het is daarmee dus vergelijkbaar met het "zwakke schuim" zoals dat hierboven omschreven is. Een tweede set experimenten is uitgevoerd waarbij gebruik is gemaakt van heterogeen, Edwards White gesteente. Met behulp van CT scan visualisatie kan de invloed van de heterogeniteiten op de schuimstroming in de steen worden bepaald door de verzadiging van de vloeibare en gasfase te meten. Deze heterogeniteiten zijn onder andere holtes met een grootte van enkele mm. Ondanks deze heterogeniteiten blijkt het mogelijk te zijn om schuim te genereren in deze steen, maar de verzadigingen zijn niet uniform door de hele kern heen zelfs wanneer de drukgradiënt over de kern heen wel een stabiele toestand bereikt.

ACKNOWLEDGEMENTS

This thesis is the result of nearly five years of work at the Geoscience & Engineering department at TU Delft. Many people have supported me during this period and I would like to take this opportunity to thank them.

Firstly, I would like to thank Prof. Bill Rossen for giving me the opportunity to take on this project. Through the years he has been a fantastic mentor, constantly introducing me to new concepts, carefully analysing all of our obtained results and meticulously checking and commenting upon any texts I had written. Furthermore he deserves praise for remaining patient during times when I felt like I was hardly making any progress especially in the lab.

I would like to express my gratitude to the rest of the thesis committee for agreeing to be on the committee and taking time out of their busy schedules to review my work. I would also like to thank Maersk Oil for supporting this project. I have had the pleasure of working with several members of their Research and Technology Centre in Doha, Qatar. Especially fruitful discussions and cooperation with Dr. Kristian Mogensen and Dr. Martin Vad Bennetzen have greatly aided me in completing this work.

None of the experimental work performed during this project would have been possible without the excellent and continuous support from the lab technicians. I would especially like to single out Jan Etienne who built the greatest setup in the entire lab for this project which is still being used by my successor on a daily basis and will be for years to come.

During my time at TU Delft I have been fortunate enough to work alongside people from all corners of the earth providing me insights into a whole range of different cultures. I will never forget all the good times together both in- and outside the office. I truly feel like I have made a lot of friends for life here. Also thanks to all my other friends some of whom I have known since childhood and who have played an important role in my life throughout the years.

But all things come to an end and after close to five years in Delft I set sails for the (somewhat) sunnier shores of Bordeaux, France where I have been working for the past six months as a postdoc. I wish to thank the entire group at EN-SEGID along with the new friends I am meeting here for being very welcoming to a Dutch guy whose ability to converse in French leaves a lot to be desired.

My final words of gratitude are for my family who have always been there for me and have given me everything I could have ever needed to get to where I am today. Thank you very much!

LIST OF PUBLICATIONS

The work discussed in this thesis is also described in the following publications.

PEER-REVIEWED JOURNAL PAPERS

Boeije, C. S. and Rossen, W. R. Gas-Injection Rate Needed for SAG Foam Processes To Overcome Gravity Override. *SPE Journal*, Vol. 20 (01):pp. 49 − 59, (SPE 166244), February 2015.

Boeije, C. S. and Rossen, W. R. Fitting Foam-Simulation-Model Parameters to Data: I. Coinjection of Gas and Liquid. *SPE Reservoir Evaluation & Engineering*, Vol. 18 (02):pp. 264 − 272, (SPE 174544), May 2015.

Rossen, W. R. and Boeije, C. S. Fitting Foam-Simulation-Model Parameters to Data: II. Surfactant-Alternating-Gas Foam Applications. *SPE Reservoir Evaluation & Engineering*, Vol. 18 (02):pp. 273 − 283, (SPE 165282), May 2015.

CONFERENCE PROCEEDINGS

Boeije, C. S. and Rossen, W. R. Fitting Foam Simulation Model Parameters to Data. *17th European Symposium on Improved Oil Recovery*, (15594), St. Petersburg, Russia, 16-18 April 2013a.

Boeije, C. S. and Rossen, W. R. Gas Injection Rate Needed for SAG Foam Processes to Overcome Gravity Override. *SPE Annual Technical Conference and Exhibition*, (SPE 166244), New Orleands, LA, USA, 30 Septermber - 2 October 2013b.

Boeije, C. S., Vad Bennetzen, M., and Rossen, W. R. A Methodology for Screening Surfactants for Foam Enhanced Oil Recovery in an Oil-Wet Reservoir. *9th International Petroleum Technology Conference*, (IPTC 18248), Doha, Qatar, 6 - 9 December 2015.

Rossen, W. R. and Boeije, C. S. Fitting Foam Simulation Model Parameters for SAG Foam Applications. *SPE Enhanced Oil Recovery Conference*, (SPE 165282), Kuala Lumpur, Malaysia, 2-4 July 2013. ISSN 978-1-61399-258-6.

ABOUT THE AUTHOR

Chris Boeije was born on 3 October 1984 in Zwolle in the Netherlands. In 2008 he obtained as M.Sc. degree from the University of Twente in Mechanical Engineering specialising in Engineering Fluid Dynamics. After this he studied physics at the University of Groningen from which he obtained a B.Sc. degree in 2010. In May 2011 he started a PhD project at Delft University of Technology under the supervision of Prof. dr. W. R. Rossen which has culminated in this thesis. In October 2015 he started working as a postdoctoral researcher at Bordeaux-INP ENSEGID in Bordeaux, France.